January 2012

The Electronic Structure of Biomolecular Self-Assembled Monolayers

Matthaeus Anton Wolak
University of South Florida, mwolak@mail.usf.edu

The Electronic Structure of Biomolecular Self-Assembled Monolayers

by

Matthaeus Wolak

A dissertation submitted in partial fulfillment
of the requirements for the degree of
Doctor of Philosophy
Department of Electrical Engineering
College of Engineering
University of South Florida

Major Professor: Rudy Schlaf, Ph.D.
Vinay Gupta, Ph.D.
Li-June Ming, Ph.D.
Arash Takshi, Ph.D.
Jing Wang, Ph.D.

Date of Approval:
June 13, 2012

Keywords: peptide nucleic acid, tetraphenylporphyrin, work function,
charge injection barrier, interface dipole, XPS

DEDICATION

I dedicate my dissertation to my girlfriend Emily Helmrich, and my parents Margarete and Anton Wolak, who supported me throughout the process and always had the right words of encouragement for me. I am very grateful to you and will always appreciate all that you have done for me. There is no doubt in my mind that without your continued support I could not have completed this process.

ACKNOWLEDGMENTS

I would like to thank Dr. Rudy Schlaf for his guidance and support throughout the process of writing this dissertation and I appreciate his commitment.

I am also thankful to the members of my supervisory committee for their help and advice on how to improve my work.

Furthermore, I would like to express my gratitude to Dr. Alexander Balaeff and Dr. David Beratan from Duke University for providing me with the DOS calculations used in this dissertation and the fruitful discussions we had.

I would also like to thank Dr. Catalina Achim and her students at Carnegie Mellon University for giving me the opportunity to engage in their research and their continuous supply of PNA solutions, which were crucial for my research.

I am further thankful to Dr. David Waldeck and Emil Wierzbinski of the University of Pittsburgh for their ellipsometry measurements of the investigated PNA monolayers.

Additionally, I would like to thank Dr. Shengqian Ma, who provided me with the tetraphenylporphyrin molecules used in this dissertation and was always willing to engage in helpful discussions.

I would also like to thank all the members of the Surface Science Lab of the University of South Florida for their continuous help during my research.

TABLE OF CONTENTS

LIST OF TABLES

LIST OF FIGURES

ABSTRACT

The studies presented here address the characterization of the electronic structure of various self-assembled monolayers (SAMs) of peptide nucleic acid (PNA) and tetraphenylporphyrin (TPP) SAMs and arrays, formed on gold substrates.

PNA is a promising alternative to DNA for bio-sensing applications, as well as for strategies for self-assembly based on nucleic acid hybridization. In recent years charge transfer through PNA molecules was a focus of research due to possible applications in self-assembled molecular circuits and molecular tools. In light of this research it is interesting to investigate the electronic structure of PNA interfaces to gold, a potential electrode material.

TPP is, due to its electronic structure, an organic p-type molecular semiconductor. Such a material can provide an alternative to standard micro- and optoelectronic devices and in recent years more attention was paid to semiconducting polymers and organic compounds offering these low-cost and flexible alternatives. Therefore, it is of high importance to investigate the prospect of using modified TPP molecules for the formation of interconnected molecular networks on metallic surfaces.

All investigated monolayers were formed from solution in a nitrogen atmosphere inside a homemade glove box. This process allowed for PNA SAM and TPP SAM and array formation on clean Au substrates without the exposure to the ambient atmosphere. Ultraviolet and X-ray photoemission spectroscopy (UPS and XPS) measurements on the

resulting PNA SAMs and TPP SAMs and arrays, which were performed in a to the glove box attached vacuum chamber containing a photoemission spectrometer, revealed the hole injection barriers at the interfaces and the interface dipoles.

In addition to the UPS and XPS measurements on PNA, electronic structure calculations based on molecular dynamics sampling of the PNA structure were obtained, yielding the HOMO-LUMO gap and the electronic density of states for PNA. Combined with the UPS data, the theoretical calculations enabled estimation of the charge injection barriers for the PNA SAMs at the interface, as well as the assignment of individual UP-spectral features to specific molecular orbitals.

The orbital line-up at the interface between the Au substrate and the PNA indicated a significant interface dipole resulting in the alignment of the Au Fermi level near the center of the PNA HOMO-LUMO gap. This alignment causes large charge injection barriers for both holes and electrons, and thus impedes charge transfer from Au into the PNA SAM. The study of PNA molecules with ferrocene termini showed that this hole injection barrier is shifted to lower energies at the PNA/ferrocene interface. This shift was explained with a molecular orbital reconfiguration through the presence of the ferrocene terminus. The further investigation of the dependence of the electronic structure of PNA SAMs, based on their orientation, showed that incomplete films containing flat lying molecules can have a significant impact on the charge injection barriers. The close proximity of the nucleobases to the Au surface offers new ways for charge transfer between the substrate and the PNA molecule through its nitrogen sites, leading to a lowering of the hole injection barrier at the interface.

The TPP arrays were formed by depositing $AgNO_3$ on the Au substrate prior to TPP incubation using the electrospray technique. The interaction of $AgNO_3$ with the TPP promoted the formation of an interconnected thin film forming a network on the Au substrate. The line-up at the Au/TPP interface without $AgNO_3$ exposure showed an interface dipole formation with injection barriers that would potentially obstruct charge injection into the molecule. However, the addition of $AgNO_3$ to the process resulted in the formation of fine structures, and lead to a lower hole injection barrier due to an induced dipole, which would ultimately improve charge transfer between the substrate and the thin film. A separate thiolated TPP derivative was used to form SAMs on a gold substrate. The SAM exhibited an even lower injection barrier than the mentioned TPP thin film with $AgNO_3$ exposure, leading to the conclusion that a mix of both TPP derivatives could potentially lead to a SAM with long range interconnectivity and a low hole injection barrier towards the substrate.

CHAPTER 1: INTRODUCTION AND MOTIVATION

1.1: Motivation and Outline of this Dissertation

As modern day electronic devices continue to shrink in their size, it is evident that their physical limits will soon be reached. Single electron transport devices based on organic molecules, such as conjugated oligomers or aromatic molecules, present a promising alternative to conventional devices. Usually, fabricating a solid structure with features below 10 nm presents a technological challenge. Simple molecules can, however, be easily self-assembled into predefined patterns and their size lies within the mentioned limits. Organic molecules allow for easy integration of functional groups and the availability of a large range of synthetic procedures enables the rational design and assembly of molecular electronic devices. In the recent past a wide range of organic semiconductors was the focus of several studies discussing their potential for the use in transistors, photovoltaic cells and electroluminescent devices [1, 2]. The properties of these organic semiconductors are often compared to those of regular inorganic semiconductors. Just as for inorganic semiconductors, the mechanism behind the energy level alignment at organic/metal interfaces has to be understood in order to improve the performance of such organic devices.

The contact between the self-assembled molecule and the metal electrode is crucial to electron and hole transport through a single molecule. Not only is this apparent

in contact resistance, but also in the nature of the molecular device, depending on the degree of molecular orbital interaction between the molecule and the electrode. The electronic interaction between the molecule and the surface determines the charge transport across the interface. Therefore, it is important to understand and control the electronic interaction between a single molecule and the metal substrate in order to be able to design electronic devices based on organic molecules. A number of theoretical and experimental studies on the electronic structure at the interface of thiolated SAMs were published in the past, but experimental data on larger molecules containing thiol groups, however, is still rare.

This dissertation focuses on the characterization of the electronic structure of two types of organic molecules: peptide nucleic acid (PNA) based single strands containing two kinds of nucleobases and two derivatives of tetraphenylporphyrin (TPP).

The first part of the dissertation addresses the formation and characterization of PNA SAMs. The PNA molecules were based on a single strand with 7 backbone segments and a cysteine head-group, which allowed for self-assembly through its thiol group. Experimental data regarding the electronic structure was collected on the PNA SAMs through photoemission spectroscopy (PES) using a selection of PNA strands with different nucleobases attached to the backbone. The experiments showed that the type of nucleobase present in the SAM has a significant impact on the hole injection barrier, while strand orientation can additionally influence the barrier as well.

The second part of this work focuses on the electronic structure of tetraphenyl-porphyrin derivatives, motivated by the potential application of tetraphenylporphyrins for the formation of long range conductive molecular networks. For this study, two different

derivatives of TPP were used, one containing thiol groups (TPP-S) and the other containing nitrogen atoms (TPP-CN) at the peripheral positions of the TPP molecule. The goal in these experiments was to investigate the self-assembly of thiolated porphyrins (TPP-S) and the possibility of a formation of an interconnected network of TPP-CN molecules. Eventually, the information extracted from these experiments could be used for the design of molecular wires and arrays formed by self-assembly of thiolated TPP with nitrogen groups at its peripheral positions.

1.2: Charge Transfer and Electronic Structure of Organic Materials

Electronic devices that are based on organic materials are potential alternatives to present standard devices in the integrated circuit industry, as they introduce benefits in fabrication, mechanism and cost [1]. The idea of molecular electronics has received an increase in interest in recent years due to advancements of methods for characterizing and manipulating single molecules. The field effect in organic semiconductors was already described in the 1970s [3-5], but the first organic field effect transistors (OFETs) were developed only much later in 1987 [6]. Devices based on organic materials typically include the adsorption of molecules on metallic surfaces and researchers focus on several processes connected with this deposition method. In particular, the preparation and characterization of monolayer assemblies of oriented organic molecules gained a lot of attention in the recent past.

Understanding the electronic structure of metal/organic interfaces is of high interest as a proper adjustment of the interfacial electronic structure is essential to increase the efficiency of charge injection from the metal substrate to the organic SAM. In general, electrons and holes are injected from metal contacts into the organic material

resulting in a charge flow through the device. Efficient injection, however, can only be achieved, if the charge injection barriers at the interface of metal and organic material are small [7]. In this context, charge transfer between the organic molecule and the metal substrate, the actual interaction of the molecular levels of the organic material with the continuum of states in the metal [8], the intramolecular alteration of the molecular levels prompted by the change of electrostatic potential in the organic material itself [9], and the energy barrier and energy level alignment at the interface [10], are of great importance.

All these processes are interface related and are evident in the transport characteristics of the investigated organic device. They determine the energy and character of the molecular orbitals, which are responsible for charge transfer through the organic material, and define the electronic structure at the metal/molecule interface.

Although a wide range of techniques like Langmuir-Blodgett [11, 12], spin-coating [13, 14] and vapor deposition [15, 16] can be applied in order to deposit organic molecules on substrates, most of the molecular devices based on organic molecules involve the adsorption of these molecules onto metal surfaces through their head-groups. The most common combination for the adsorption of molecules on surfaces is the one of gold as the metal substrate and thiolated sulfur as the attachment group on the molecule. The deposition of thiols on a gold surface allows for a highly ordered assembly of molecules on the surface without any external input and a variety of functional groups can be incorporated into the thin film that way. The resulting film is commonly called a self-assembled monolayer (SAM) and by employing this technique, a wide range of thin films with an ordered arrangement can be formed [17-20].

CHAPTER 2: FUNDAMENTALS OF ORGANIC SELF-ASSEMBLED MONOLAYERS

Peptide nucleic acids (PNA) and tetraphenylporphyrins (TPP) represent a group of versatile biomolecular templates as they offer means for easy attachment of functionalized groups. PNA is a synthetic alternative to DNA and shows superior bonding characteristics and thermal stability. With such, it can likely be used in biosensors and organic circuits. TPP is a potential candidate for light-harvesting applications and the formation of molecular wires and networks for organic devices. Equipped with the proper functional groups, these biomolecules can easily be integrated in self-assembled monolayers, laying the foundation for the development of new organic devices and sensors. The fundamentals of self-assembly of organic monolayers and its mechanism will therefore be discussed in this chapter. In addition, further insight will be given into the structure and characteristics of the employed PNA and TPP molecules.

2.1: Self-Assembly of Monolayers

Self-assembled monolayers (SAM) have become a common method in the area of microelectronics, nanopatterning and biomaterials as well as many more research applications [18]. Self-assembly is an important fabrication technique in nanoscale science and it helps overcoming the limits set by directed assembly. The main mechanism

of self-assembly is the capability to form ordered molecular assemblies through adsorption of an active surfactant on a solid surface [18]. The organized layer formed by self-assembly usually consists of molecules in which one end of the molecule, called the 'head-group', shows a specific, reversible affinity towards the substrate (Figure 1). Additionally, these molecules often contain a 'tail-group' which consists of a functional group at the terminal end, opposite the head-group. Both groups are usually connected through a chain or backbone which is the main structure of the molecule and provides means of charge transfer between the head and the tail of the molecule. The self-assembly process can be achieved by the chemisorption of the hydrophilic head-groups onto a substrate by either evaporating the material or incubating the substrate in a solution containing the organic molecules.

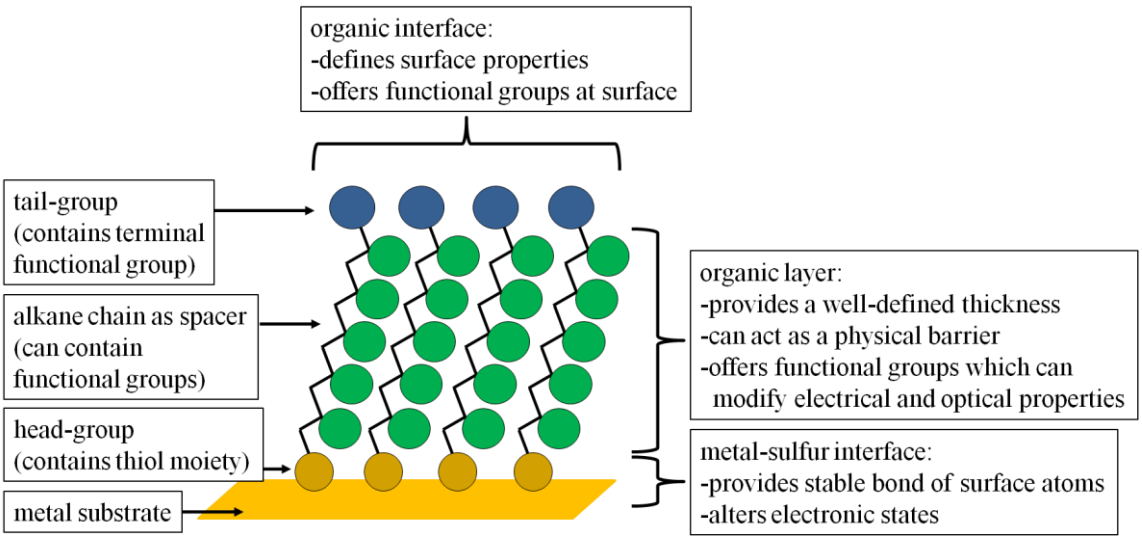

Figure 1: Diagram of an ideal SAM of alkanethiolates formed on a gold surface with highlighted anatomy and characteristics. (Reprinted (adapted) with permission from [17]. Copyright 2005 American Chemical Society)

In directed assembly, external manipulation is usually used to arrange atoms and molecules in a precise pattern. Therefore, a high degree of control over where the individual atoms or molecules are placed is needed. Photolithography and electron beam

lithography are usually used for two-dimensional directed assembly, however it is not possible to achieve assembly on a molecular scale with these tools. Atomic force microscopy (AFM) and scanning tunneling microscopy (STM) are other means of positional assembly which allow for single molecule arrangement, but result in a very time consuming process, if larger patterns have to be assembled. Self-assembly is an important alternative to the above mentioned techniques as it offers the ability to arrange single molecules on the nanometer scale in less time than with the use of AFM or STM.

Self-assembly is a process that can easily be found in biology, where supramolecular chemistry shows how molecules can merge to form new noncovalent structures [21-23]. The self-assembly process was already discovered in 1946 by Bigelow et al. [18, 24-26], where it was reported that some types of polar organic molecules adsorbed onto polished solid surfaces in non-polar solvents and formed well-oriented monolayers. It was then also concluded that the monolayer formation was a reversible adsorption from solution and was not just an accumulation of insoluble films floating on top of the solvent, like in the Langmuir-Blodgett deposition technique [26]. The process of self-assembly was already discovered in the 1940s, but it took several decades before studies on silane monolayers [27, 28] and thiol self-assembly on gold [29] made it a popular tool in modern surface science.

Functionalized long-chain hydrocarbons are usually employed for the formation of self-assembled monolayers and larger supramolecular structures can be achieved with their employment [18]. SAMs can be assembled by a wide range of reactions, like van der Waals interactions (as in long-chain aliphatics for example), chemisorption of thiols on coinage metals, chemisorption of trichlorosilanes and trialkoxysilanes on glass and

silicon, carboxylic acids on metal oxides, or H bonding in smaller structures [30]. Selecting the appropriate type of head-group depends on the application of the SAM.

Long-chain n-alkanoic acids can spontaneously adsorb on a metal surface through an acid-base reactions. This process leads to the creation of a salt at the interface which forms between the carboxylate anion and the metal. The adsorption of these types of acids was observed on surfaces like aluminum oxide, silver oxide, and copper oxide [18].

In order to form SAMs using trichlorosilanes and trialkoxysilanes, the surface has to be hydroxylated. Silane SAMs can be formed on a variety of surfaces like glass, quartz, silicon, mica, aluminium and gold [18]. The molecules adsorb on these surfaces through the formation of polysiloxane, which connect to the silanol groups (-SiOH) on the surface via Si-O-Si bonds [18]. However, it is difficult to acquire reproducible films using this method as the SAM formation strongly varies with the amount of water that is present in the solution and the degree of hydrolysis of the substrate.

2.1.1: Thiol Based Self-Assembly on Metals

Atoms like sulfur, phosphine, and selenium have a strong affinity for various metals including gold, silver, platinum, iron, copper and others [18], and compounds containing these atoms adsorb from solution onto the metal surface forming stable monolayers. Terminally functionalized thiol-based (-SH-) SAMs readily form on gold. They present an effective method for precise chemical modification of surfaces [31, 32] and are the most commonly studied systems. The adsorption of these sulfur based molecules on gold surfaces represents a chemisorption process with exceptional and significant properties. The bond between gold and sulfur is relatively strong, displaying a bond strength of approximately 44 kcal/mol [32].

It is surprising that sulfides and disulfides form strong chemisorption bonds on gold [33], given the inertness of this metal toward the chemisorption of most polar organic molecules. Moreover, the two-dimensional films formed through this process assemble into organized structures and even seem to resemble single layer crystalline phases [34]. The inertness of gold and strong affinity towards sulfides [34] allow for SAM formation in the presence of many other functional groups [30] on a surface that resists oxidation and atmospheric contamination fairly well [35].

The actual mechanism behind the adsorption of sulfides on gold is still being discussed, but the most prominent concept is the oxidative addition of the S-H bond to the gold surface, leading to a bond between the thiol and the gold, resulting in a reductive elimination of hydrogen [18, 36]:

$$RS\text{-}H + Au^0 \rightarrow RS\text{-}Au + \tfrac{1}{2} H_2 \qquad (1)$$

For the bond between disulfides and gold, it was proposed that an intermediate step exists, where the disulfide is bound to only one gold atom and then the S-S bond breaks, leading to two S-Au bonds:

$$RS\text{-}SR + 2\ Au^0 \rightarrow 2\ (RS\text{-}Au) \qquad (2)$$

Once the monolayer forms, no differences between the sulfide and disulfide SAMs can be observed by surface analysis techniques [30, 34, 37, 38].

Monolayers of alkane chains formed through thiol bonds with the gold surface usually exhibit hexagonal packing and their chains have a tilt of 30˚ from the surface normal [30, 32, 39], which maximizes the van der Waals interactions between the chains. The van der Waals interactions between the chains have a significant impact on the

monolayer when one considers the length of the chains present in the monolayer. It was concluded that longer chains usually result in a more structured monolayer due to the increased amount van der Waals interactions, while shorter ones lead to more disordered monolayers, as observed through ellipsometry and contact angle measurements [30, 39-41].

It was determined through low-energy electron diffraction that the spacing of the alkane chains is approximately 5 Å [42]. This spacing leads to the conclusion that the sulfur atoms at the interface would have a similar spacing, which is larger than the van der Waals diameter of sulfur, and an interaction between neighboring sulfur atoms should not exist.

However, X-ray diffraction studies showed that the actual distance between the sulfur atoms is as little as 2.2 Å [36]. The rather small distance between the sulfur atoms suggests that an interaction should occur, and that the sulfur atoms could exist as homodimers at the monolayer-gold interface, as shown in Figure 2. The model was further supported by studies employing thermal desorption spectroscopy (TDS), where it was found that alkanethiols desorb as dimers from a gold surface [43, 44].

Thiols can easily be used as functionalizing head-groups for larger and more complex organic molecules allowing for a formation of well-ordered monolayers through self-assembly. By employing thiols as the linker between the metal surface and the organic molecule, it is possible to achieve an arrangement of molecules at the surface with predictable spacing between the molecules. The molecules used for the self-assembly can in general be tailored to match requirements regarding the size and electronic structure that is needed.

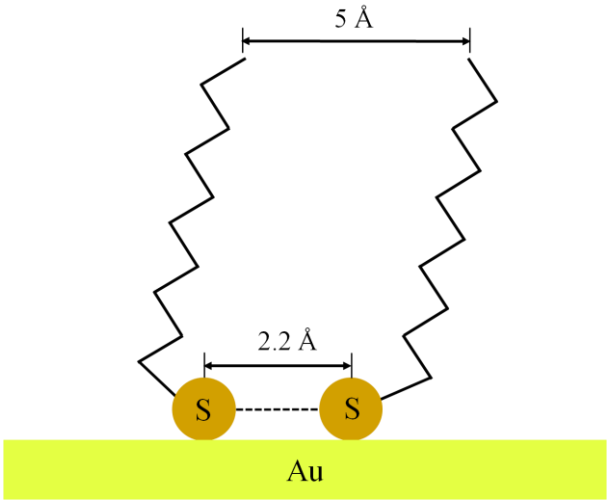

Figure 2: A homodimer formed by two sulfur atoms with a spacing of 2.2 Å exists at the interface while the alkane chains in the overlayer have a spacing of 5 Å. This model was proposed by Fenter et al. [36] in the past.

Additionally, the head-groups can be modified by implementing more thiol groups and therefore allowing for stronger bonding to the surface. Linkers, like simple alkane chains, can also be embedded in the molecules if separation is required between the metal surface and the functionalized tail-group. The monolayer could even contain a multilayered system if several linkers and functionalized groups are used, providing biological sensors, electronic or optical circuits on a very small scale.

2.2: Peptide Nucleic Acids

Peptide nucleic acid (PNA) is an analogue to Deoxyribonucleic acid (DNA), which is a building block of life, carrying the genetic information of living organisms. DNA is an oligonucleotide and its central part, the backbone, is comprised of sugars and phosphate groups joined by ester bonds. It is not only the building block of life, but can also be used in biological sensors [45, 46] and potentially in electronic circuits [47-49]. While DNA is the carrier of genetic information, Ribonucleic acid (RNA), another

oligonucleotide, decodes the genetic information. Cellular organisms use messenger RNA in order to carry genetic information, which guides the synthesis of proteins. RNA can also be used in biological sensors and has, just like DNA, the potential to be used in organic microelectronic circuits.

Since DNA and RNA can degrade by nucleases in vivo [50] or chemical or enzymatic hydrolysis [51, 52], a large number of oligonucleotide analogues were synthesized in past decades, which bind specifically to DNA and RNA and could form the basis for gene-targeted drugs and sensors. The biological stability of oligonucleotides can generally be modified chemically, but the binding affinity and specificity to DNA and RNA has to be kept intact beyond this modification. The majority of the investigated analogues shows slight modifications in the structure and still closely resembles natural oligonucleotides. There were only a few efforts made in which the backbone of the natural oligonucleotide was drastically altered, resulting in an oligonucleotide with improved characteristics. One of these analogues is PNA, which was first described by Nielsen at al. in 1991 [53]. It is a DNA analogue in which the deoxyribose phosphate backbone has been substituted with a pseudo peptide backbone consisting of repeating N-(2-aminoethyl)glycine units, as seen in Figure 3.

The structure of PNA brings several benefits with it. It is a neutral DNA mimic, and as a result, electrostatic repulsion between PNA and the negatively charged DNA or RNA does not occur. Oligomers containing modified amino acid building blocks can generally be assembled by well-established solid phase peptide synthesis protocols, making PNA in milligram to gram quantities readily available, and providing an alternative to DNA obtained through the common polymerase chain reaction. Reporter

groups, intercalators, metal binders and other molecules can be easily attached either through the N-terminal amino group or the C-terminal carboxylic acid of the PNA backbone. PNA also displays a high biostability since it is neither degraded by nucleases nor proteases. The base spacing of PNAs matches the spacing of DNAs, preserving the sequence-specific binding of nucleic acid oligomers as well [54-56].

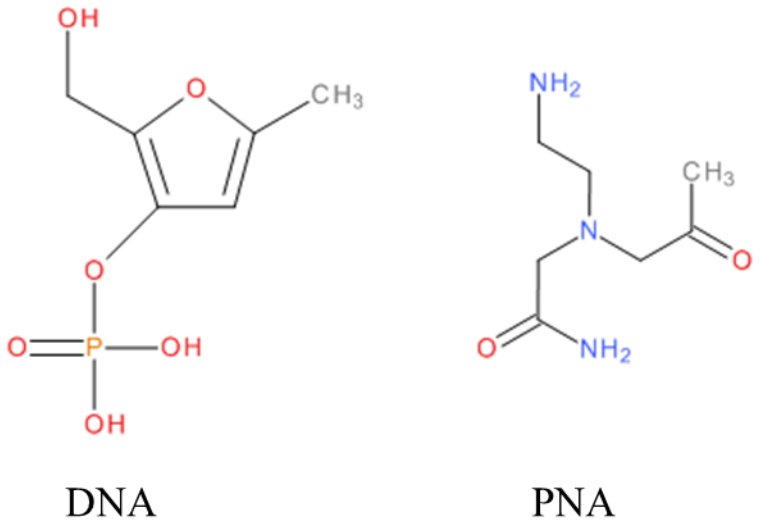

Figure 3: The backbone structure of DNA (left) and PNA (right)

As a result, PNA is a synthetic DNA analogue with properties exceeding those of natural oligonucleotides. A pentadecamer PNA-DNA duplex exhibits a melting temperature (T_m) of 69.5°C [50], while the double strand of DNA-DNA consisting of the same nucleobase sequence, only exhibits a T_m of 53.3°C, demonstrating the increased thermal stability of duplexes containing PNA. PNA-RNA duplexes show even somewhat higher thermal stabilities than found for PNA-DNA duplexes [57]. This increased thermal stability, which was estimated as 1°C per base pair, is mainly attributed to the aforementioned lack of electrostatic repulsion between the strands [57]. The highest

thermal stability can be achieved for PNA-PNA duplexes, as shown in the case of complementary PNA decamers containing all four nucleobases which form antiparallel duplexes [58]. As shown in these experiments, a PNA-PNA decamer duplex has a T_m of 67°C, while a PNA-DNA duplex only displays a melting point of 51°C and DNA-DNA duplexes melt at 33.5°C. Another important characteristic of PNA is the generally higher sequence discrimination which can be easily observed for PNA-DNA mismatches. A single mismatch in a PNA-DNA decamer results in a T_m decrease of 8-20°C, significantly more than for DNA-DNA decamers [50]. With these properties in mind, PNA has evidently a great potential in the fields of molecular biology, diagnostics, nanoelectronics and other related fields.

Several studies were published in the recent past investigating the charge transfer in self-assembled PNA single strand and duplex monolayers employing electrochemical measurements [59-61]. As of now however, no further insight was achieved regarding the detailed electronic structure of PNA. The use of PES in the experiments presented here as a means of characterization allows a full description of the electronic structure of self-assembled PNA monolayers.

For this purpose, 7mers of PNA molecules were used in this study. The PNA molecules varied as some of the molecules did not have any nucleobases attached while others contained 7 thymine or 7 adenine nucleobases. This differentiation helped to answer the question as to how much, if at all, the nucleobase type affects the electronic structure of a self-assembled PNA monolayer. The self-assembly was achieved through the employment of a cysteine head-group on all PNA molecules, which led to a chemisorption of the thiol terminus on the Au substrate. PNA molecules without cysteine

head-groups were explored as well in order to investigate the impact of PNA orientation on the electronic structure. PNA strands with ferrocene tail-groups were studied in separate experiments, giving a more complete picture of the electronic structure of PNA strands that are commonly used in electrochemistry experiments. The characterization of the electronic structure of the PNA strands can be a very helpful tool if the PNA molecules would be employed in microelectronic circuits in the future, offering an insight into the charge transfer characteristics and charge injection barriers.

The variation of PNA molecules and the employment of PES for their characterization allowed for a detailed depiction of the electronic structure of PNA as a function of nucleobase type, tail-group presence and strand orientation.

2.3: Tetraphenylporphyrin

Tetraphenylporphyrin (TPP) is a synthetic heterocyclic compound which resembles naturally occurring porphyrins, like heme and chlorophyll. TPP is ideal for the use in self-assembly of monolayers, as it offers a wide range of variations that are commercially available, or can be fabricated through well-established synthesis processes [62-64].

The core of TPP, the porphyrin nucleus, consists of four rings of the pyrrole type, which are joined by four methine bridges resulting in a macrocycle. Küster [65] was the first to propose this cyclic tetrapyrrole structure in 1912, although it was believed at that time that such a ring would not be stable. Fischer, also called the father of contemporary porphyrin chemistry, was originally opposed to the idea of a cyclic tetrapyrrole structure, as suggested by Küster, but did in the end present the final proof for the existence of the described structure through the synthesis of protoporphyrin in 1929 [66]. The aromatic

ring formation of the porphyrin gives it rigidity and can be simply customized by introducing different groups on the periphery of the porphyrin and incorporating substituents in the meso position during the synthesis, in order to vary the molecule's size and its properties. Although TPP is a p-type organic semiconductor, its conduction type can be easily changed to n-type by peripheral substitution [67]. By employing functional groups in these positions, an interaction between neighboring molecules can be promoted. The interaction can be realized by several means, including metal coordination of cyano groups or carboxylic acids, hydrogen bonding of amides or carboxylic acids, or ionic interactions through charged functional groups. Additionally, linkers can be attached at the meso positions of the TPP allowing for attachment of thiols, sulfides or disulfides, which would present a way to attach the TPP molecule to a gold surface.

Metalloporphyrins contain a metal atom centered in the poprhyrin nucleus and are commonly found in nature as active centers of enzymes. An example would be hemethiolate proteins which contain an iron-poprhyrin and also an axial thiolate ligand at its center, which serves as the active site [68]. Metalloporhyrins have the potential to be used in various technological applications, such as transistor-based sensors for organic molecules [69], organic solar cells [67], or as a sensitizer in dye-based solar cells [70].

In recent years, ordered monolayers of porphyrins and metalloporphyrins on metal and single-crystal surfaces have gained significance in fundamental surface science and their geometric and electronic structure was the topic of several studies [71-73].

TPP derivatives containing thiol groups are expected to readily form SAMs on metal surfaces and a long range of porphyrins and metalloporphyrins were assembled on gold to study their electrochemical properties in the past [74-80]. SAMs of wire-like

molecules with porphyrin tailgroups assembled on gold were the topic of several studies [76, 80-88], investigating the possibility of using porphyrins for the formation of self-assembled networks. In many of these cases, thiols were used as the anchor group, allowing for a chemical bond with the gold surface.

In the studies presented here, two separate TPP derivatives were investigated. The two contained different kinds of linkers attached to the peripheral positions of the TPP molecule. TPP molecules with thiophenol substituents were used (named TPP-S) in the first set of experiments in order to investigate the self-assembly on a gold surface, while TPP molecules with nitrogen atoms linked to the phenyl groups through a carbon bridge (named TPP-CN) were employed to study the formation of multiporphyrin arrays. Both TPP derivatives are shown in detail in Figure 4.

The goal of these studies was the formation of self-assembled molecular structures consisting of porphyrin arrays. The earlier mentioned interaction between neighboring molecules through functionalized groups at the periphery of the TPP molecule can be used in order to increase the strength, stability and arrangement in a self-assembled monolayer. The obtained results can be used as a starting point for further investigations of molecular wires and multiporphyrin dendrimers, which are among the main components in the evolving field of molecular electronics.

The wires can be viewed as conjugated molecules that form one-dimensional electronic connectors between molecular devices, such as single electron transistors and molecular switches. The formation of larger nanotubes with TPP is a proven concept and results in stable and reproducible structures [89]. For this purpose, different functional groups can be attached to the TPP, which results in oppositely charged porphyrins that

arrange into larger structures through ionic self-assembly [90]. The same approach can be used for molecular wire formation and was employed here, were silver atoms promoted the formation of multiporphyrin arrays through the ionic self-assembly between TPP-CN molecules. Multiporphyrin dedrimers are well-defined macromolecules with a treelike array of branch units [91, 92]. The dendrimers can serve as an entire two-dimensional network with the molecular devices (porphyrins with different functional groups) embedded within them.

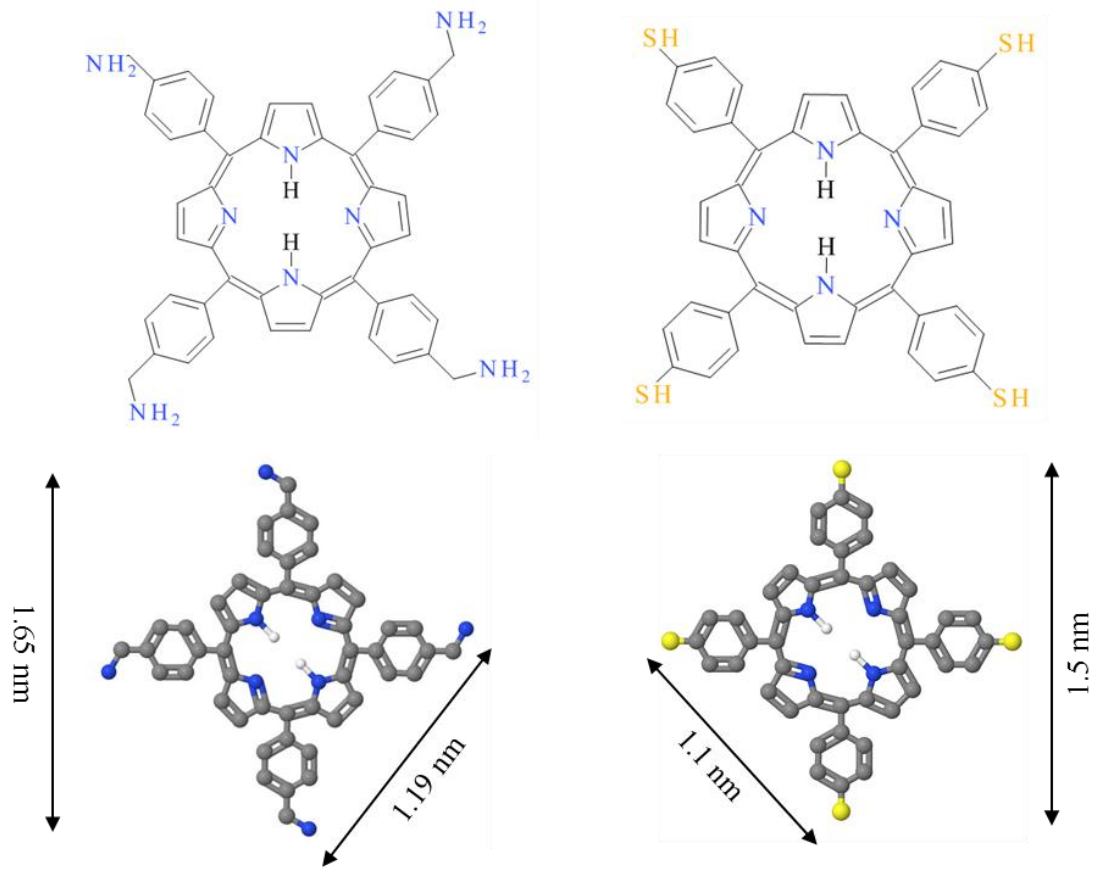

Figure 4: TPP derivatives used in the experiments. TPP-CN is shown on the left, while TPP-S is shown on the right.

Dendrimeric architectures have attracted a growing interest in the field of artificial light-harvesting systems due to the structural similarity to natural antenna

complexes. The natural photosynthetic process is a very elaborate nanobiological system, converting solar energy into an electrochemical potential or chemical energy [93, 94]. The fabrication and investigation of multiporphyrin arrays could help understanding the light-harvesting processes [95-97] since porphyrins are related to chlorophyll, but are more stable and accessible. Synthetic methods used in chemistry usually limit the preparation of arrays of porphyrins with well-defined geometries to a low number (10 or less) and new novel synthetic ways to form large multiporphyrin arrays had to be established in the recent past [79, 84, 98-100].

The approach chosen here for an assembly of porphyrin molecules on gold surfaces involves the exposure of the TPP-CN molecules to silver nitrate ($AgNO_3$). It is expected that the silver ions act as a linker through a bond with the nitrogen atoms positioned at the peripheral positions of the TPP-CN molecule while also providing an electric connection between neighboring molecules. The interaction should lead to a self-assembled multiporphyrin array with a long-range coordination. Such an array can potentially be used as a molecular wire for charge transport or as a light-harvesting antenna. In combination with porphyrin molecules with thiol groups at their peripheral positions, one could fabricate an array that does not only allow for charge transfer between molecules but also to the substrate itself. The main advantage of an array formed with this technique is that no complicated synthesis has to be performed in order to achieve multiphorphyrin arrays. The formation takes place directly on the substrate surface and is driven by self-assembly processes that result in extremely well-ordered arrays with predictable structures within a short amount of time.

CHAPTER 3: EXPERIMENTAL METHODOLOGY

The SAMs investigated in this work were formed by incubating clean Au samples in solutions containing the various biomolecules. The protocol followed during the incubation plays a relevant role for SAM quality and the fundamentals of the incubation procedure will be explained in this chapter. In addition to regular sample incubation, *in situ* electrospray deposition was employed during the TPP-CN related research. This technique allowed for the deposition of a homogenous $AgNO_3$ film on clean Au substrates, which is a prerequisite for TPP-CN array formation. In this context, the basics of electrospray deposition will be discussed in detail. The electronic structures of the formed SAMs were mainly characterized with photoemission spectroscopy (PES) and therefore theory of PES, which includes X-ray photoemission spectroscopy (XPS) and Ultraviolet photoemission spectroscopy (UPS), represents the main portion of this chapter.

3.1: Incubation Procedure

Kinetic studies showed in the past that during an adsorption of alkanethiols on Au surfaces two kinetic processes can be observed [18]. In the first few minutes, the alkanethiol based SAM forms quickly on the surface, reaching about 80-90% of its maximum thickness, and the molecules show contact angles that are close to their

expected limits, yet are not fully reached and a portion of the molecules lies down on the substrate. However, this monolayer is disordered and the final values for thickness and contact angle are reached after several more hours of incubation [30], where a well-ordered monolayer can be observed, resembling a crystalline or semicrystalline structure [30, 38]. During the second step, residual hydrocarbon contaminants are expelled from the surface [101], solvent is removed from the monolayer, and defects are reduced, while packing is enhanced due to lateral diffusion of the molecules [30]. The hydrophilic head-groups finally arrange in a tight pattern at the surface, while the hydrophobic tail-groups assemble far from the substrate. The molecules adsorb readily on the surface as they lower the surface free-energy of the substrate and the formed monolayer stays stable due to the strong chemisorption of the head-groups.

The thiol concentration has a big influence on the duration of the first described step. It was shown that while a concentration of 1 mM led to a completion of the first step after approximately 1 minute, it took over 100 minutes at a concentration of 1 μM [102]. The second step on the other hand is concentration independent and can be defined as a surface crystallization process. During this process the alkyl chains leave the disordered state and recombine in unit cells, forming a two-dimensional crystal.

It can be concluded that the kinetics of the first step are directed by the interaction and reaction between the metal surface and the head-group of the investigated molecule. The activation energy in this case might be dependent on the electron density of the adsorbing sulfur. The second step however seems to correlate with chain disorder, the surface mobility of the chains, and the different encountered chain-chain interactions, for example van der Waals and dipole-dipole interactions. It appears that these interactions

also help lower the time duration of the second step, as longer chains show faster kinetics, which is attributed to the increased amount of van der Waals interactions between the chains [30].

3.2: Fundamentals of Electrospray

Although electrospray was not the main means of thin film deposition in this study, it was used for the *in situ* deposition of $AgNO_3$ during the TPP-CN related experiments. Since it is a rather unique deposition technique, a quick review will be given here in order to explain the physical principle behind it.

The electrospray technique has its origin in electrospray ionization mass spectrometry (ESIMS), which was developed by Fenn and co-workers in the 1980s [103]. ESIMS allows for characterization of large molecules through the analysis of the mass to charge ratio of the investigated material. Therefore the molecules are usually put in their gas phase allowing for easier ionization and charge separation.

By combining the basic concept of ESIMS, the electrospray method, with a PES setup, it allows for the deposition of a wide range of materials, like polymers [104-107], biomolecules [108], nanocrystalline materials [109, 110], and living cells and organisms [111] without exposure to the ambient atmosphere. The advantage of being able to deposit thin films from solution in vacuum is the absence of contamination, which is essential for reliable photoemission spectroscopy measurements [112].

Figure 5 shows a schematic of the general electrospray process. The solution containing the particles that will be deposited on the substrate surface is usually prepared in ambient atmosphere and subsequently loaded into a syringe. The syringe has a capillary at its tip which is made of metal and allows for a high voltage to be applied

between the capillary and ground. Since the vacuum chamber and the substrate are grounded as well, the formed electric field extends from the capillary tip to the substrate.

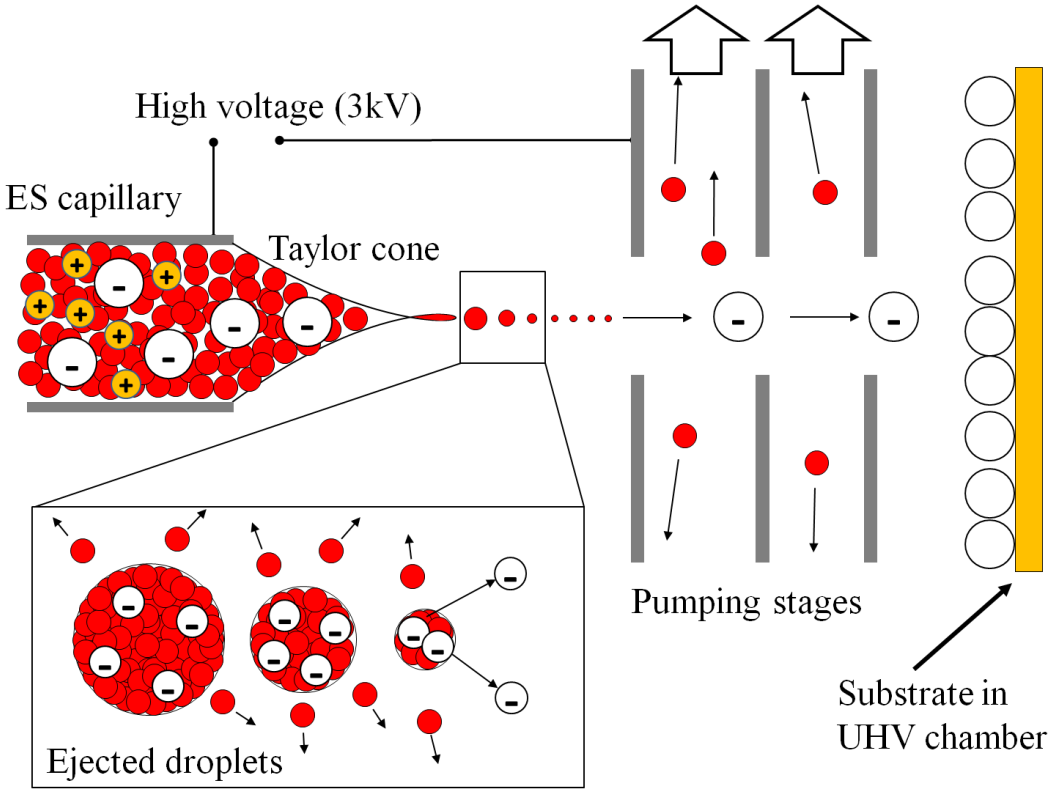

Figure 5: The principle of the electrospray process. The high voltage applied between the capillary and the entrance to the vacuum chamber creates a strong electric field that ionizes the material in the solution. Once droplets leave the capillary, Coulomb explosions separate the solvent from the ionized particles and the solvent is removed in the pumping stages. The material then enters the vacuum chamber and is deposited on the substrate, resulting in a thin film.

The particles are then nebulized from the syringe, as the electric field accelerates the ionized molecules through the capillary. The solution is then ejected from the capillary and forms a Taylor-cone at its tip [113], resulting in a plume of charged droplets. As a result an aerosol is formed, which contains solvent molecules as well as ionized particles and is drawn to the intake orifice leading to the vacuum chamber. The droplets evaporate during flight and the solvent molecules are extracted in the differential

pumping stages while the charged droplets shrink in size. Eventually, the Coulombic forces within the droplets become strong enough to overcome the surface tension of the droplet and lead to so called 'Coulomb explosions'. The Coulomb explosions separate the ionized particles from the solvent, resulting in a beam of molecules that are deposited on the substrate and form a thin film.

3.3: Photoemission Spectroscopy

The main method of analysis in the research presented here was photoemission spectroscopy (PES). In PES, a sample is exposed to radiation in order to investigate the properties of the atomic species contained in the sample, resulting in a characterization of the occupied states of the investigated solid or molecule. This technique is based on the photoelectric effect, which was first discovered in 1887 by Hertz [114] and after the experimental setup used by Hertz was later refined [115, 116], Einstein was able to describe the systematics behind it in 1905 [117]. It was in the 1950s, when Siegbahn and co-workers made use of the photoelectric effect in their high resolution photoelectron spectrometer [118-120], which in principle is based on the same setup that was used by Hertz. In the following years, the resolution of such systems was improved to below 1 eV, allowing for the detection of chemical shifts in the electron binding energies, therefore giving it the name 'ESCA' (electron spectroscopy for chemical analysis) [118, 121, 122].

3.3.1: The Theory of Photoemission Spectroscopy

In order to analyze a material with PES, a sample is exposed to monochromatic radiation from a gas-discharge lamp, an X-ray tube or a synchrotron-radiation source.

The incident photons are absorbed by electrons bound within the sample up to a depth of approximately 50 Å (if XPS is employed), liberating the electrons into unoccupied states. The excited electron can then be emitted into vacuum, if the electrons' final state lies above the vacuum level of the material. The kinetic energy E_{kin} of the ejected electron is defined by Einstein's photoelectric equation:

$$E_{kin} = h\nu - E_B - \Phi \qquad (3)$$

Here, $h\nu$ is the photon excitation energy, E_B is the binding energy of the electron in the sample and Φ is the work function of the investigated material. Figure 6 shows the relation between the energy distribution of the electrons of the investigated sample and a PES spectrum. The sample has core levels and a valence band with characteristic emissions (shown on the bottom left). If the sample is a metal, the valence band onset will coincide with the Fermi energy E_F, as seen at the top of the energy distribution of the sample. The onset is separated from the vacuum level E_{Vac} by the work function Φ of the material. A photoelectron that is emitted from a core level with the binding energy E_B, with reference to E_F=0eV, will have a kinetic energy of E_{kin} after exiting the sample. By plotting the number of captured photoelectrons in vacuum vs. their energy an image of the energy distribution in the sample can be generated, where the Fermi edge, valence band emissions, core level emissions and secondary edge can be observed.

The binding energy of the emitted photoelectrons recorded in the spectrum is directly related to the chemical environment within the sample from which they were ejected. Once a photon is adsorbed and excites an electron from its ground state to its final state above the vacuum level, the neutral atom in the sample becomes ionized, leaving behind a photo-generated hole.

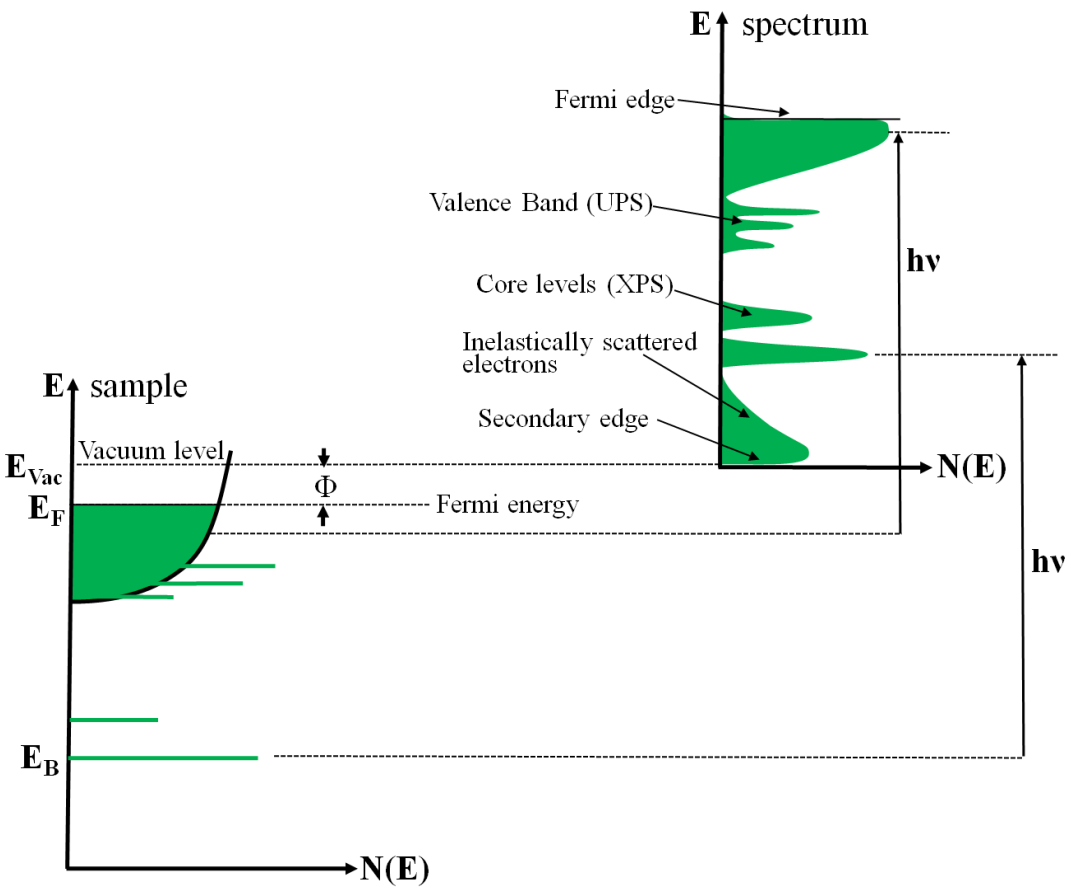

Figure 6: The energy levels in a solid sample and the electron distribution generated by photons at an energy *hv*, depicting the location of the Fermi edge, valence band, core levels and secondary edge in the recorded spectrum.

The remaining electrons in the sample then relax, in order to screen the positive charges from each other (image charge screening), as the positive charge near the nucleus is energetically unfavorable. The photoemission process is approximately one magnitude slower than the relaxation process and as a result, photoemission spectroscopy is sensitive to such final state effects. Photoemission spectra display the binding energies of the ejected photoelectrons in their final state and an example of a typical XPS scan of a Cys-T7 monolayer with its individual emission peaks is shown in Figure 7. The weak valence band emissions of gold can be seen close to the Fermi edge (E_B=0eV), while deeper core level emission features of gold (5p, 4f, 4d, and 4p), carbon (1s), nitrogen

(1s), and oxygen (1s) can be seen at higher energies. The $Au4f_{7/2}$ emission line at 84 eV is often used in PES for calibration purposes in order to achieve reliable results. The visible sloping background in the spectrum is created by secondary electrons, which are inelastically scattered photoelectrons that have lost random amounts of energy through collisions.

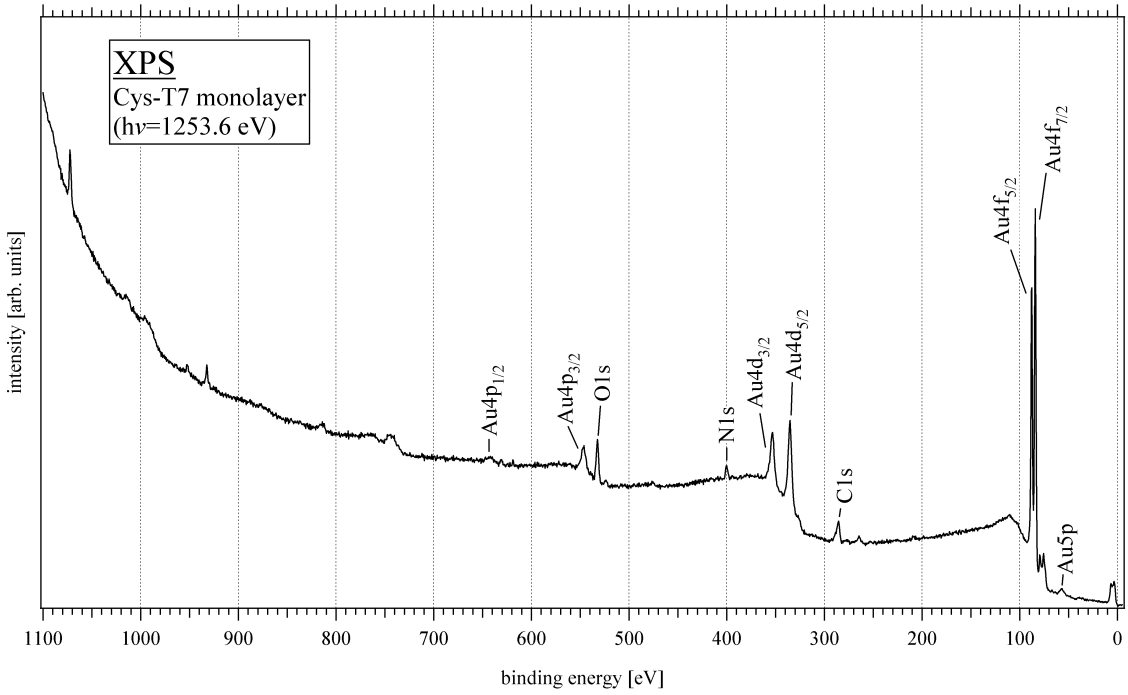

Figure 7: An XP-spectrum of a Cys-T7 SAM depicting the various emissions features

While core level emissions are usually recorded using XPS, UPS is used to measure valence band emissions, or in the case of organic materials, highest occupied molecular orbital (HOMO) emissions and the work function of the sample. It is being frequently employed for the studies of electronic structures of inorganic interfaces and is a complementary measurement technique for XPS [123].

In UPS, electrons close to the Fermi level are excited by UV light and released into vacuum. The emitted UV photons have a lower energy and but a finer energy

resolution, due to the narrower line width of He-emissions. This resolution is essential to record the detailed structure of valence band emission features. Only core levels with low binding energy, also called 'shallow' core levels can be excited with UPS. Although XPS can also be used for investigations of the valence band, its resolution is worse by more than one magnitude [124].

An UP-spectrum of sputter cleaned gold taken with a photon energy of $h\nu$=21.2182 eV is shown in Figure 8. The Au5d valence band emissions of gold can be seen at 2-7 eV above the Fermi edge, followed by a sloping background, as already observed in the XP spectrum above. The final feature of UP-spectra is the sharp cutoff seen on the left in Figure 8, called the secondary edge, and relates to the work function of the sample.

By employing equation (3), the value of the work function can be calculated by using the photon energy of $h\nu$ = 21.2182 eV and the binding energy of the onset, which is equivalent to the intercept of the edge with the energy axis at zero intensity. Additionally, a value of 0.1 eV is added to the calculated work function in order to account for the analyzer broadening of the PES system.

If an organic layer is deposited onto the sample, the UP-spectrum changes and in this case the new onset at high energy corresponds to the emission from the highest occupied molecular orbital (HOMO) of the organic molecule and the low energy cutoff will display the work function of the deposited overlayer.

Using a combination of XPS and UPS during a multi-step deposition sequence of an organic layer, the transition of the substrate work function and electronic structure to

that of the overlayer can be followed. This enables the detailed characterization of the investigated interface.

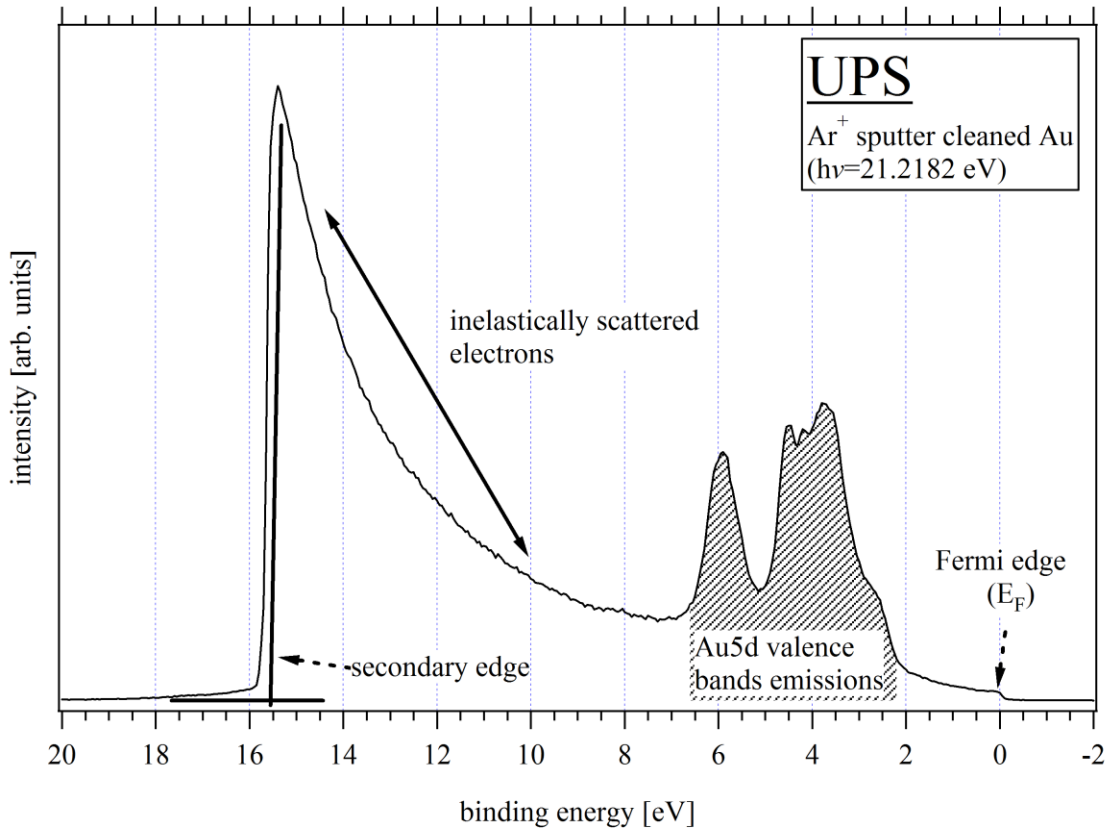

Figure 8: A typical UP-spectrum of sputter cleaned Au showing the work function onset, the valence band emissions and the Fermi edge

It should be noted that the ultraviolet radiation impinging on a sample during an UPS experiment can result in sample charging or even photochemical modifications of the surface. While sample charging has a temporary effect on the work function of the sample, a photochemical reaction will change the work function permanently. In order to determine if the work function of a sample was affected by charging or a surface modification occurred, low intensity XPS (LIXPS) was employed during the measurements as well. LIXPS was specifically developed for this purpose and first used in order to determine the true work function of an environmentally contaminated ITO

surface [125]. During LIXPS, the X-ray gun is operated in the low energetic stand-by mode, which still allows the measurement of the secondary edge, but does not have enough intensity to resolve core level emission features. LIXPS is usually used prior to an UPS measurement and due to its much lower photon flux, no significant work function change occurs within the short amount of time needed for a measurement. Hence the correct value of the work function can be measured. Once the sample is exposed to the magnitudes higher photon intensity of radiation during an UPS measurement and charging or a photochemical modification occurs, these can immediately be observed through a work function shift compared to the initial LIXPS measurement. LIXPS work function values with Kelvin probe measurements [126] show good agreement. This demonstrates that LIXPS yields work function values unaffected by radiation induced effects.

A second LIXPS measurement is usually also performed after UPS measurements. This helps distinguishing between sample charging and photochemical changes on the surface. If sample charging is present, the secondary edge should shift temporarily during the UPS measurements and should revert back after a waiting-period. In the case of a photochemical surface modification however, the secondary edge should shift permanently, i.e. the second LIXPS measurement should be in agreement with the secondary edge from the UPS measurement. Figure 9 shows the common measurement sequence on a Cys-T7 monolayer, demonstrating a charge related shift encountered with UPS.

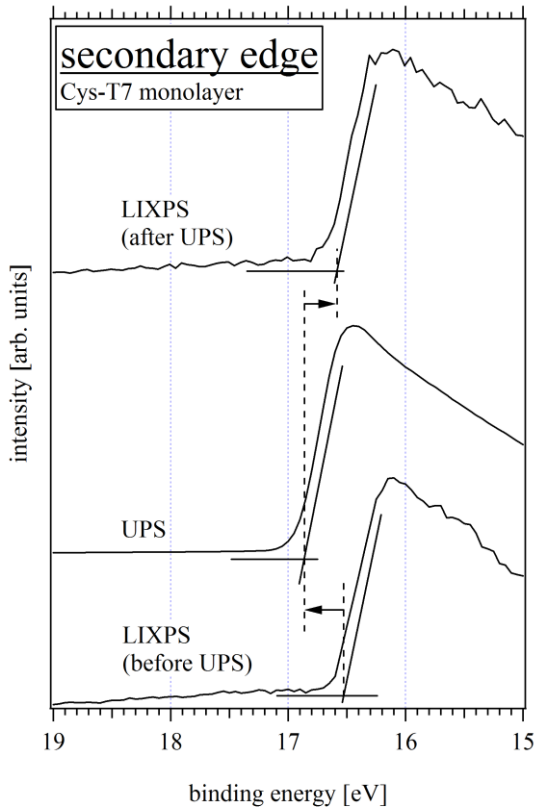

Figure 9: The secondary edge as measured on a Cys-T7 monolayer with LIXPS and UPS. Due to the lower radiation intensity, the initial LIXPS measurement allows for a determination of the secondary edge without having an effect on the work function of the sample. UPS can result in charging of the sample, seen here as a shift of the secondary edge, and the reversion of the secandary edge position to its initial state can be observed with subsequent LIXPS measurements.

3.3.2: Dipole Formation at Metal-Organic Interfaces

The understanding of the carrier injection process between electrodes and organic layers in contact is essential for the enhancement of the performance of organic devices. In the past, this mechanism was characterized by estimating the electronic structure at metal/organic interfaces. It was assumed that the organic layer and the metal electrode have a common vacuum level and the electronic states would align according to the work functions of both materials, as shown in Figure 10.

However, it was shown in the past that the vacuum level cannot be used as the energy reference at such interfaces, as finite vacuum level shifts were observed [127-130]. The observed shifts are a result of the formation of an electronic dipole at the metal/organic interface. In this case the location of the molecular levels with respect to the Fermi level of the metallic substrate differs from the vacuum level alignment.

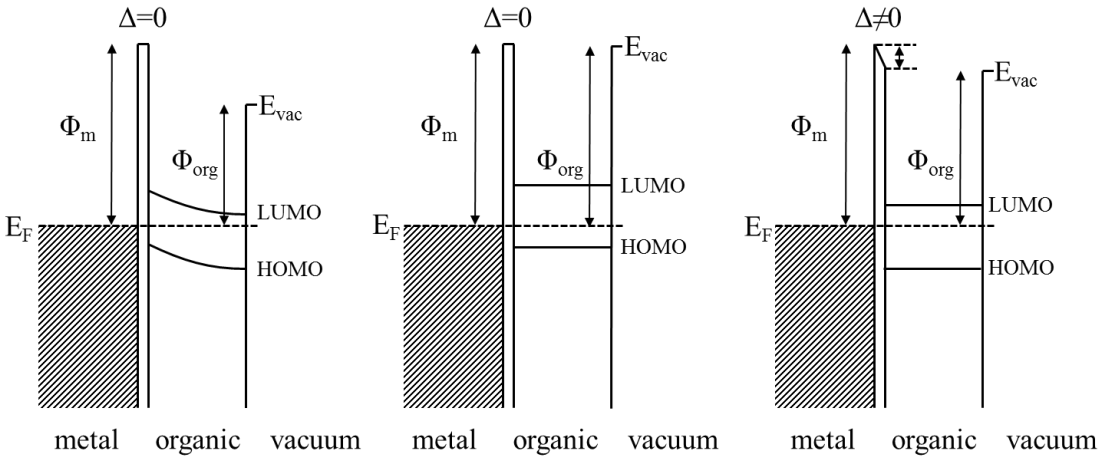

Figure 10: Energy diagrams at a metal/organic interface. The case of Fermi level alignment according to the Schottky-Mott rule is shown on the left, while the case of vacuum level alignment is shown in the middle. The actual observed alignment for metal/organic interfaces with the emerging dipole is shown on the right.

The work function shift observed for thin films of organic molecules can have several origins [131-136], as shown in Figure 11. When no adsorbates are present at the surface of a metal, the tails of the electron wave functions extend into the vacuum region. The resulting charge separation causes an interface dipole (a), which has an effect on the work function of the clean metal substrate [135, 137]. If organic molecules are applied to the surfaces, they push the metal electrons back into the substrate bulk as a result of Pauli repulsion, lowering the electron density of the metal at the surface, and causing a permanent change of the work function. This effect is also called the 'push-back' effect, due to the electrons being driven back into the metal.

The organic molecules themselves can be polarized by an attractive surface potential (b), which also leads to a work function change [135, 138]. It was shown for Xe adsorbed on Cu and Ag, that the 'push-back' effect and polarization together can alter the work function by up to 1 eV [133, 137, 139]. This work function modification strongly depends on the adsorbate and is usually greater for organic molecules [140, 141].

A permanent or adsorption-induced dipole (c) that has a vertical component at the interface originating from the organic molecule can usually shift the vacuum level and consequently the work function of the sample. Additionally, charge transfer between the organic overlayer and the metal substrate (d), or the formation of a chemical bond (e), where the latter one is more common for reactive materials like Ti, In or Sn [142], has an influence on the work function as well.

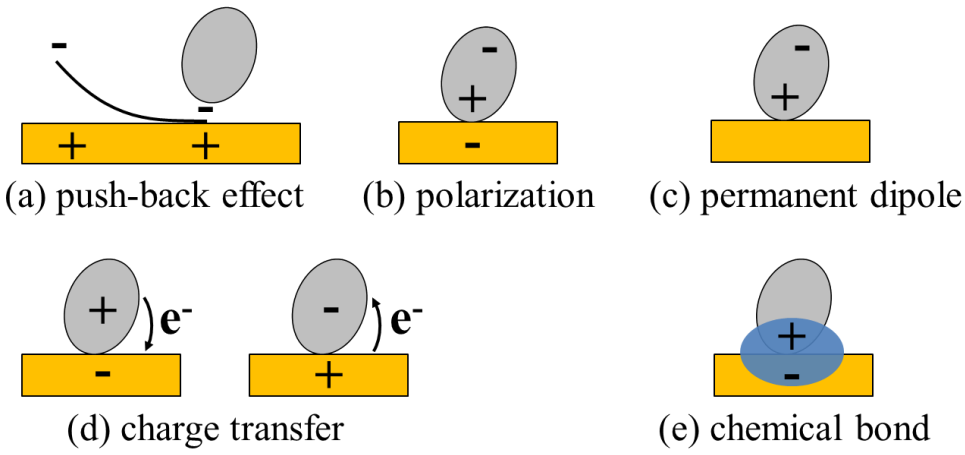

Figure 11: Origins of dipole formations at the substrate/monolayer interface. The push back of the electron tailing of the substrate by repulsion (a), polarization of the molecule through an attractive surface potential (b), permanent dipole as a result of the molecule orientation (c), charge transfer between monolayer and the substrate across the interface (d), chemical interaction leading to a chemically induced dipole (e).

The use of XPS and UPS as complementary measurement techniques allows the investigation of the causes of dipole formation at metal/organic interfaces.

3.3.3: XPS-Based Estimation of Film Thickness

Figure 12 displays the universal electron mean free path plotted as a function of kinetic energy (cf. ref [137]). The mean free path describes the distance that can be covered by an electron before its direction and/or energy is changed due to a collision with other particles. If the electron encounters too many collisions, its energy will drop to a level at which an escape from the solid is impossible. The kinetic energy range of interest, which lies between 10 and 2000 eV, has a mean free path of only a few Å, meaning that PES can only probe a very thin layer of the investigated sample. It should be noted that the mean free path is material-specific. While mean free paths for simple systems like thin films containing one species of atoms or simple compounds can be theoretically calculated, mean free paths of more complex systems, like organic monolayers, have to be identified empirically through experiments.

The fact that photoelectrons can only travel a few Å without undergoing any collisions with other particles means that the sample has to be free from residual contaminants to allow for characterization of surface properties. On the other hand, this particular property can be used for the estimation of the overlayer film thickness. As the photoelectrons can only escape from a certain depth, substrate related emission peaks will decrease in intensity with increasing overlayer thickness, as the photoelectrons originating from the substrate encounter more collisions in the overlayer.

Using the difference in intensity between substrate emission lines before and after a thin film deposition allows for an estimation of the overlayer thickness. The Lambert-Beer law,

$$I = I_0 e^{-\alpha d} \qquad (4)$$

where I is the intensity after the thin film deposition, I_0 the intial intensity of the substrate emission line, α is the mean free path and d the overlayer thickness, describes the attenuation of the intensity. It should be noted that the calculated film thickness assumes a homogenously grown overlayer. Existing pinholes and other defects typically increase the substrate signal in comparison to the signal of the overlayer, which can result in an underestimated thickness of the deposited film.

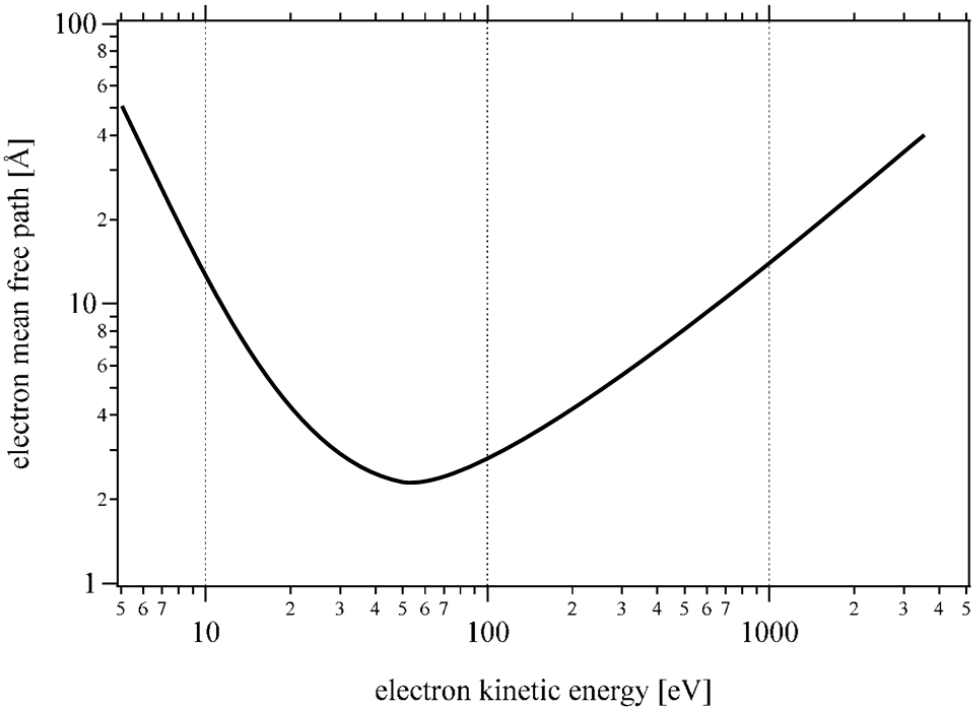

Figure 12: The universal electron mean free path as a function of the kinetic energy. A minimum of 2-5 Å for kinetic energies of 30-100 eV is noticeable.

The intensity of the measured emission lines can also be used to determine the stoichiometry of the investigated sample. Changes in self-assembly conditions (duration, concentration, temperature, etc.) can often lead to deviations in surface coverage, and by evaluating the intensities of overlayer and substrate emission lines, the qualities of separate layers can be directly compared.

3.3.4: Chemical Shifts of Core-Level Binding Energies and Curve Fitting

The chemical environment of an atom affects the energy of a photoemitted electron caused by a change in this local bonding environment. The difference in binding energy between the various chemical states of an atom is referred to as a 'chemical shift' and the direction of these shifts depends on the attractive potential of the nucleus and the repulsive interaction with the surrounding electrons in the material.

Electrons emitted from the C*1s* orbital of a hydrocarbon exhibit a binding energy of approximately 285 eV, for example. C*1s* electrons originating from a C-N bond on the other hand have a binding energy of 286.4 eV while electrons emitted from a carbonyl group reveal a binding energy of approximately 288.4 eV [143], as shown in Figure 13.

The presence of all three bond types in one compound leads to an intricate emission feature, and a more detailed scan of these features is often necessary to obtain accurate measurements. The resolution of the different peaks within the emission feature often requires peak-fitting. Peak-fitting usually starts by removing the inelastic background signal. Then, the separate peaks are fitted with Gaussian-Lorentzian profiles to determine peak positions and the corresponding full width at half-maximum (fwhm) [144].

The fitting procedure does not only allow for the determination of bond types present in the probed sample, but also for a quantitative analysis of the peak ratios. Since the number of emitted electrons is proportional to the amount of atoms within the sample, the ratio between bond types and atoms can be calculated using the area underneath the emission peaks. The area measured underneath the peak has to be multiplied by a factor that takes into account the photoionization cross section of the atoms present in the

sample [145]. Normalizing the peak areas that way allows for direct comparison and quantitative analysis. The comparison of the elemental composition to theoretical values as calculated from the known molecular composition is in general a good indicator for monolayer formation and purity.

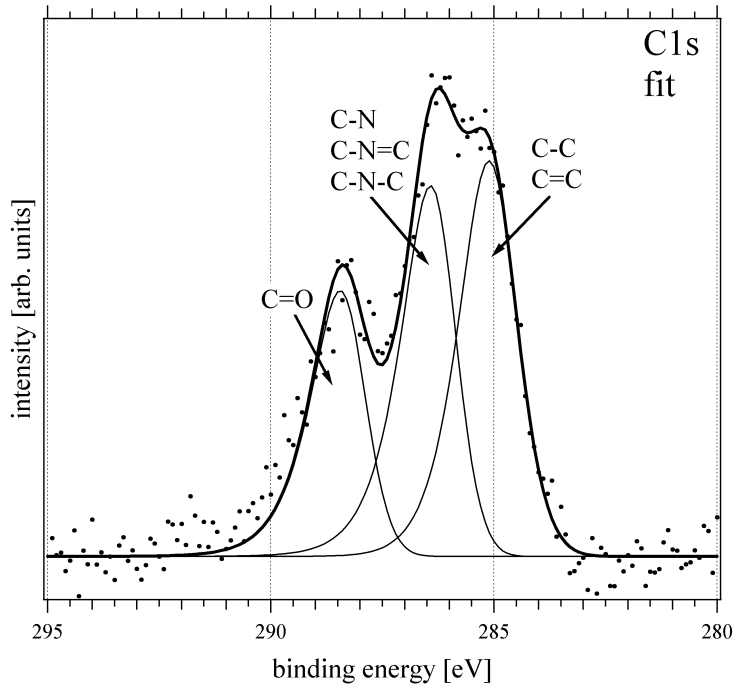

Figure 13: A high resolution scan of the C1s emission feature observed for a Cys-T7 monolayer. The feature can be further resolved by fitting three curves into the signal depicting the different bonds encountered in the molecule.

3.4: Experimental Setup

Surface contamination can have a significant impact on the correct estimation of the electronic structure of the formed SAMs. While it can lead to a wrong assessment of the substrate work function and therefore incorrect interface dipoles, it can also result in oxidation of the functional groups, hindering SAM formation. This requires that the incubation of the prepared substrates is performed in a N_2 atmosphere in a system-attached glove box. The glove box was kept under a slight overpressure during sample

preparation in order to prevent contamination from the ambient environment. A diaphragm pump was used in series with filters that contained active carbon and Drierite drying agent in order to circulate the nitrogen from the glove box and reduce contamination from residual carbohydrates or water. The glove box was directly attached to the vacuum chamber to allow the transfer of the samples into the vacuum chamber without exposure to ambient atmosphere.

3.4.1: Sample Preparation

The substrates used in the presented studies were thin films of Au (100 nm thick), which was deposited on glass slides with an approximately 20 nm thick Ti adhesion layer and these substrates were used for all experiments, with the exception of two incubation experiments in which TPP-CN was deposited on Ag and on Si. The Au substrates were obtained from EMF Corp. (Ithaca, NY) while the Ag substrate was cut from a Ag foil purchased from Alfa Asesar and the Si substrate was cut from a hyperpure polycrystalline silicon wafer purchased from Wacker Polysilicon. The Au substrates and Si wafer were cut into approximately 1 cm x 1 cm pieces and rinsed with acetone, methanol, isopropanol and deionized water in order to remove residual contaminants. The Ag foil was also cut into 1 cm x 1cm pieces and subsequently polished with a fine grain polishing cloth to remove the oxidation layer from the surface. All substrates were mounted in the same manner with mounting screws on stainless steel sample holders which were previously cleaned by sonication in methanol. Grounding of the substrates was ensured through direct contact with the mounting screws. After transfer into the UHV chamber, the substrate surface was sputtered with Ar^+ ions in order to clean the Au substrate surface from ambient atmospheric contamination and remove the oxidation layer from

the Ag and Si substrate surface. For this purpose a SPECS IQE 11/35 ion source was employed which produces Ar^+ ions with a kinetic energy of 5 keV, an emission current of 10 mA, and an Ar pressure of ~4 x 10^{-5} mbar. Detailed information on the incubation procedure for the various monolayers can be found in chapter 4 and chapter 5.

3.4.2: PES System Setup

The PES measurements were performed in a commercially available (SPECS Nano Analysis GmbH, Berlin, Germany) ultrahigh vacuum (UHV) multichamber system that consists of a fast entry lock, two preparation chambers, and an analysis chamber that is equipped with XPS and UPS, as seen in Figure 14, and the base pressure of this system is approximately 2 x 10^{-10} mbar. The analysis chamber contains an X-ray source (SPECS XR50) which was used for XPS as well as LIXPS measurements and an UV source (SPECS UVS 10/35) for UPS measurements. A hemispherical energy analyzer (SPECS PHOIBOS 100) was employed for photoelectron detection during XPS and UPS measurements.

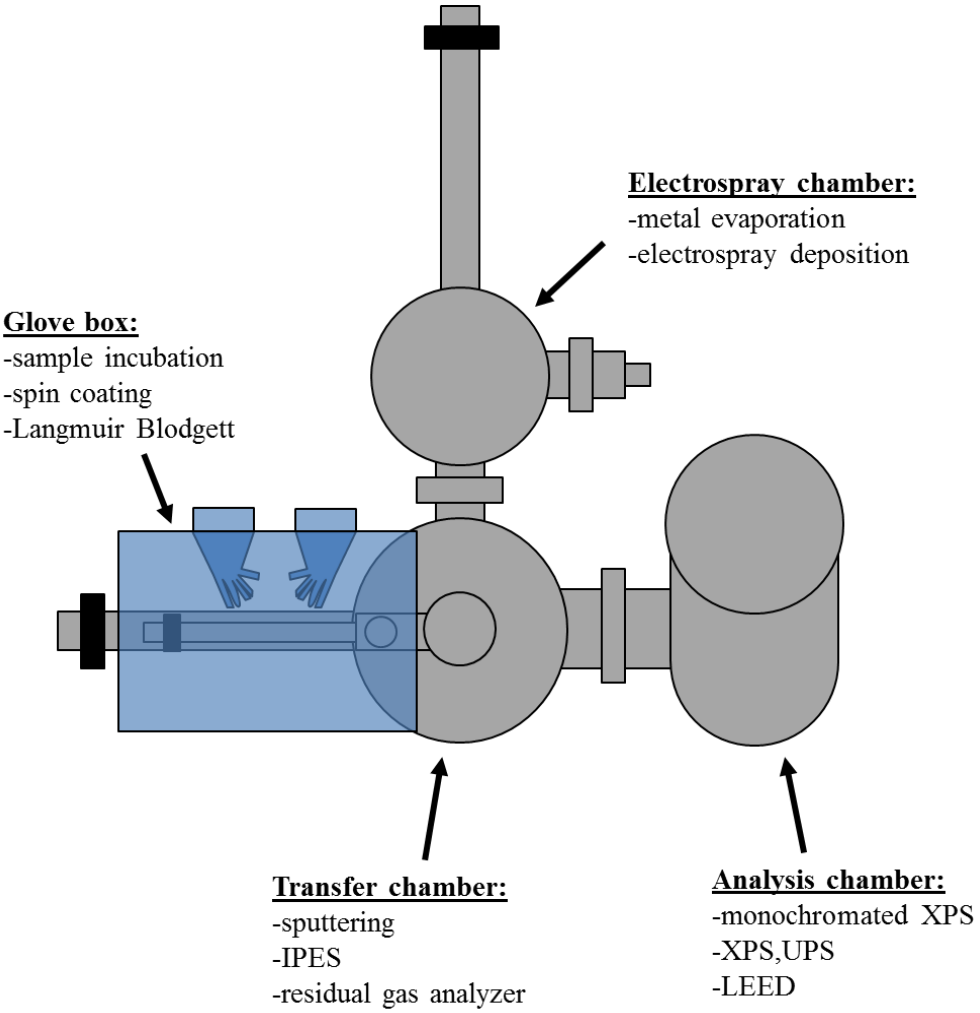

Figure 14: The multichamber analysis system consisting of a transfer chamber, electrospray chamber and analysis chamber.

CHAPTER 4: ELECTRONIC STRUCTURE AT THE INTERFACE BETWEEN AU AND SELF-ASSEMBLED PEPTIDE NUCLEIC ACIDS[1]

Peptide nucleic acid (PNA) is a versatile biomolecule due to the various bonding sites that can be employed for the attachment of functionalized groups and nucleobases. The self-assembly of cysteine appended PNA offers the ability to incorporate these molecules into various organic devices and biosensors. The characterization of the electronic structures of SAMs of cysteine attached 7-mers of PNA with adenine (Cys-A7), thymine (Cys-T7), and no bases (Cys-Bckb7), is the focus of the first part of this chapter. In the second part, two of the three investigated PNA strands were extended through the attachment of a ferrocene group at the tail of the PNA backbone (Cys-A7-Fc and Cys-T7-Fc), identical to PNA strands that are commonly used in electrochemical studies. Electrochemical measurements offer information on the charge transfer characteristics of PNA SAMs, and studying the electronic structure of these SAMs with XPS and UPS can provide clues in terms of what the limiting factors of charge transfer are. The chapter concludes by investigating the impact of the PNA strand orientation on the band line-up of the interface, as incomplete SAMs of low density can contain PNA strands that lie flat on the substrate surface and may offer additional sites for charge

[1] Table 1 and Figures 27 and 28 have been previously published [143] and are utilized with permission of the publisher.

transfer between the substrate and the molecule. To investigate this hypothesis, films of flat lying PNA molecules without a cysteine terminus (PNA-T7 and PNA-Bckb7) were studied and their electronic structure was characterized.

4.1: Experimental

The following experiments were designed to study of the interface between self-assembled monolayers of various PNA strands and Au. First, the Au substrates were cleaned with organic solvents as described in 3.3.1 and inserted into the vacuum chamber. There the substrates were sputter cleaned and analyzed with XPS, LIXPS and UPS. Next, the gold samples were then incubated in PNA solutions with concentrations of 20 μM obtained from Dr. Catalina Achim from Carnegie Mellon University. The solutions were synthesized in her lab following protocols which are explained elsewhere [59, 60, 143]. The samples were incubated for 24h at an approximate temperature of 37˚C. The incubation took place in a glove box attached to the vacuum chamber (see section 3.3). In order to achieve the temperature of 37˚C, the glove box was wrapped in aluminum foil while an incandescent light bulb was placed inside, stabilizing the temperature throughout the incubation period. However, the ferrocene containing PNA solutions were expected to be sensitive to light, and so the vials containing the solutions were wrapped in aluminum foil to provide a dark environment but still allow the solution to be heated by the light bulb.

After incubation, the samples were rinsed with various rinsing agents to resemble the rinsing sequence which is successfully applied in electrochemistry measurements [60]. They were first rinsed with a 50% acetonitrile / 50% deionized water solution, then with deionized water alone, next with sodium perchlorate dissolved in deionized water,

and then again with deionized water. After the rinsing sequence was completed, the samples were dried by applying a lab tissue (Kim Wipe) to one of the corners of the sample while the remaining solvent was evaporated in the nitrogen flow of the glove box. The samples were then moved back into the vacuum chamber, where they were characterized with XPS, LIXPS and UPS.

Figure 15 shows the PNA molecules used for the self-assembly of monolayers in the first part of this chapter. All of these molecules contain a cysteine head-group with an attached thiol moiety. The attachment to the Au surface is driven by the affinity of the thiol group towards the metal and leads to a bond between both (see 2.1.1). The PNA strands contain 7 N-(2-aminoethyl)glycine units, which define the backbone of the molecule, as seen for Cys-Bckb7. The investigated variations of this molecule were strands to which adenine bases (Cys-A7), or thymine bases (Cys-T7) were added.

In addition to the described Cys-Bckb7, Cys-A7, and Cys-T7 molecules, which were terminated with NH_2 ligands, a second group of PNA strands, terminated by ferrocene, was investigated and these molecules are shown in Figure 16. These molecules were previously used in cyclic voltammetry measurements, in which the charge transfer rate between the Au substrate and the ferrocene redox reporter through the PNA molecule was measured [59, 60, 146]. Since the charges are injected directly from the ferrocene group into the PNA molecule, a barrier at this interface is likely the main limitation for charge flow. Therefore, it is of interest to investigate this interface and to determine the charge injection barrier between the ferrocene and the PNA molecule.

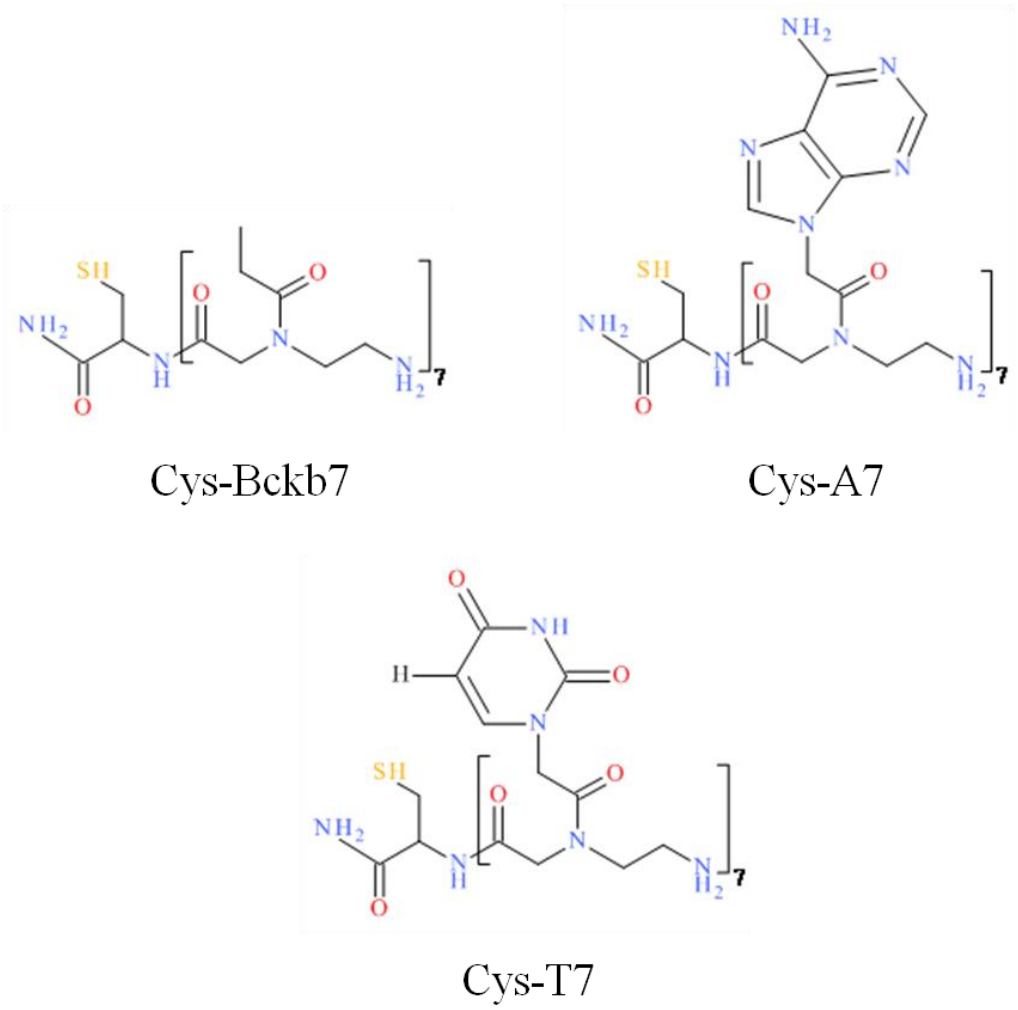

Figure 15: Cysteine appended PNA strands with no bases (Cys-Bckb7), adenine (Cys-A7), and thymine (Cys-T7)

A third series of experiments focused on the investigation of the influence of PNA molecule orientation on the electronic structure of their interfaces. The two investigated PNA strands (shown in Figure 17) were not terminated with either the cysteine head-group or the ferrocene tail-group. This encourages the molecules to lie flat on the surface bound by van der Waals forces and the close proximity between substrate and PNA molecules could lead to charge transfer through the nucleobases.

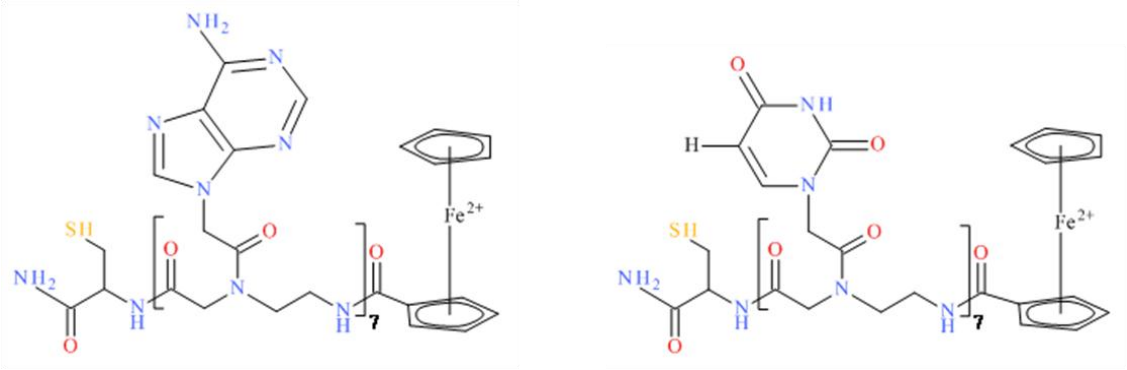

Figure 16: Ferrocene terminated PNA strands of Cys-A7-Fc and Cys-T7-Fc.

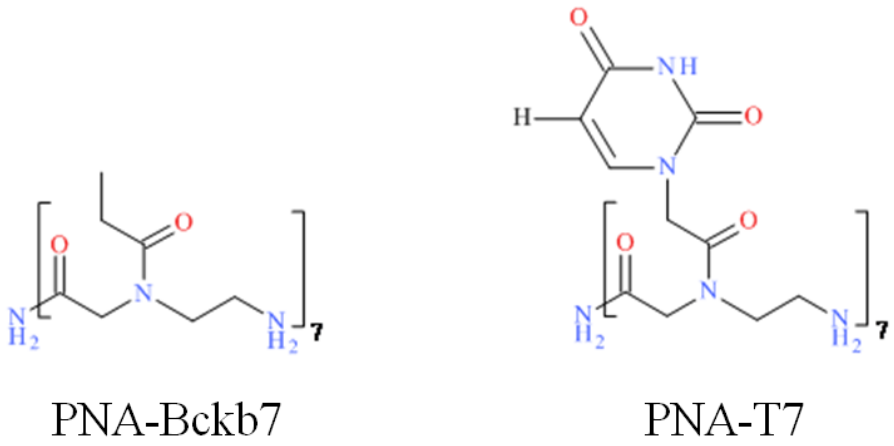

Figure 17: PNA molecules without cysteine head-group or ferrocene tail-group used for experiments focused on the dependence of the electronic structure on the molecule orientation.

In addition to the PES measurements carried out for the Cys-Bckb7, Cys-A7, and Cys-T7 solutions, density of states (DOS) computations were performed by Dr. Alexander Balaeff at Duke University for these molecules as well. The calculations were compared to the experimental results, enabling detailed peak identification in the UP-spectra. The DOS calculations were performed following protocols which are discussed elsewhere [143].

Furthermore, ellipsometry measurements of the Cys-T7 SAM were performed by Dr. Emil Wierzbinski at the University of Pittsburgh. The measurements were conducted in order to compare the XPS derived thicknesses of the SAMs to ellipsometry based results, allowing for an estimation of the error margin for the thicknesses calculated from the attenuation of the XPS spectra.

While DOS calculations were used for comparison of the cysteine based PNA strands, a separate experiment was performed for the ferrocene terminated PNA strands in order to assist in the analysis of the spectra obtained for these monolayers. In this experiment, a clean Au substrate was incubated in a solution of ferrocenyl undecanethiol (Figure 18) in dichloromethane (DCM). The ferrocenyl undecanethiol was obtained from Dojindo Molecular Technologies, Inc. and was handled with caution and only in the nitrogen atmosphere of the glove box, as it can oxidize quickly if exposed to air. The incubation was performed in the glove box as well, although it took place overnight and at room temperature.

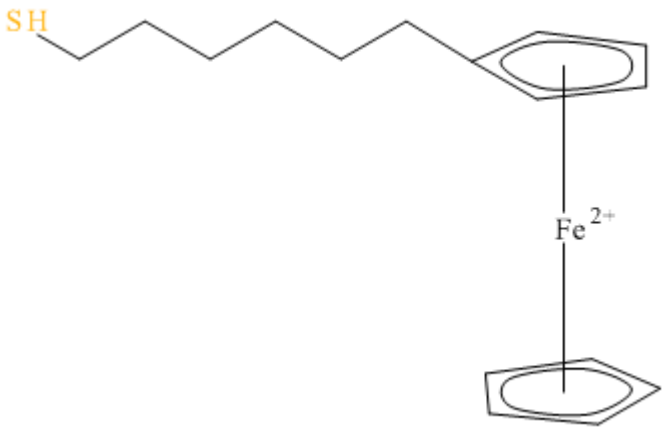

Figure 18: Ferrocenyl undecanethiol used in the ferrocene comparison experiments.

This experiment was designed to determine the XPS related peak positions of ferrocene, as well as its HOMO emission features and hole injection barrier. Since ferrocenyl undecanethiol is a relatively simple molecule, the values obtained for the various peaks should be easily distinguishable and allow for the direct comparison with the PNA related peak locations.

4.2: The Interfaces Between Au and Cys-A7, Cys-T7, and Cys-Bckb7

The interfaces between Au and Cys-A7, Cys-T7, and Cys-Bckb7 SAMs were investigated with XPS and Figure 19 shows the C1s, N1s, and O1s core level emission features of the sputter cleaned Au substrate before (bottom spectra) and after each of the incubations (top three spectra in each plot). The spectra measured for the Au substrate show only very weak C1s emissions at around 285.5 eV, which are attributed to residual contamination of the sample holder assembly.

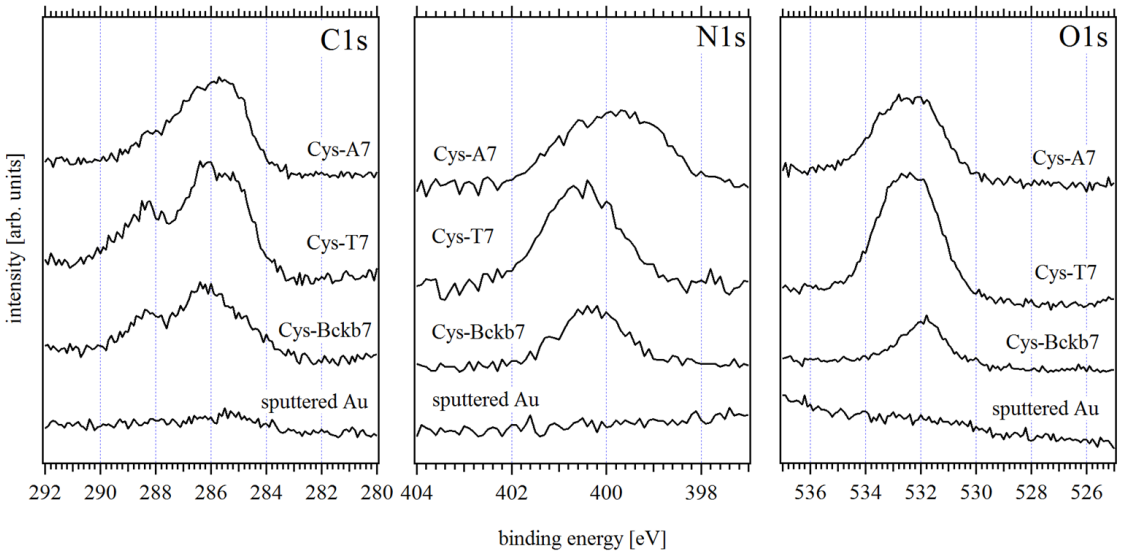

Figure 19: High resolution XPS of the C1s, N1s and O1s emission features of Cys-A7, Cys-T7 and Cys-Bckb7

Changes were observed in the C1s, N1s, and O1s spectral emission features after each of the incubations, indicating a modification of the surface stoichiometry. It is evident that the C1s emission features for the Cys-A7, Cys-T7 and Cys-Bckb7 SAMs consist of at least three distinct emission lines, which are attributed to the peptide backbone and the adenine and thymine bases. When comparing the results to earlier XPS measurements of cysteine monolayers on gold [147] and uracil bases on highly oriented pyrolytic graphite (HOPG) [148, 149], the lines can be assigned as follows: While the high-binding energy emissions at about 288 eV are related to the C=O bonds found in the PNA backbone and thymine bases, the central component at around 286 eV corresponds mostly to the C-N bonds. The main component at about 285 eV is related to C=C bonds in the adenine and thymine bases, but also to C-C bonds in the PNA backbone. As a result, the 285 eV line exhibits a higher intensity in the Cys-A7 and Cys-T7 spectra than in the Cys-Bckb7 spectrum.

The N1s emission features obtained for the Cys-T7 and Cys-Bckb7 SAMs can be split into two components, while the emission feature of the Cys-A7 SAM likely consists of three. The main component is a strong emission line at about 400 eV, which is related to pyrrolic (-NH-) nitrogen [150, 151], the amine groups located at the N-terminus of the PNA and, to a lesser degree, the cysteine group [152]. Since adenine contains additional iminic (-N=) sites with emission lines usually found at lower binding energies [153, 154], a third line can be located at around 399 eV for Cys-A7. The weak component at about 401 eV found in all three SAMs likely accounts for the -CN- bonds in the backbone and bases [150, 154].

The O1s spectra of all three SAMs seem to contain two emission lines at approximately 532 and 533 eV, judging by the large widths of the peaks. Since only the backbone and thymine bases contain C=O bonds it is likely that the 533 eV component arises from adsorbed water. This is in agreement with values published in the past [155]. However, it should be noted that this line is less intense in the Cys-Bckb7 related spectrum, indicating that less water was adsorbed here.

Figure 20 shows the S2p and Au4f emission spectra measured on the formed SAMs, as well as the clean Au sample. Interestingly, none of the films show S2p related emissions, although a thiol group is present in the cysteine head-group. This is most likely an indication that the thiol moieties are oriented down towards the Au surface. The absence of S2p emissions at about 162 eV [147] is consistent with previous studies of Cys-T7 SAMs formed on Au electrodes [60], which showed that the SAMs contain about 90% 'standing up' molecules and 10% 'lying down' molecules. Additionally, the S2p signal should be weak, even in the 'lying down' molecules, due to the low photoionization cross section of S atoms [145]. Furthermore, the S atoms represent less than 1% of the atoms present in the PNA molecules, i.e. their signal is close to the detection limit of XPS.

The Au4f signal was attenuated for each of the SAMs due to the partial absorption of the photoelectrons emitted from the Au substrate by the molecular overlayers. The thicknesses of the deposited SAMs can be calculated from the attenuation of the Au4f spectra (see section 3.3.3). The intensities of the Au4f core level emission at 84 eV were used for the calculations with an estimated mean free path of 36 Å [156]. The intensity ratios between the clean surface and SAMs determined from the peak intensity of the

$Au4f_{7/2}$ core level emission were 0.41 for Cys-A7, 0.45 for Cys-T7, and 0.34 for Cys-Bckb7. On the basis of these values the average film layer thickness was determined to be 32 Å for Cys-A7, 29 Å for Cys-T7 and 38 Å for Cys-Bckb7.

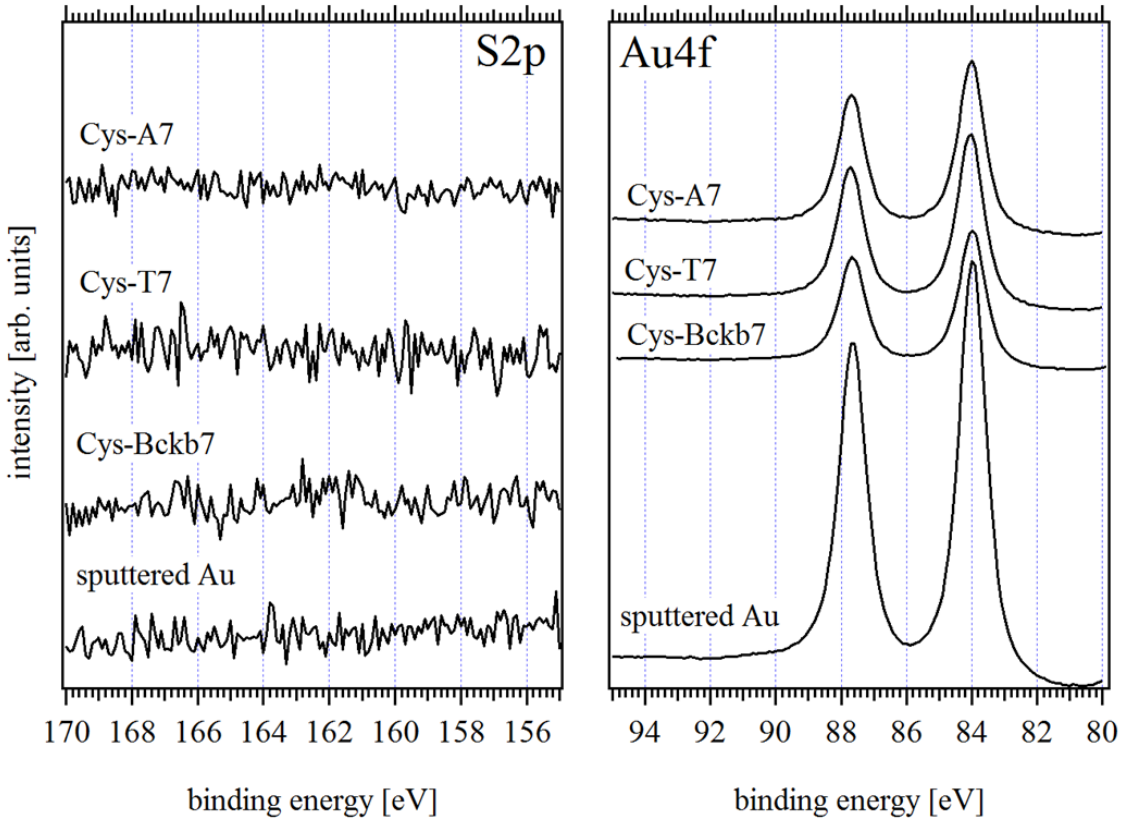

Figure 20: High resolution XPS of Au4f and S2p for the three investigated monolayers. While the Au4f related emission features decreased in intensity due to the PNA overlayer, the S2p area does not exhibit any emission features, indicating that the sulfur succesfully bonded with the gold substrate and the PNA overlayer completely attenuated the S2p related emission.

The larger thickness result for the Cys-Bckb7 film suggests that this SAM is also denser than the Cys-A7 and Cys-T7 SAMs. Since nucleobases are absent in Cys-Bckb7, this could allow the PNA molecules to arrange in a straighter conformation than the helical conformations expected for Cys-A7 and Cys-T7, resulting in denser packing. The larger density of the Cys-Bckb7 layer is also in agreement with the smaller amount of water detected in the SAM, based on the O1s spectrum in Figure 19.

As explained earlier on in section 3.3.3, these film thickness values only represent approximations of the true SAM thickness, since it is assumed in the calculations, that the film is perfectly flat and homogeneous. This is not always true and pinholes and other defects increase the substrate signal. This may result in an underestimated thickness of the SAM. However, the above evaluation was confirmed by ellipsometry measurements carried out on a Cys-T7 SAM , which yielded a thickness of 33 ± 6 Å. Ellipsometry measurements are commonly used for thickness evaluations of SAMs and the agreement between XPS and ellipsometry derived thickness values demonstrates the validity of XPS for thickness assessments on SAMs.

Figure 21 shows the Gaussian-Lorentzian fits for the C1s spectra of Cys-A7 (left), Cys-T7 (middle), and Cys-Bckb7 (right). The C1s spectrum of Cys-A7 exhibits three emission lines which can be located at 285.2 eV, 286.6 eV, and 288.3 eV, while the C1s spectrum for Cys-T7 consists of three emission lines at 285.1 eV, 286.4 eV, and 288.4 eV. The Cys-Bckb7 emission also contains three lines located at 284.9 eV, 286.4 eV, and 288.3 eV. The low binding energy lines at 285.2 eV, 285.1 eV, and 284.9 eV respectively are attributed to the carbon atoms in C-C and C=C bonds. Since the latter bonds are only present in the adenine and thymine bases, the resulting peak is higher in the Cys-A7 and Cys-T7 spectrum than in the Cys-Bckb7 spectrum. The two lines at higher binding energies (286.6 eV and 286.4 eV) are characteristic of carbon in C-H, C-N, and C-N=C bonds [148] and in C=O bonds (the 288.3 eV/288.4 eV lines) [107, 148]. Table 1 summarizes the energies and assignments of the C1s, N1s and O1s lines.

Table 1: Emission lines of the Cys-A7, Cys-T7, and Cys-Bckb7 monolayers in eV. (Reprinted (adapted) with premission from [143]. Copyright 2011 American Chemical Society)

	Cys-A7	Cys-T7	Cys-Bckb7	assignment
C1s	285.2	285.1	284.9	C in C-C and C=C
	286.6	286.4	286.4	C in C-H, C-N and C-N=C
	288.3	288.4	288.3	C in C=O
N1s	399			N in iminic N (-N=)
	399.8	400	400	N in NH_2 and peptide bond
	400.7	400.9	400.6	N in C-N
O1s	531.8	531.8	531.6	O in peptide bond
	533.2	533	532.4	O in water

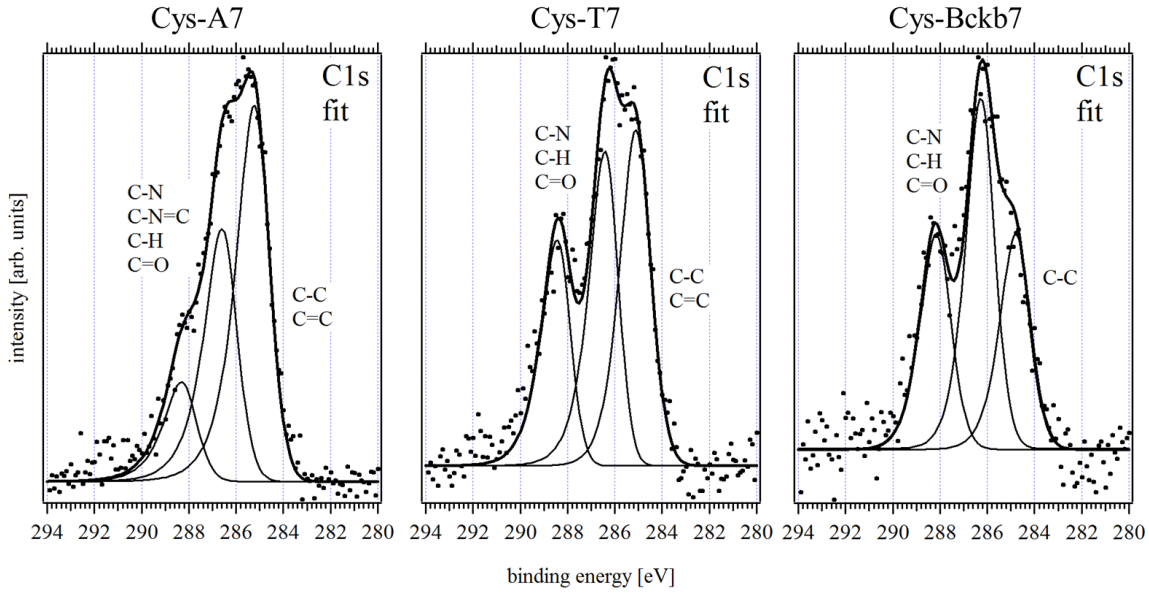

Figure 21: Gaussian-Lorentzian fits of the C1s emission features of Cys-A7, Cys-T7, and Cys-Bckb7.

The fitted N1s spectra for Cys-A7, Cys-T7, and Cys-Bckb7 are shown in Figure 22. All three spectra contain an emission line at 400.7 eV (Cys-A7), 400.9 eV (Cys-T7), and 400.6 eV (Cys-Bckb7), which are attributed to nitrogen in C-N bonds. The spectra

also contain a line at 399.8 eV (Cys-A7) and at 400 eV (Cys-T7 and Cys-Bckb7), which originates from the nitrogen in the amino and amide groups of PNA [107, 148]. While the 400.9 eV line of the Cys-T7 spectrum has a higher intensity than the 400.6 eV line in the Cys-Bckb7 spectrum, reflecting the presence of the nucleobases, a third line is present in the Cys-A7 spectrum at 399 eV, as a result of the iminic (C-N=C) bonds only present in adenine. The assignments of the N1s emission lines discussed above are all in good agreement with previous results published by Mateo-Marti et al. [157].

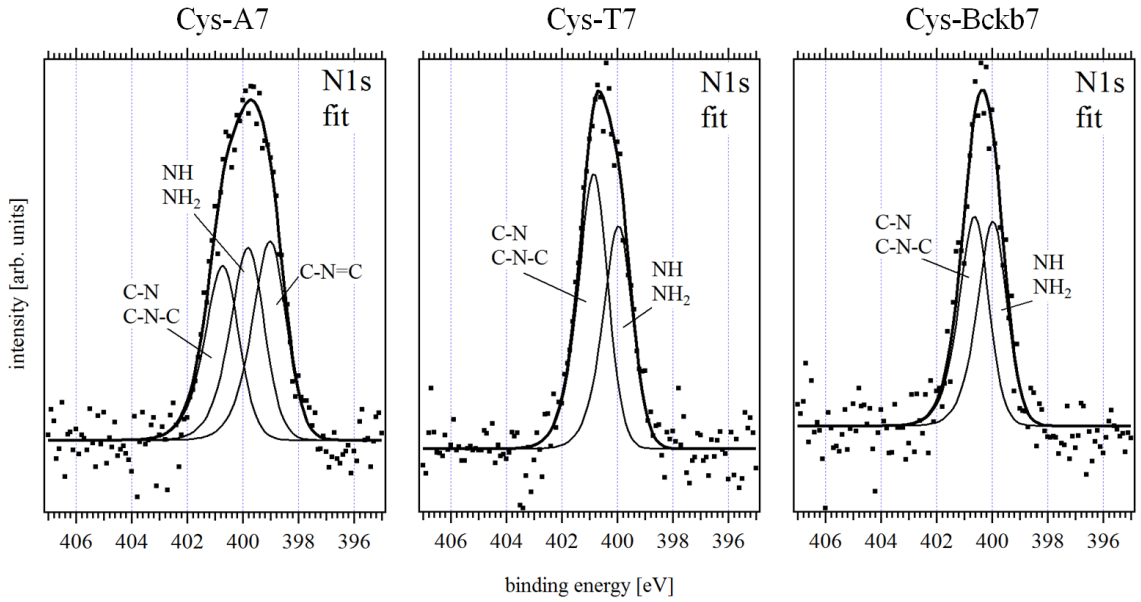

Figure 22: N1s emission features of Cys-A7, Cys-T7, and Cys-Bckb7 fitted with Gaussian-Lorentzian functions.

The O1s emission features were also fitted with Gaussian-Lorentzian peaks and the results are shown in Figure 23. All three emission features can be split into two lines, located at 531.8 eV and 533.2 eV (Cys-A7), 531.8 eV and 533 eV (Cys-T7), and at 531.6 eV and 532.4 eV (Cys-Bckb7). The intense lines at lower binding energies are attributed to the oxygen atoms in the peptide bonds of the PNA, whereas the weaker lines at higher

binding energies are attributed to the residual water present in the PNA layer [155]. The water related peak is higher in the Cys-A7 and Cys-T7 spectra in comparison to the Cys-Bckb7 spectrum, which indicates that a larger amount of water present in the SAMs containing adenine and thymine. One possible explanation could be the lower PNA surface density in the Cys-T7 and Cys-A7 films, as was discussed above based on the Au4f thickness calculations. Furthermore, adenine and thymine bases offer more hydrogen bonding sites due to their polar moieties in addition to those found in the neutral backbone [158], which could lead to more water adsorption. The variations in the binding energies of the H_2O-related peak (533.2 eV for Cys-A7 and 533 eV for Cys-T7 vs 532.4 eV for Cys-Bckb7) indicate differences in charge and/or polarization of the PNA-bound water molecules in the Cys-A7, Cys-T7 and Cys-Bckb7 systems. However, this interpretation should be considered in light of the overall measurement accuracy of ±0.1 eV, and uncertainties resulting from the fitting process.

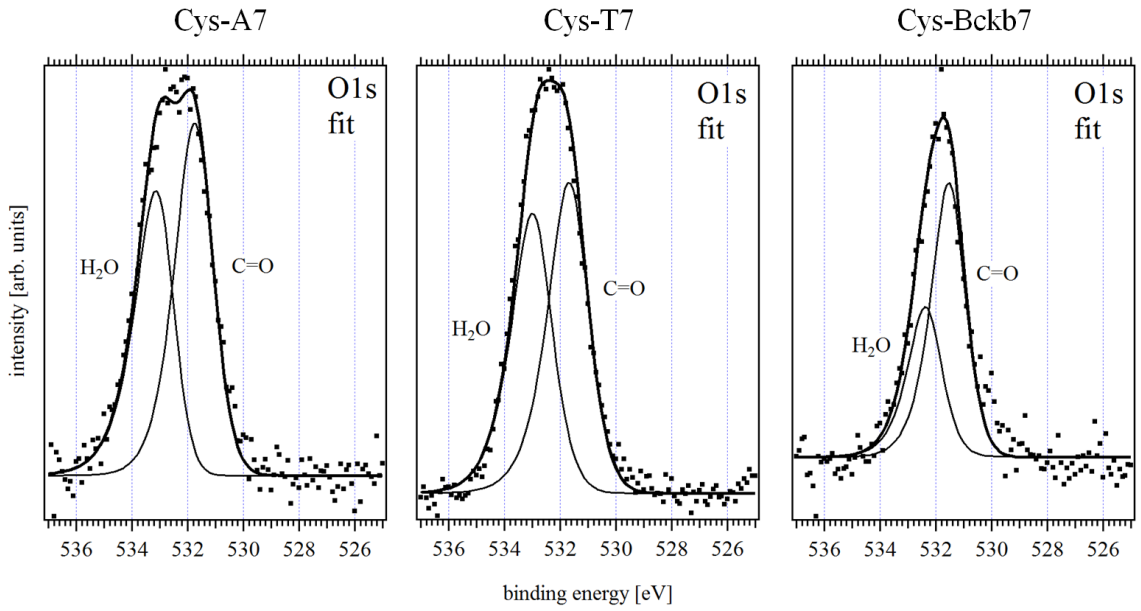

Figure 23: Gaussian-Lorentzian peak fits for the O1s emission features recorded for Cys-A7, Cys-T7, and Cys-Bckb7.

Figure 24 displays the UP-spectra measured in conjunction with the XPS characterization. The center graph shows the full spectra before and after each of the three incubations of the sputter cleaned gold substrate. The low binding energy edges of the spectra located directly below the Fermi energy (0 eV) correspond to the valence bands/highest occupied MOs and are shown in the right panel. The binding energies of the secondary edges of the spectra, which are shown on the left, allow the determination of the work function of the sample.

The incubations resulted in intense spectral lines at low binding energies which correspond to the frontier orbital states of the deposited molecules, while strongly attenuating the Au valence bands emissions at 2-7 eV below the Fermi level. At the same time the secondary cutoffs shifted to higher binding energy for each of the monolayers, indicating a decrease in the work function due to the interaction between the Au surface and the molecular films. The work functions obtained from the secondary edge onsets as measured by LIXPS (not shown here) are listed in Table 2.

Table 2: Work functions and highest occupied molecular orbital (HOMO) onsets of the Cys-A7, Cys-T7 and Cys-Bckb7 SAMs in eV.

	Au	Cys-A7	Cys-T7	Cys-Bckb7
Work function	5.4	3.95	4.32	3.84
HOMO onset		2.24	2.81	3.23

The thickness values obtained from the attenuation of the Au4f core emission lines are consistent with the UPS data. Since UPS has a higher surface sensitivity (~10-20 Å) because of the lower energy of the emitted photoelectrons, the mean free path of these electrons is shorter than typical XPS electrons. The Au emissions seen in

Figure 24 are significantly suppressed in the UP-spectra of the three deposited SAMs, which indicates that the SAM thickness must be more than 20 Å.

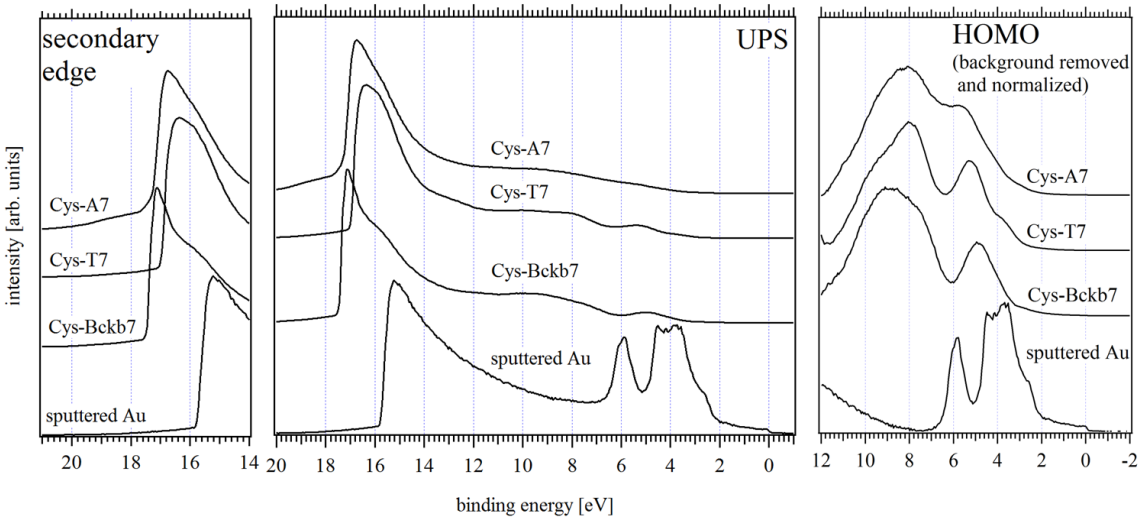

Figure 24: UP-spectra measured before and after incubation in Cys-A7, Cys-T7, and Cys-Bckb7 solution, as indicated. The full spectra are shown in the center. The normalized secondary edge and the conduction bands/HOMO emission range after removal of the inelastic background are shown on the left and right, respectively.

From the analysis of the UP-spectra before and after the formation of the SAMs information about the electronic structure of the Au/Cys-A7, Au/Cys-T7 and Au/Cys-Bckb7 interfaces can be obtained. The hole injection barrier between the organic monolayer and the gold substrate can be determined directly by measuring the difference between the highest occupied molecular orbital (HOMO) onset and the Fermi edge of the clean substrate. The HOMO cutoff energies can be extracted from the background-removed spectra of the three interfaces (shown in Figure 25), resulting in hole injection barriers Φ_h of 2.24 eV for the Au/Cys-A7 interface, 2.81 eV for the Au/Cys-T7 interface, and 3.23 eV for the Au/Cys-Bckb7 interface. It should be noted that hole injection into the PNA HOMO may also proceed through a 'stepping stone' state at 1.5 eV. This 'stepping stone' is attributed to the bonding orbital of the thiol-Au bond, which was

investigated in the past [147, 159]. Due to the surface sensitivity of the UPS measurements, this interfacial state cannot be detected directly, as the signal of the thiol moiety is mostly attenuated by the top part of the PNA molecule.

The computed theoretical DOS spectra are shown in Figure 25 in comparison to experimental spectra, and were shifted along the x-axis in order to achieve the best overlap. The adjustment of the energy axis of calculated DOS in order to match experimentally determined DOS is a standard practice, since ab-initio DOS calculations have limited accuracy with regard to absolute energy values. Additionally, the interface dipole between the gold substrate and the PNA molecules has an influence on the molecular energy reference point in the experiment and depends on the particular substrate, which is not included in the calculations.

The calculated and measured spectra are in good agreement between binding energies of 2 eV and 6 eV, which relates to the highest-energy occupied electronic states of PNA. The number and height of the theoretical DOS peaks differ from the experimental data at energies above 6 eV. The experimental spectrum of Cys-A7 shows one high, broad peak at 8 eV, while the Cys-T7 related spectrum shows a similar peak at 8 eV, with an additional small shoulder at around 9.5 eV. The computed spectrum of Cys-A7 shows a low intensity peak at slightly higher energies than measured in the experiment. On the other hand, the computed spectrum of Cys-T7 shows two low intensity peaks at approximately the same energies as obtained from the experiment. The Cys-Bckb7 spectrum shows one high, broad peak located at around 9 eV with a shoulder at 7.5 eV, similar to the Cys-T7 spectrum, while the computed spectrum shows two lower intensity peaks, one at 7.5 eV and the other at 9 eV with a shoulder at 9.5 eV. The most

likely reason for the discrepancies between computed and measured spectra is that water molecules were excluded from the quantum mechanical computations.

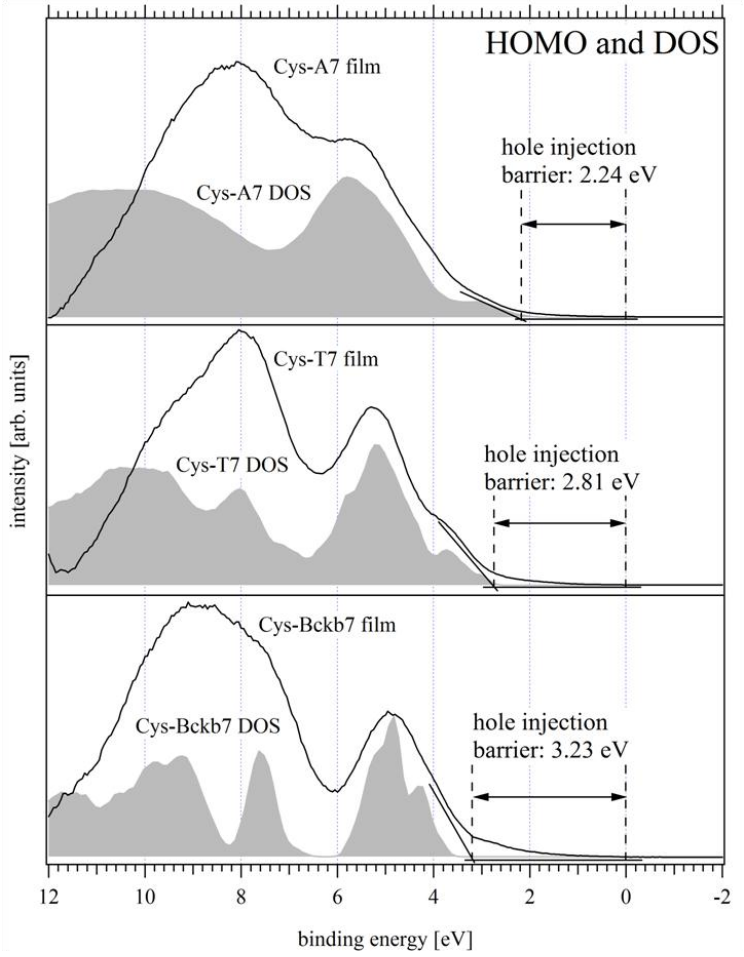

Figure 25: HOMO regions of the Cys-A7, Cys-T7, and Cys-Bckb7 SAMs after inelastic background removal. The superimposed gray filled spectra represent the DOS curves from molecular dynamics simulations. The HOMO spectral features from the measured UP-spectra are in close agreement with these calculations.

The experimental DOS includes the electronic states of adsorbed residual water (as seen in Figure 19) and the presence of water in the PNA films should lead to a broadening of the PNA DOS peaks. The PNA conformations in the film could also exhibit more variety than the straight-axis P-helical conformation, which was sampled in the simulations. Therefore, more coupling interactions between molecular orbitals,

including those on different PNA molecules, would result in an increase of orbital delocalization and a broadening of the related orbital energies.

The measured hole injection barriers between the Au Fermi level and the molecular HOMOs are 2.24 eV for Cys-A7, 2.81 eV for Cys-T7, and 3.23 eV for Cys-Bckb7 (see above). The electron injection barriers defined by the lowest unoccupied molecular orbitals (LUMO) at these interfaces can be estimated from the hole injection barriers and the theoretical values for the HOMO-LUMO gap of the molecular overlayer, which were 5.84 eV for Cys-A7, 6.69 eV for Cys-T7, and 8.15 eV for Cys-Bckb7, as determined by the onsets of the theoretical HOMO and LUMO positions.

It should be mentioned that these HOMO-LUMO gap values represent gaps of a neutral molecule; charge transfer across the interface, however, depends on the 'transfer gap' between the corresponding HOMO and LUMO polaron states. The polaron states represent the HOMO of a positively (+1) and the LUMO of a negatively (-1) charged molecule. In order to estimate the according transfer gap values, the electron and the hole polaron energy has to be subtracted from the theoretical HOMO-LUMO gap. The hole injection barriers, as determined through the UPS measurements, already include the polaron energy since the final state of photoemission spectroscopy measurements is the positive ion in its (electronically) polarized surrounding. Therefore the corresponding LUMO can be calculated directly from this value, if the transfer gap is known.

The polarization energy of DNA can be used as an estimate for the corresponding energy for PNA, as it was shown by Conwell et al. that the charge of the ribose diphosphate backbone of DNA does not affect the hole polaron binding energy because the effect of static polarization is already accounted for in the binding energy of the

ground state HOMO [160]. Based on these published calculations, the hole polaron binding energy for a 'dry' double-stranded DNA is approximately 0.2 eV [161, 162] and about 0.13 eV for a dry single-stranded DNA of alternating G and T bases [163]. The polarization from residual water results in an increase of the hole polaron binding energy by about 0.5 eV [161] to 0.6 eV [162]. The bases on a single strand are more exposed to water than those on a double strand, which leads to the assumption that the polaron binding energy of a solvated single-stranded DNA is at least similar to the 0.6 eV of double-stranded DNA. The PES measurements show that the formed SAMs are partially solvated, hence, the average hole polaron binding energy should be in between the values for the dry and solvated molecules. The average of 0.37 ± 0.24 eV for the above mentioned values could therefore be a reasonable estimate. Taking into account an error of ± 0.1 eV for the energy values extracted from the photoemission spectra, due to analyzer broadening, and assuming that the electron and hole polarons have a similar binding energy as the peptide backbone and that nucleobases have a similar screening ability, the HOMO-LUMO transfer gap can be estimated as $5.1 \pm ((0.24)^2 + (0.1)^2)^{1/2}$ eV= 5.1 ± 0.26 eV (assuming independent uncertainties) for Cys-A7, 5.95 ± 0.26 eV for Cys-T7, and 7.41 ± 0.26 eV for isolated Cys-Bckb7 molecules surrounded by a thin shell of solvent.

The emerging polarons experience an additional energy loss in the PNA molecules, as the molecules are in close contact with the Au surface. PNA surrounded by a solvent is exposed to much a smaller dielectric screening in comparison to the metal surface. This causes an effect named 'polarization barrier lowering' [164, 165] or also 'final state screening', a term used more commonly in photoemission spectroscopy [166-

168]. This additional energy loss results in lowering of both, the hole and the electron injection barriers, by an amount that is dependent on the difference between the screening capabilities of the molecule and of the substrate surface. Measurements performed on ribonucleic acid (RNA)/Au interfaces demonstrated that the decrease of the polarization barrier can be as high as 1.0 ± 0.1 eV per either electron or hole injection barrier [164]. If one assumes that the investigated PNA molecules exhibit screening abilities similar to that of RNA, then the estimated HOMO-LUMO transfer gaps E_g would be reduced to 3.1 $(((0.24)^2 + (0.1)^2 + (0.1)^2)^{1/2}$ eV = 3.1 ± 0.28 eV for Cys-A7, 3.95 ± 0.28 eV for Cys-T7, and 5.41 ± 0.28 eV for Cys-Bckb7 in the vicinity of the Au surface.

Based on the determined work functions, hole injection barriers and transfer gaps, the orbital line-ups at the Au/Cys-A7 (Figure 26), the Au/Cys-T7 (Figure 27) and the Au/Cys-Bckb7 (Figure 28) interfaces were determined. The electron injection barriers estimated from the transfer gaps and hole injection barriers result in values of 0.3 $(((0.24)^2 + (0.1)^2 + (0.1)^2)^{1/2}$ eV = 0.3 ± 0.28 eV for Cys-A7, 1.14 ± 0.28 eV for Cys-T7 and 2.18 ± 0.28 eV for Cys-Bckb7. This means that the injection barriers between the PNA molecules and the Fermi level of the Au surface are significant for electrons and holes, even if hole injection would take place through the 'stepping-stone' state mentioned earlier. However, the Au/Cys-A7 interface displays a relatively low electron injection barrier in comparison to Cys-T7 and Cys-Bckb7, which should promote electron injection.

At this point it should be noted that the Fermi level shown in the band line-ups below does not represent the bulk value. This level is defined by the orbital line-up and the Fermi level of the Au substrate, as free charge carriers are not present in the PNA

layers. This would mean that the SAMs exhibit depletion layer widths, which exceed the thickness of the SAM by far.

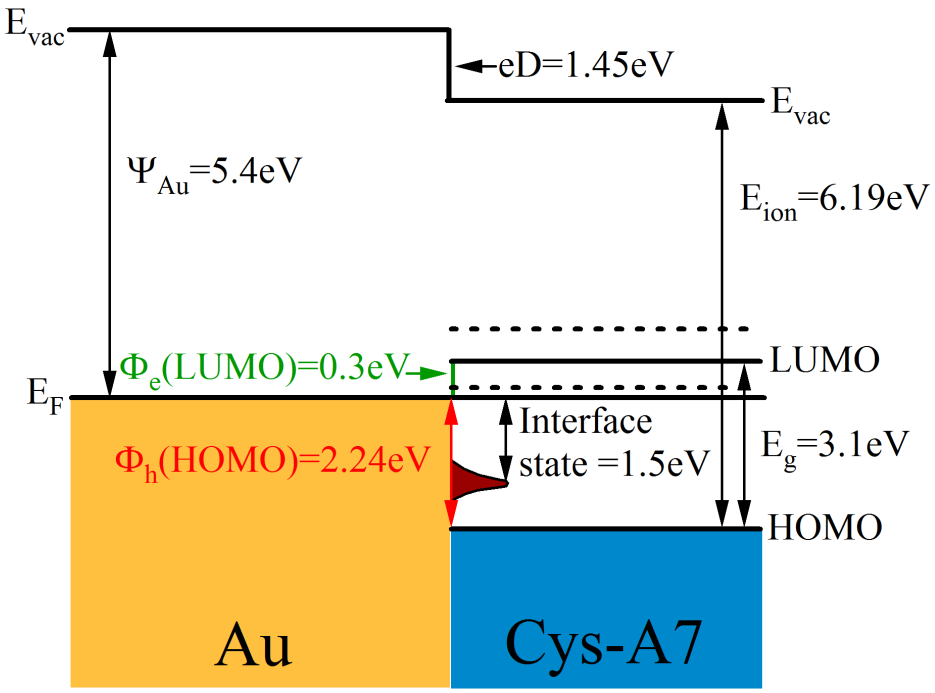

Figure 26: Band line-up of the Cys-A7 interface as determined from the UPS measurement and the theoretical calculation. The dotted lines indicate the uncertainty of the estimated LUMO energy.

The ionization energies displayed in the band line-ups were determined for each interface by adding the HOMO binding energy to the work function as determined from the UP-spectrum. This resulted in values of 6.19 eV for Cys-A7, 7.13 eV for Cys-T7 and 7.07 eV for Cys-Bckb7. The E_{ion} values are only valid in the direct vicinity of the Au surface, as they are affected by the further polarizability of the Au surface. The ionization energy of isolated molecules are likely about 1 eV larger than the above values, if the estimation for the lowering of the binding energy by the polarization of the Au surface, as discussed above, is correct.

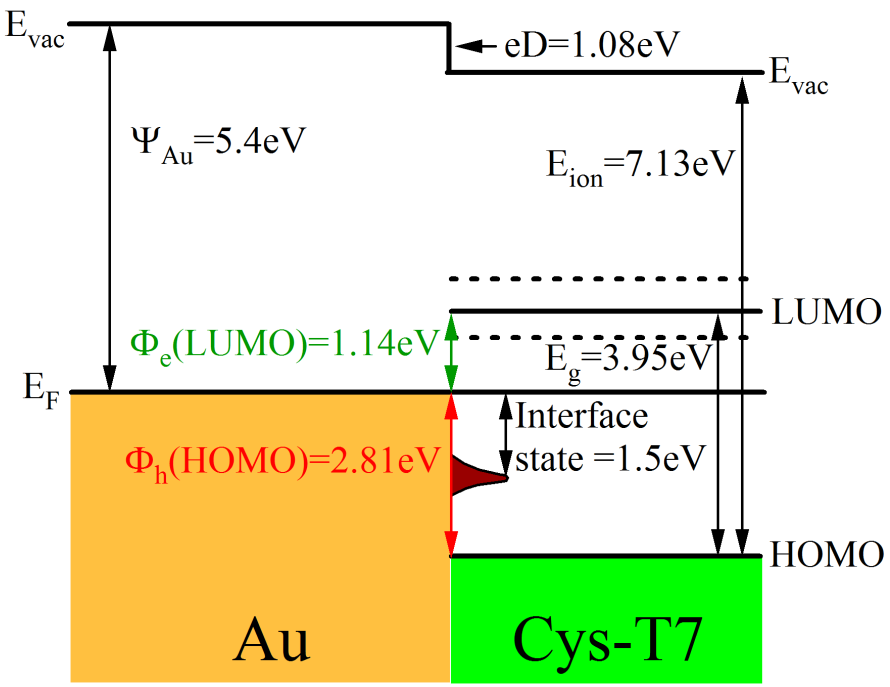

Figure 27: The orbital line-up of the Cys-T7 interface as determined by the UPS measurement in conjunction with the theoretical calculation. The dotted lines display the uncertainty of the estimated LUMO energy, as mentioned in the text. (Reprinted (adapted) with permission from [143]. Copyright 2011 American Chemical Society)

By comparing the work functions of the formed PNA SAMs and the work function of 5.4 eV measured for the sputtered cleaned Au surface prior to deposition, the interface dipoles can be determined from the difference between the values before and after incubation. These comparisons led to interface dipole values 1.45 eV for Cys-A7, 1.08 eV for Cys-T7 and 1.56 eV for Cys-Bckb7.

The observed dipoles are consistent with the value of 1.03 eV measured for SAMs of L-cysteine on Au [147]. These mainly originate from the interaction of the Au electron wave functions with the organic overlayer, the creation of a chemical bond between the thiol moiety and the Au surface, and the presence of molecule intrinsic dipole potentials [169]. The first two cases (also called ‘bond dipole’ [169]) usually result in a localized

net charge transfer between the substrate and the overlayer, which in return creates an electrical dipole potential at the interface. The formed dipole then leads to a shift of the electronic states of the molecular overlayer down relative to the substrate states. In a simple approximation, one can add the bond dipole (BD) and the intrinsic molecular dipoles (ΔU),

$$eD = BD + \Delta U \tag{5}$$

where eD is the total interface dipole potential [169].

As an example, the electronic structure calculations yielded the ensemble-average molecular dipole mD of 19.4 ± 5.9 D for Cys-T7 and 19.1 ± 4.9 D for Cys-Bckb7, as projected on the PNA helical axis. The intrinsic molecular dipole ΔU can be calculated from the ensemble-average molecular dipole mD using

$$\Delta U = \frac{mD \cdot a}{\varepsilon_r \cdot \varepsilon_0} \tag{6}$$

Here a and ε_r are the surface coverage and the dielectric permittivity of the PNA film and ε_0 is the vacuum permittivity (cf. eq 3 in ref [169]). By employing a surface coverage of ~80 pmol/cm^2, which was measured for Cys-T7 by cyclic voltammetry in the past [59], and an estimate for ε_r of 2-4, an intrinsic molecular dipole ΔU of 0.9-1.8 eV can be calculated for either Cys-T7 or Cys-Bckb7. The measured values of 1.08 eV (Cys-T7) and 1.56 eV (Cys-Bckb7) are in good agreement with the calculated theoretical value. Based on these results it can be concluded that the interface dipole potential of the PNA film is mostly due to the backbone dipole.

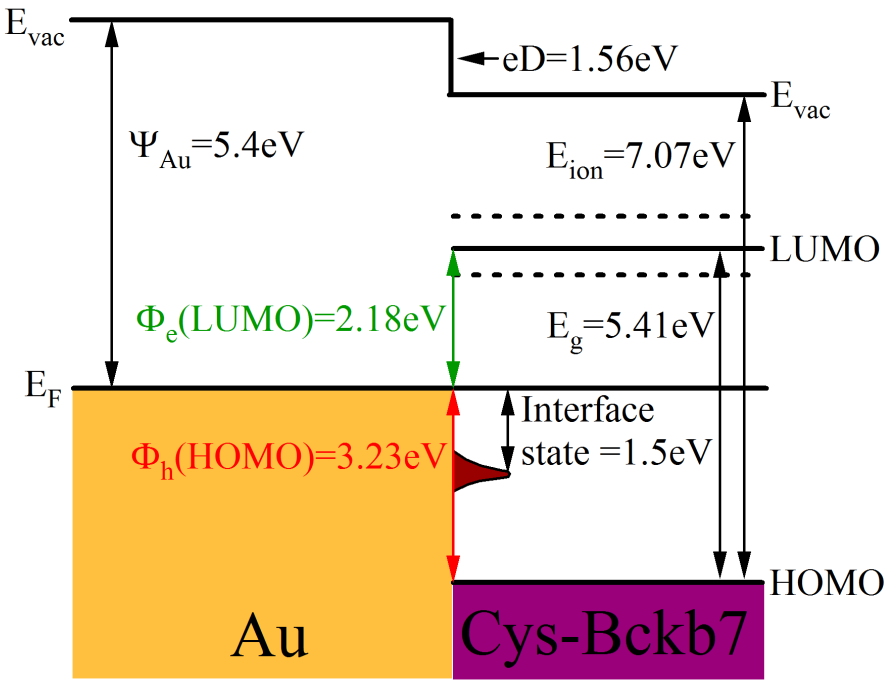

Figure 28: Band alignment at the Au/Cys-Bckb7 interface with dotted lines symbolizing the uncertainty of the estimated LUMO energy. (Reprinted (adapted) with permission from [143]. Copyright 2011 American Chemical Society)

However, the calculated value of ΔU can still vary by more than 50% as a result of the uncertainty of the employed parameters. While the surface coverage is affected by an error of ±10 pmol/cm^2, the dielectric permittivity could increase significantly in comparison to the assumed value of 2-4, depending on the amount of the residual solvent present in the PNA layer.

The dipole potential of 1.03 eV as measured on molecular layers of L-cysteine on gold [147] may also represent the bond dipole BD present at the Au/PNA interface, but it should most likely be smaller, as BD is roughly proportional to the surface coverage of the monolayer [169]. Due to the small size of cysteine molecules, a monolayer of L-cysteine should exhibit a much larger surface coverage than the investigated PNA

SAMs. If one assumes a realistic ratio between the surface coverages of about 10, the BD term should amount to only a few tenths of eV. This estimated value is noticeably smaller than either the intrinsic molecular dipole or the net interface dipole of the PNA film. The difference between the interface dipole potentials of the three SAMs could also be explained by a difference in surface coverage. If both terms contributing to eD are more or less proportional to the surface coverage, it can be assumed that the surface coverage of the Cys-Bckb7 SAM is 1.56/1.45 ≈ 1.08 times larger than that of the Cys-A7 SAM and 1.56/1.08 ≈ 1.44 times larger than that of the Cys-T7 SAM. The missing nucleobases most likely reduce the effective diameter of the PNA molecule by about a factor of 2 (cf. Figure 15), while the adenine and thymine bases contain different amounts of hydrogen bonding sites at their polar moieties [158], resulting in varying amounts of adsorbed solvent which could additionally impact the density of the formed SAMs.

In summary, the investigation of self-assembled monolayers of Cys-appended PNA 7-mers of adenine (Cys-A7), thymine (Cys-T7), and abasic PNA backbone (Cys-Bckb7) with UPS and XPS revealed the orbital line-up at the Au/PNA interfaces. The recorded density of the highest occupied electronic states closely matched the calculated density of states of the PNA SAMs, the calculations also showed that the PNA backbone must be accounted for in order to compute the PNA density of states correctly. The orbital line-up showed significant barriers for both hole and electron injection from Au to Cys-T7 and Cys-Bckb7, while Cys-A7 displayed a significantly lower electron injection barrier. All three SAMs exhibit large interface dipoles of 1.45 eV (Cys-A7), 1.08 eV (Cys-T7), and 1.56 eV (Cys-Bckb7). These results imply that charge transfer

between the PNA molecules and the Au substrate may be difficult due to the energy which would be necessary to overcome the injection barriers.

4.3: The Interfaces of Cys-A7-Fc and Cys-T7-Fc on Au

The charge transfer characteristics of PNA based SAMs are generally studied with cyclic voltammetry [59, 60, 146, 170, 171]. In these electrochemical characterization measurements, the ferrocene redox groups positioned at the end of the PNA strands are used for charge injection into the SAM. The charge transfer through a biomolecule is mostly dependent on the charge injection barriers at the interfaces between the various sections of the molecule. The characterization of cysteine appended PNA (see 4.2) represents a first approach in the depiction of the electronic structure of a PNA SAM and the identification of the charge injection barriers responsible for the charge transfer characteristics. The goal of the measurements presented here was to characterize the charge injection barriers between the ferrocene tail-group and the PNA molecule.

For this purpose, SAMs of cysteine appended and ferrocene terminated PNA containing adenine (Cys-A7-Fc) and thymine bases (Cys-T7-Fc) were used, as shown in Figure 16. The incubation protocol was similar to that followed for the Cys-PNA experiments, with an incubation time of 24 hours, a concentration of 20 µM, and an incubation temperature of approximately 37˚C.

The recorded high resolution XP-spectra for the C1s, N1s, and O1s energy ranges of both SAMs in comparison to the Cys-PNA SAMs without ferrocene tail-groups are shown in Figure 29. Neither the C1s nor the N1s emission features show significant differences between regular Cys-PNA and ferrocene terminated Cys-PNA. The C1s

emission features of Cys-A7-Fc and Cys-T7-Fc again contain emission lines that are attributed to single and double bonds of carbon (C-C, C=C), hydrogen and nitrogen in carbon bonds (C-H, C-N, C-N=C), and double bonds between carbon and oxygen (C=O), as discussed in detail in 4.2. The N1s emissions display the expected lines for NH_2, C-N, and the Cys-A7 and Cys-A7-Fc related emission features additionally display a shoulder at lower binding energy, which is attributed to iminic nitrogen present in the adenine bases.

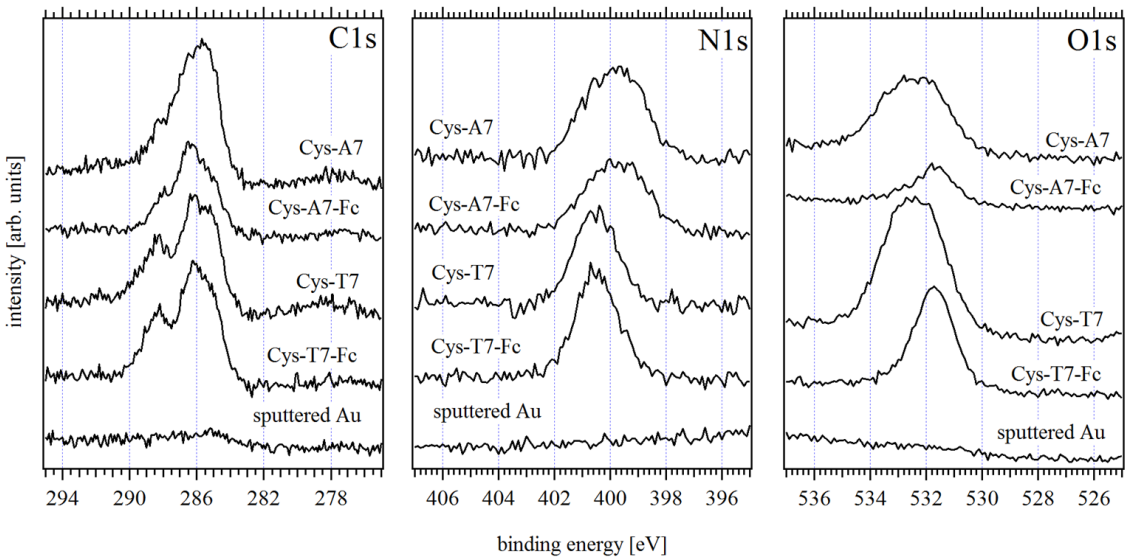

Figure 29: High resolution XP-spectra of the C1s, N1s, and O1s emission features of Cys-A7, Cys-A7-Fc, Cys-T7, and Cys-T7-Fc.

Conversely, there is a difference between ferrocene terminated and regular Cys-PNA in the O1s spectra, and while Cys-A7 and Cys-T7 contain an emission line at around 533 eV, which is attributed to coadsorbed water, this line is missing in the Cys-A7-Fc and Cys-T7-Fc spectra. This may be a consequence of the hydrophobic characteristics of ferrocene [172, 173], leading to lower water content in these SAMs.

From the S2p spectra shown in Figure 30 it can be concluded that the incubation in Cys-A7-Fc and Cys-T7-Fc resulted in SAMs with mostly vertical molecular

arrangement, as no S2p emission features can be detected. The absence of these features also indicates that no significant deposition of excess molecules occurred on top of the SAM surface.

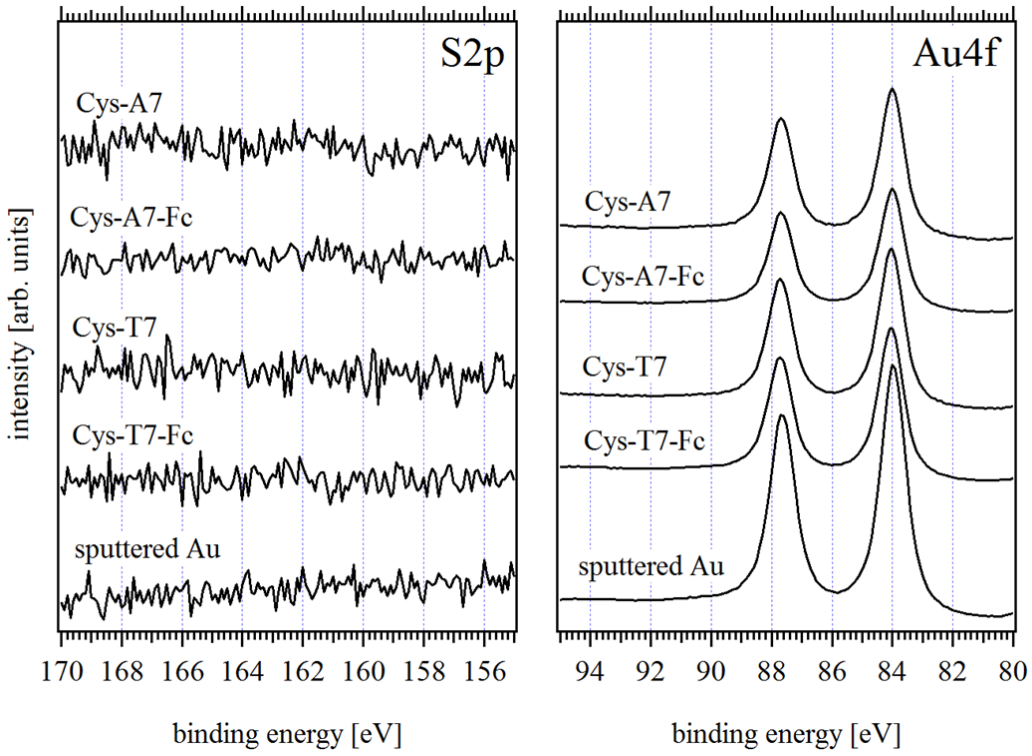

Figure 30: S2p and Au4f high resolution XP-spectra as measured on Cys-A7, Cys-A7-Fc, Cys-T7 and Cys-T7-Fc.

The thickness of the deposited SAMs was calculated from the Au4f intensity attenuation (shown in Figure 30). The intensity ratios before and after incubation are 0.49 for Cys-A7-Fc and 0.45 for Cys-T7-Fc. With a mean free path of 36 Å [156], thickness values of 25.9 Å and 28.8 Å resulted for Cys-A7-Fc and Cys-T7-Fc, respectively.

These values are in close agreement with the values obtained for Cys-A7 and Cys-T7 SAMs and are lower than what would be expected for a SAM containing PNA molecules with appended ferrocene, since the ferrocene tail-group increases the length of the molecule and should therefore increase the thickness of the formed monolayer.

However, the O1s spectra showed that the presence of residual water is strongly reduced in the Cys-A7-Fc and Cys-T7-Fc SAMs, which could allow the PNA molecules to arrange into a more helical conformation and therefore lower the thickness of the SAMs.

As a baseline experiment, a self-assembled monolayer was deposited from ferrocenyl undecanethiol (Figure 18) in order to compare ferrocene related core level and HOMO emission features. The normalized Fe2p emission features originating from the ferrocene tail-group of Cys-A7-Fc and Cys-T7-Fc are shown in Figure 31 in comparison to the emission features measured for the Fc-SAM.

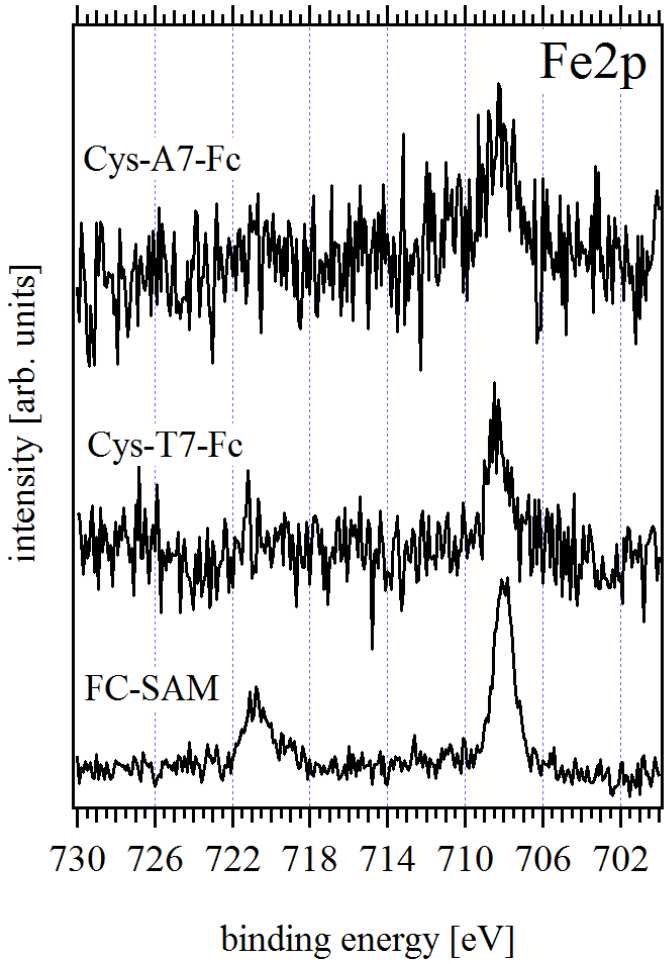

Figure 31: Normalized Fe2p emission features of Cys-A7-Fc and Cys-T7-Fc in comparison to a Fc-SAM.

It is evident that the spectrum obtained for the Fc-SAM exhibits a much better signal to noise ration than the spectra of Cys-A7-Fc and Cys-T7-Fc. This difference can be explained by the higher density of the Fc-SAM, which only contains a thiol group and an alkane chain. This allows for a denser molecular assembly than in the case of Cys-A7-Fc and Cys-T7-Fc, which contain nucleobases demanding a larger molecular footprint. A comparison of the peak areas of the original Fe2p emission peaks before normalization (not shown here) allows for a rough estimate of the density ratios between the SAMs. For this purpose, the background was removed from the Fe2p emission peaks and the area was calculated by integration over the peak shapes.

The resulting peak areas of the three Fe2p peaks led to ratios of 1:3 between the Fc-SAM and Cys-A7-Fc, and 1:2 between the Fc-SAM and Cys-T7-Fc. The ratios indicate that the Cys-T7-Fc SAM exhibits a slightly higher density than the Cys-A7-Fc SAM, which is also evident in the higher signal-to-noise ratio of the Cys-T7-Fc SAM and is in agreement with the larger molecular footprint of Cys-A7-Fc (compare Figure 16). Apart from the density-related difference in signal-to-noise ratios, all three spectra appear similar and the $Fe2p_{3/2}$ peak is located at approximately 708 eV for all three SAMs. This peak position corresponds to values published in literature [174, 175] and demonstrates the presence of ferrocene.

Figure 32 shows UP-spectra recorded for the ferrocene terminated Cys-PNA SAMs in comparison to the SAMs formed from regular Cys-PNA. The secondary edge was used in order to estimate the work functions of the formed SAMs and resulted in values of 4.31 eV (Cys-A7-Fc) and 4.3 eV (Cys-T7-Fc). While the work function of Cys-A7-Fc differs significantly from the work function of Cys-A7 (3.95 eV), the values

of Cys-T7-Fc and Cys-T7 (4.32 eV) are in close agreement. The absence of residual solvent is a reasonable cause for the work function increase. Coadsorbed water molecules could introduce a dipole moment [176] that might counteract the molecular dipole moment of the PNA molecules and the absence of these dipoles should increase the work functions noticeably.

The work functions of the clean Au substrates before the incubation resulted in two different values as two different samples were used, and the dipoles eD calculated from the difference between the corresponding work functions were determined to be 1.11 eV (Cys-A7-Fc) and 0.94 eV (Cys-T7-Fc). These values are similar to the interface dipole of 1.03 eV observed for the Au/Fc-SAM interface (spectrum not shown here).

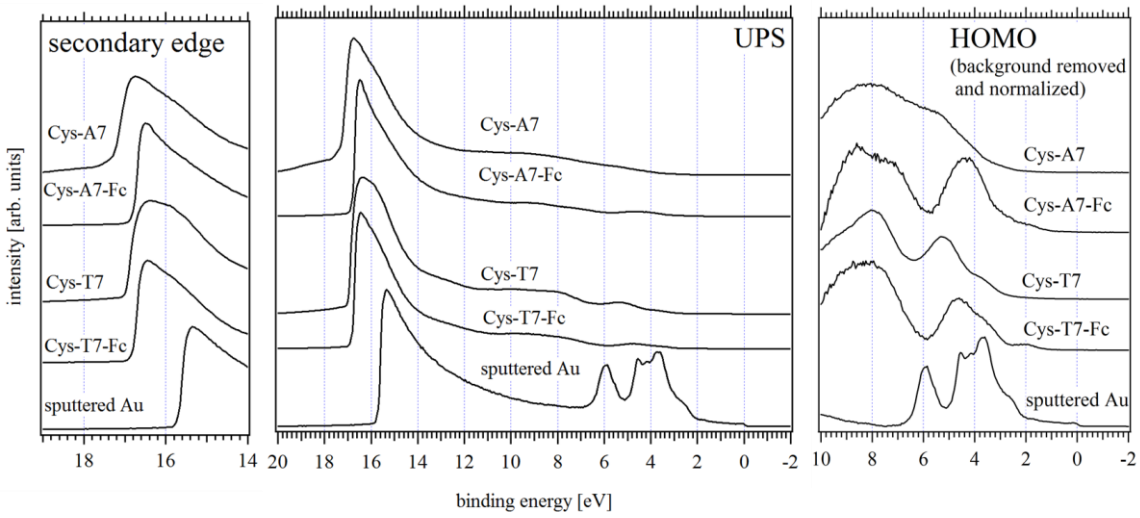

Figure 32: UPS derived spectra of Cys-A7, Cys-A7-Fc, Cys-T7, and Cys-T7-Fc are shown in the center. The recorded secondary edge is shown on the left while the background removed HOMO region is displayed on the right.

Figure 33 shows the background removed and normalized HOMO regions of Cys-A7, Cys-A7-Fc, Cys-T7, and Cys-T7-Fc in comparison with the Fc-SAM. The Fc-terminated SAM shows an additional emission between 1 and 2 eV, which is related to the HOMO emission of ferrocene [177-179]. The shift of the PNA backbone related

emission peak from 5.5 eV (Cys-A7 and Cys-T7) to lower binding energies (Cys-A7-Fc and Cys-T7-Fc) indicates a possible molecular orbital reconfiguration due to the interactions between ferrocene and the PNA molecule.

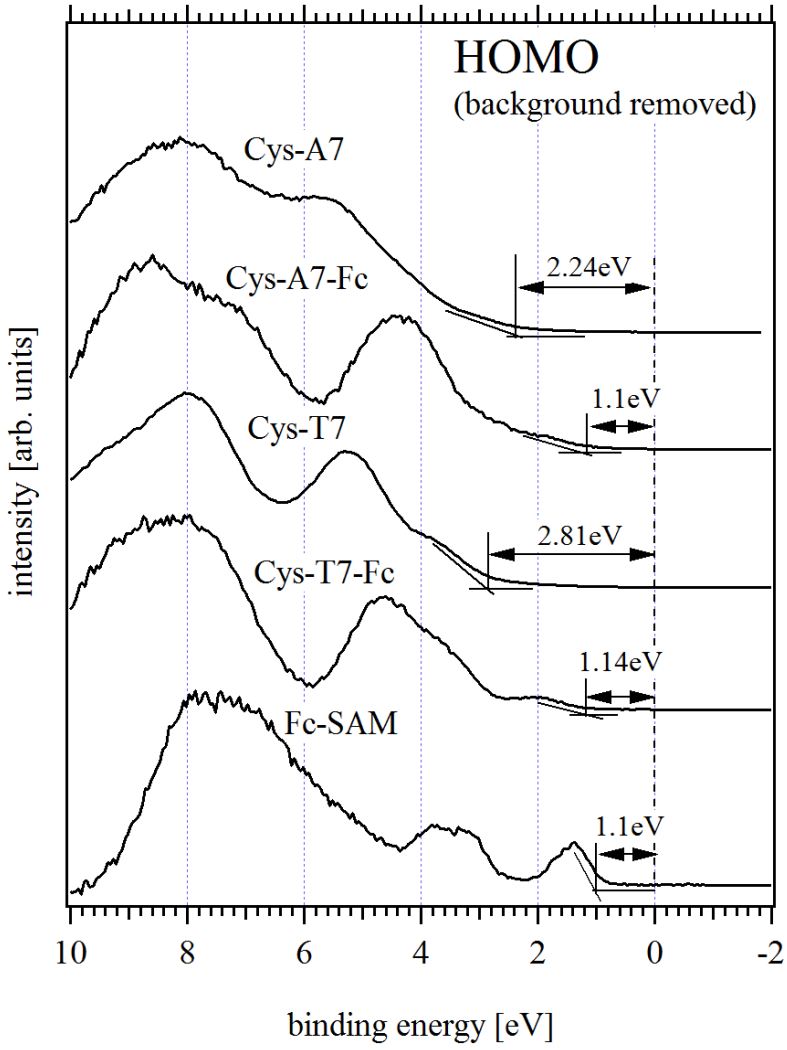

Figure 33: Background removed HOMO emission features as measured on Cys-A7, Cys-A7-Fc, Cys-T7, and Cys-T7-Fc in comparison to HOMO features of a Fc-SAM.

The emission features of Cys-A7-Fc and Cys-T7-Fc at higher binding energies are, in comparison to the features obtained for Cys-A7 and Cys-T7, more pronounced and not as broad while still exhibiting approximately the same binding energies. This

occurrence is likely a result of the absence of residual water, which would lead to sharper peaks and features, as was mentioned in 4.2.

By inserting lines at the low binding energy onset of the HOMO features, the hole injection barriers Φ_h were determined, resulting in values of 1.1 eV (Cys-A7-Fc), 1.14 eV (Cys-T7-Fc), and 1.1 eV (Fc-SAM). The hole injection barriers for Cys-A7 and Cys-T7 were already estimated in section 4.2 which led to values of 2.24 eV and 2.81 eV, respectively. The close resemblance of the onsets of Cys-A7-Fc, Cys-T7-Fc, and the Fc-SAM demonstrate that the ferrocene tail-group defines the hole injection barriers of the PNA SAMs.

With the calculated work functions and hole injection barriers, the band line-up of the Cys-A7-Fc and Cys-T7-Fc SAMs can be drawn and the results are shown in Figure 34 and Figure 35. Since the measured dipoles and hole injection barriers are in close resemblance to values obtained for the Fc-SAM, a LUMO energy of 2.2 eV, as mentioned in literature for ferrocene [177], was used here. This value was chosen as it is assumed that the ferrocene terminus is mostly responsible for the hole and electron injection barriers and not the self-assembled PNA molecules. The LUMO energy of 2.2 eV leads to transfer gap values of 3.3 eV and 3.34 eV for Cys-A7-Fc and Cys-T7-Fc, respectively. The ionization energies of the investigated SAMs were determined to be 5.41 eV (Cys-A7-Fc) and 5.44 eV (Cys-T7-Fc), which is in good agreement with the literature value of 5.4 eV obtained for the ionization energy of ferrocene [177] and with what was measured for the Fc-SAM (5.38 eV).

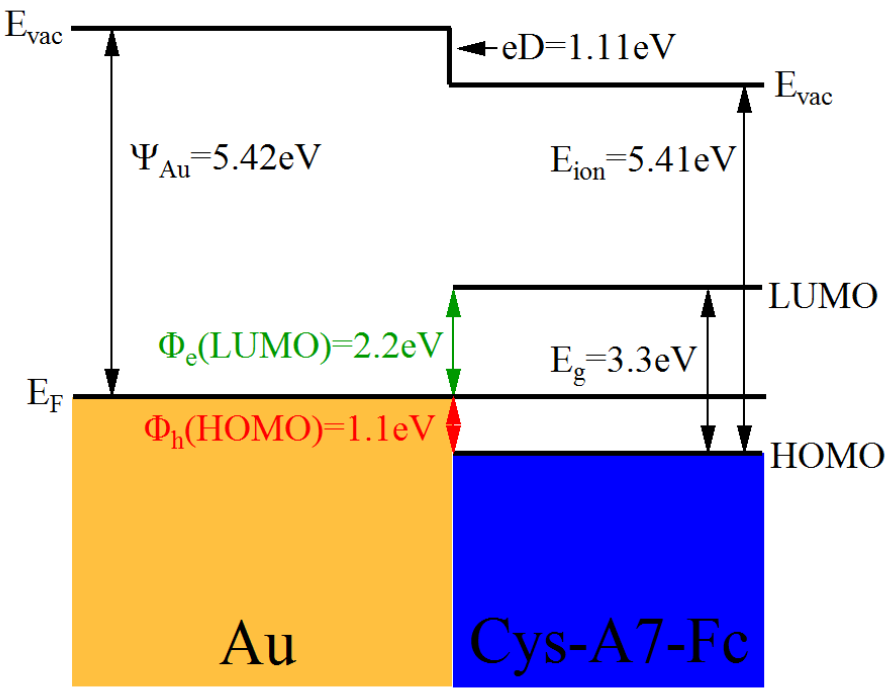

Figure 34: Band line-up of the Au/Cys-A7-Fc interface displaying a much lower hole injection barrier than measured on Cys-A7.

The band alignments displayed in Figure 34 and Figure 35 symbolize the electronic structure of the Cys-A7-Fc and Cys-T7-Fc SAM surfaces rather than the actual Au/SAM interface. To depict the actual band alignment of the complete PNA molecule, the injection barrier located at the PNA/Fc interface must be compared with the injection barriers measured for the Cys-PNA SAMs in 4.2. The charge injection barrier between the ferrocene and the PNA strand is of particular interest as it is a limiting factor for charge transfer through the molecule.

Since the UP-spectra are a superposition of ferrocene and PNA related HOMO emission features, it is reasonable to assume that by subtracting the Fc-SAM related emission features from the PNA spectra, the actual HOMO onset at the PNA/Fc interface can be obtained.

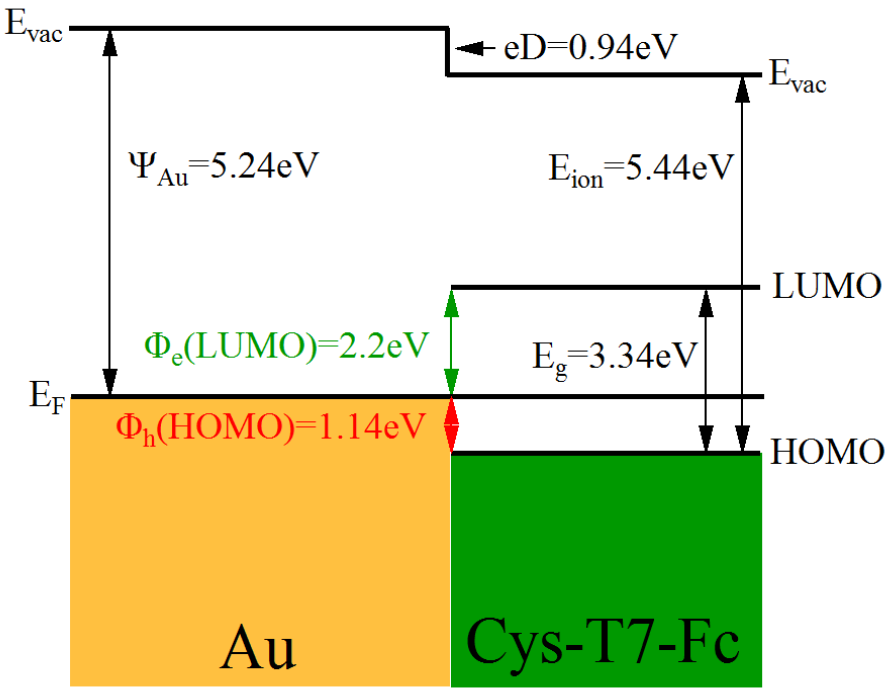

Figure 35: The band alignment at the Au/Cys-T7-Fc interface. The interface dipole and ionization energy are in close agreement with values obtained for Cys-A7-Fc.

The Fe2p emission lines shown in Figure 31 did not show significant shifts between the PNA and Fc SAMs, demonstrating that the ferrocene related emissions in the Cys-PNA-Fc UP-spectra are most likely free of shifts and the Fc-SAM emissions can be directly subtracted from these spectra. The Fc-SAM spectrum was scaled down for the subtraction process as the higher density of the Fc-SAM resulted in more intense emission features. The scaling factors used for this procedure were 3.2:1 (Cys-A7-Fc) and 2.2:1 (Cys-T7-Fc) and are in close agreement with the density ratios estimated from the Fe2p peak areas, strengthening the validity of these ratios. The resulting difference spectra are shown in Figure 36.

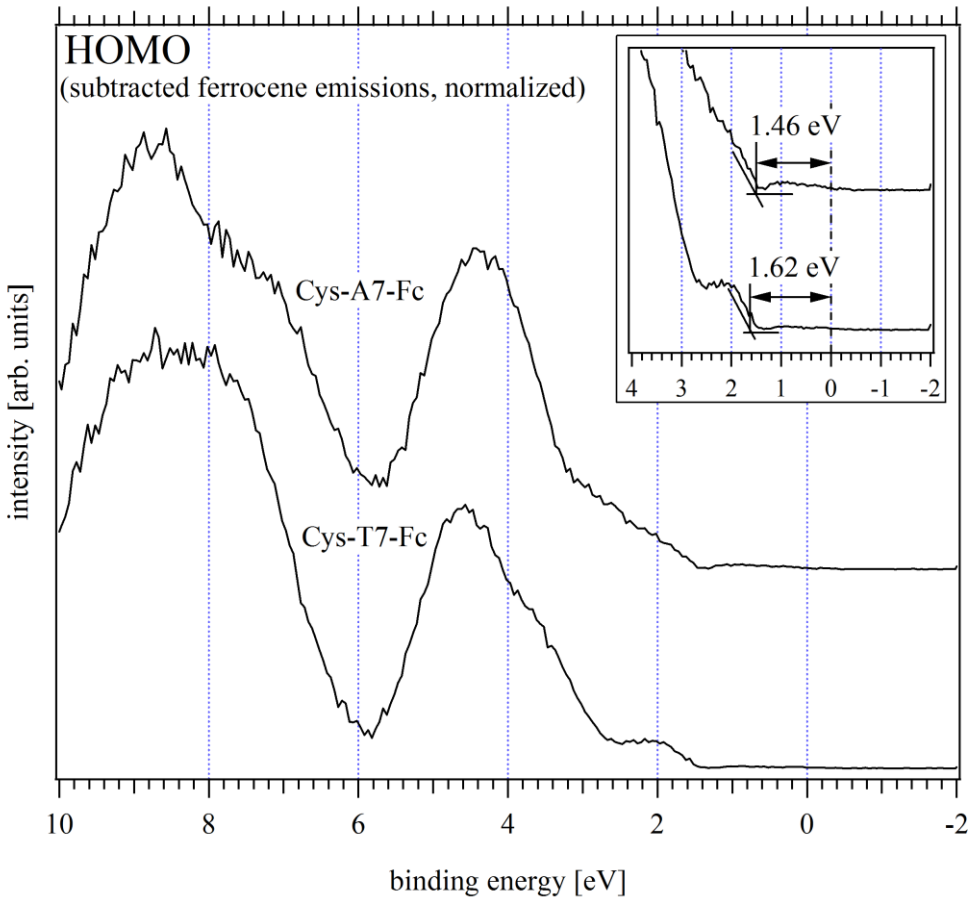

Figure 36: HOMO emission features of Cys-A7-Fc and Cys-T7-Fc with subtracted ferrocene related emission features. The insert shows the low energy onsets of both SAMs.

The HOMO onset of the Cys-A7/Fc interface is with 1.46 eV much lower than the hole injection barrier of 2.24 eV, as measured for the Cys-A7 SAM. A similar observation can be made for the Cys-T7/Fc interface, where the onset is with 1.62 eV much lower than for a Cys-T7 SAM (2.81 eV). The shifts of the onsets to lower binding energies indicate that a molecular orbital reconfiguration might have occurred. Comparing these values with the hole injection barriers of the ferrocene termini shows that barriers of 0.36 eV and 0.48 eV are most likely present at the Cys-A7/Fc and Cys-T7/Fc interfaces.

An evaluation of the different values allows for an assessment of charge injection barriers throughout the PNA SAMs and the results are displayed in Figure 37 and Figure 38.

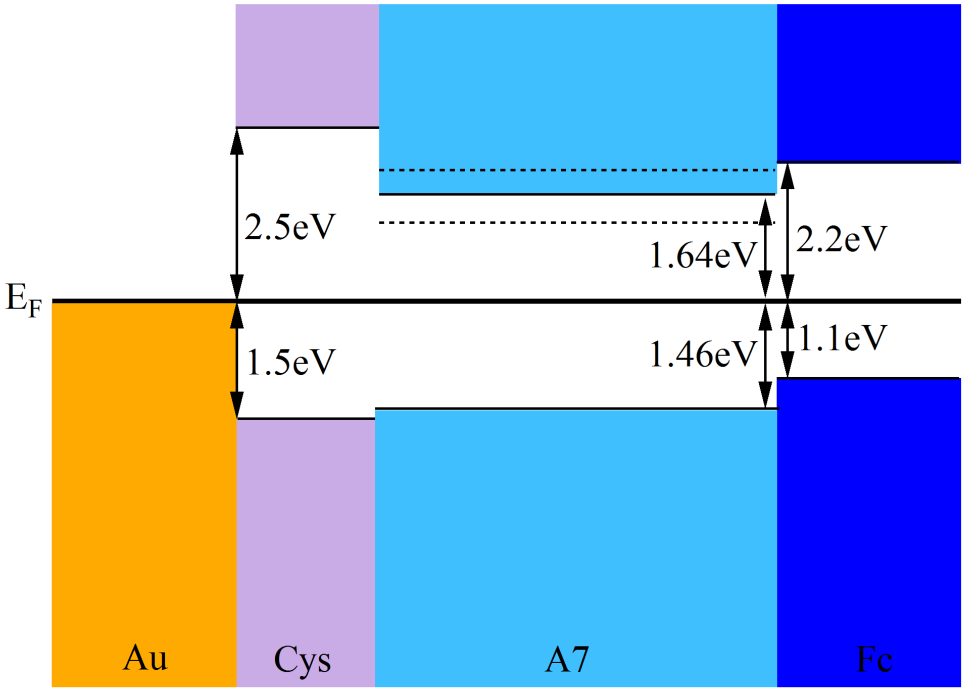

Figure 37: Hole and electron injection barriers throughout the Cys-A7-Fc SAM as measured by PES and estimated from theoretical values.

Both diagrams show the bonding orbital of cysteine, which is located at the actual interface and was characterized by PES in the past [147]. The cysteine can be treated as a stepping stone for hole injection into the PNA molecule while its high LUMO of 2.5 eV [180] represents a barrier for electron injection at the Au/PNA interface. The hole injection barriers measured for the two types of PNA strands without a ferrocene terminus (Cys-A7 and Cys-T7) are higher than the barriers depicted from the difference spectra shown in Figure 36. It is likely that a molecular orbital reconfiguration took place, shifting the HOMO level towards lower energies. This shift is also reflected in the

LUMO level, as a molecular orbital reconfiguration should have an influence on the electron injection barriers as well.

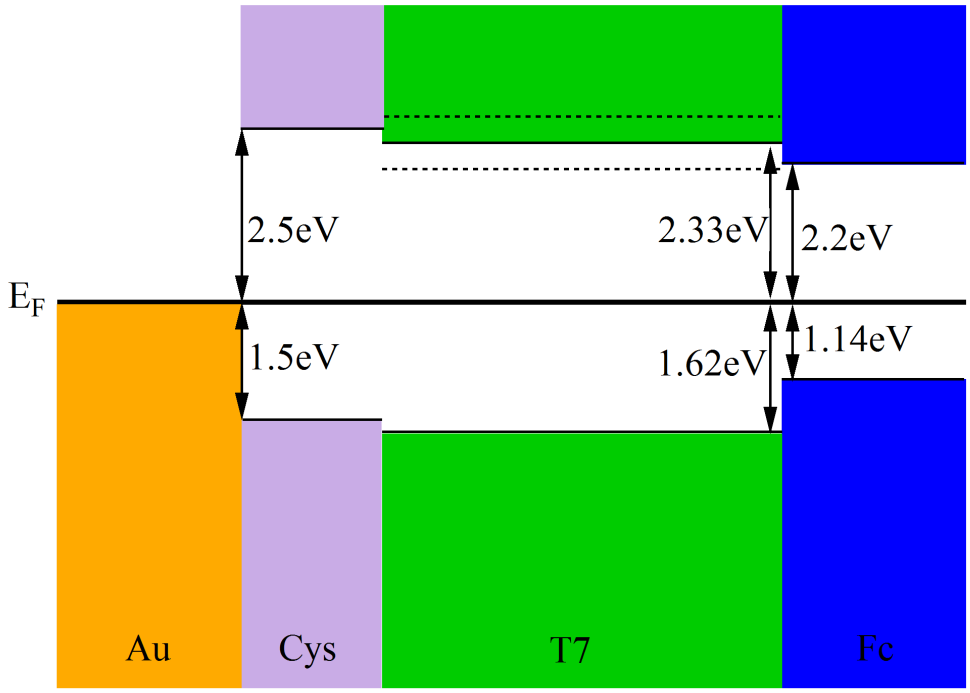

Figure 38: The charge injection barriers of the Cys-T7-Fc SAM as measured by PES and estimated from theoretical values.

The barriers at the PNA/Fc interface are important for the characterization of charge transfer rates in electrochemical measurements. In these measurements, electrons are injected into the PNA SAM from the ferrocene redox group and an existing barrier at this interface can hinder the charge flow. Cyclic voltammogram measurements on single stranded PNA of adenine and thymine showed that adenine appended PNA exhibits better charge transfer characteristics than thymine appended strands [146]. This is in agreement with the UPS measurements, as the Cys-A7-Fc SAM revealed a step down from the ferrocene HOMO by 0.36 eV, while a step of 0.48 eV is present at the Cys-T7/Fc interface.

Both of the SAMs investigated in this study exhibited larger hole injection barriers than cysteine or ferrocene. It can therefore be concluded that the PNA and especially the type of appended nucleobase should define the hole transfer characteristics of a self-assembled PNA monolayer. This conclusion corresponds with results from cyclic voltammetry measurements which showed that charge transfer through a PNA molecule strongly depends on the type of nucleobase appended to the strand [59, 146]. However, since the estimated positions of the electron injection barriers are based on theoretical calculations and values obtained from literature, it is difficult to assess the exact impact of the cysteine head-group, PNA backbone, nucleobases and ferrocene tail-group on the electron transfer through the SAM without having experimental data regarding the exact LUMO positions of the investigated PNA SAMs.

4.4: Charge Injection Barrier Changes as an Effect of PNA Strand Orientation

Preliminary PES measurements performed on SAMs formed from Cys-T7 solutions with lower concentrations and shorter incubation times showed a shift of the hole injection barrier to lower energies, when compared with SAMs formed with Cys-T7 at a concentration of 20 µM and an incubation time of 24 hours. Since low concentrations and short incubation times result in SAMs with mostly flat-lying molecules and pinholes in the film as described in 3.1, a shift of the hole injection barrier would imply that the orientation of the PNA molecules on the surface and their increased interaction with the Au substrate can have a significant impact on the electronic structure of the formed SAM.

The following experiment was therefore designed as a simple approach to test the hypothesis that flat lying molecules would result in lower hole injection barriers due to increased PNA-Au interactions. In contrast to the Cys-T7 and Cys-Bckb7 experiments,

the PNA molecules (PNA-T7 and PNA-Bckb7) used here were missing the cysteine head-group, as shown in Figure 17. The motivation for this approach was the prevention of self-assembly and the promotion of adsorption of the PNA molecules. Except for the missing cysteine head-group, the molecules were identical and the incubation procedure was unchanged with an identical incubation time, concentration and rinsing procedure as with the Cys-PNA experiments.

The resulting XP-spectra for the PNA molecules are shown in comparison to the Cys-PNA molecules in Figure 39. While the Cys-T7 and PNA-T7 spectra are in close agreement with each other, the PNA-Bckb7 spectra differ significantly from Cys-Bckb7. As discussed earlier in subsection 4.2, the C1s spectrum of Cys-Bckb7 consists of three emission lines that can be attributed to the various carbon species present in the PNA molecule. The spectrum of PNA-Bckb7, however, only exhibits one asymmetric peak at around 285.1 eV which can be attributed to hydrocarbons. Furthermore, the N1s spectrum of PNA-Bckb7 only displays a faint peak at approximately the same position at which the emission feature of Cys-Bckb7 is located. The O1s spectrum of PNA-Bckb7 also exhibits a rather large emission peak at higher binding energies in comparison to the Cys-Bckb7 spectrum, which is likely attributed to residual water on the surface. The emission lines of hydrocarbons and water suggest that residual contaminants from the rinsing step are present on the surface and that most of the PNA-Bckb7 molecules washed off during the rinsing step.

As mentioned above, the Cys-T7 and PNA-T7 spectra are in a much better agreement and the C1s spectra for both experiments display emission features in which the three main emission lines are still distinguishable. The O1s emission feature for

PNA-T7 exhibits a similar full width at half maximum (FWHM) and energy range as the Cys-T7 related feature, while the N1s feature is the only one that shows a slight discrepancy between both experiments. This can be observed by a small shoulder at lower binding energies for the PNA-T7 film. In order to investigate the origin of the mentioned shoulder, the N1s emission feature of PNA-T7 was fitted with Gaussian-Lorentzian peaks and the result is shown in Figure 40.

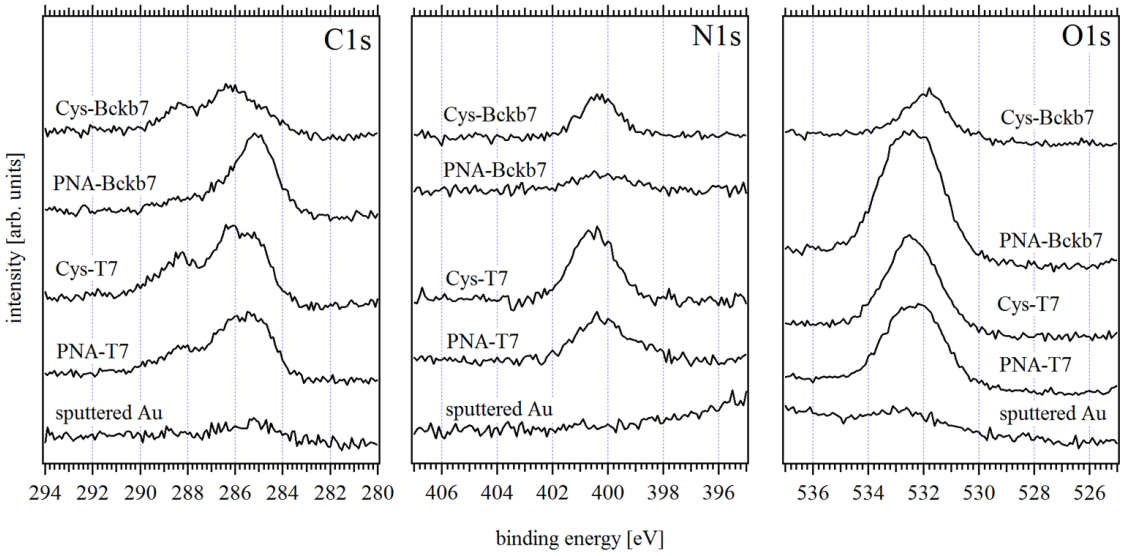

Figure 39: High resolution XP-spectra of the C1s, N1s, and O1s energy range of Cys-Bckb7 and Cys-T7 in comparison to PNA-Bckb7 and PNA-T7.

The N1s emission feature evidently contains three emission lines, two of which were already discussed in 4.2 and are attributed to nitrogen in C-N bonds, located at 400.8 eV, and nitrogen in the amino and amide groups of PNA [107, 148], which can be found at 400.1 eV. The third emission line was not observed for the Cys-T7 emission feature and is located at 398.7 eV. This energy is similar to values published for adsorbed thymine on single crystalline Cu [181] and is related to unsaturated nitrogen induced by the dissociation of a hydrogen atom, which plays an important role in the adsorption of thymine bases on metal surfaces.

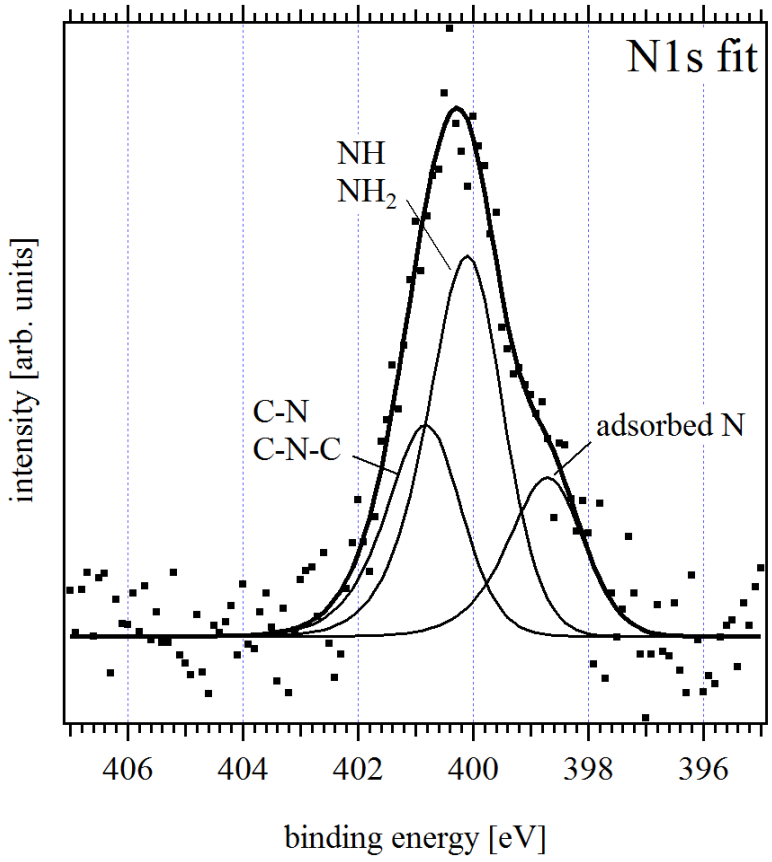

Figure 40: Gaussian-Lorentzian peak fits for the N1s emission feature of PNA-T7

Based on the presence of this peak in the spectrum it can be assumed that the PNA-T7 molecules adsorbed on the clean Au substrate through the interaction of nitrogen atoms in the thymine bases with the metal surface. This is supported by the poor adsorption of PNA-Bckb7, which does not contain these nitrogen sites. The fact that PNA-T7 adsorbs on Au through its nitrogen sites located on the thymine bases leads to the hypothesis that the deposited film contains PNA molecules that are either oriented at a flat angle towards the substrate or lie flat on the surface.

From the attenuation of the Au4f emission features recorded for all four incubation experiments (shown in Figure 41), an estimate for the thickness of the various layers can be made. The thickness estimation can help determine the orientation of the

adsorbed PNA molecules if it is compared to the previous Cys-PNA experiments. By following the procedure explained in 3.3.3 and assuming a mean free path of 36 Å [156], thickness values of 20 Å and 32 Å were obtained for PNA-T7 and PNA-Bckb7, respectively. These values are lower than the thickness values calculated for Cys-T7 (29 Å) and Cys-Bckb7 (38 Å).

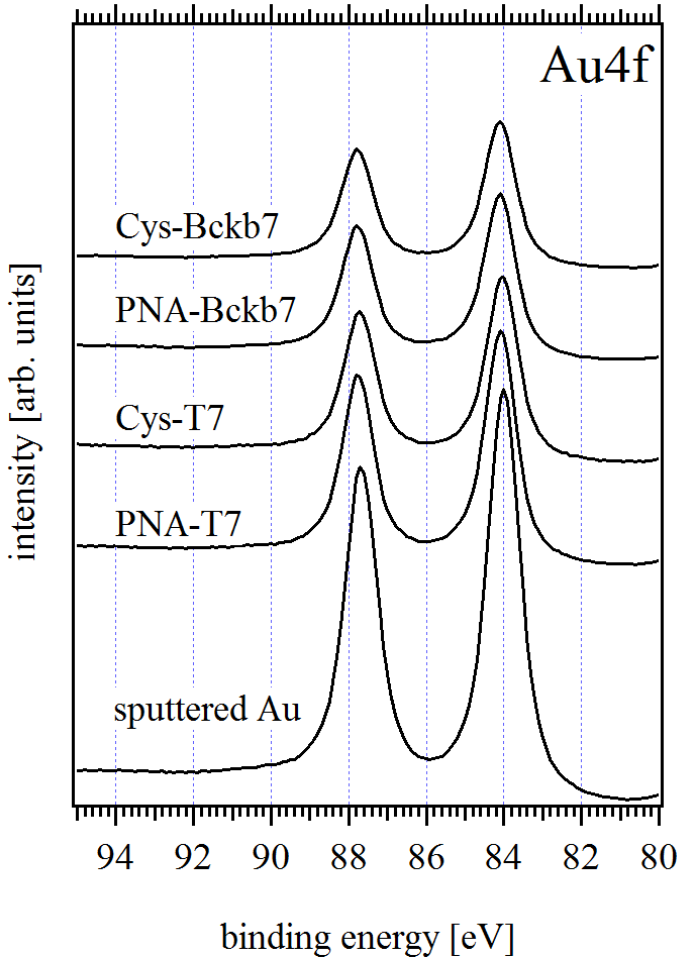

Figure 41: Au4f emission features of Cys-Bckb7, PNA-Bckb7, Cys-T7, PNA-T7, and the sputter cleaned Au surface.

The lower thickness of the PNA-T7 film in comparison to the Cys-T7 SAM supports the hypothesis that the absorbed molecules are oriented at a low angle towards the Au sample. This orientation may encourage charge transfer through the adsorbed

nitrogen atoms instead of the thiol moieties, as is the case for self-assembled Cys-T7 monolayers. As a result, this should lead to a reconfiguration of the orbital alignment at the interface.

Figure 42 shows the UPS data for the Cys-T7 and PNA-T7 interfaces. The work function of the deposited PNA-T7 film was calculated from the position of the secondary edge onsets and resulted in a value of 4.38 eV. This work function is in very close agreement with the work function of Cys-T7 (4.32 eV).

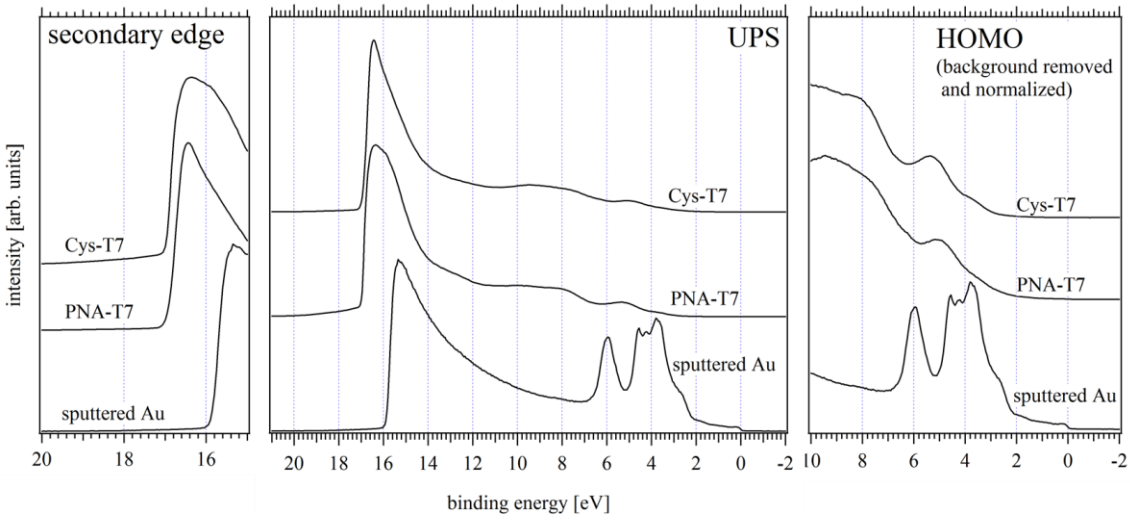

Figure 42: UP-spectra of Cys-T7, PNA-T7, and the sputtered Au surface are shown in the middle. The secondary edge onset is shown on the left, while the normalized and background removed HOMO region is shown on the right.

Figure 43 shows the HOMO region of Cys-T7 and PNA-T7 and the hole injection barriers present at these interfaces. The Cys-T7 SAM has a hole injection barrier of 2.81 eV, while PNA-T7 has a much lower hole injection barrier of 2.27 eV. This results in a HOMO onset difference of 0.54 eV between both layers. The tendency towards a lower hole injection barrier supports the assumption that cysteine appended PNA molecules in low density or incomplete layers interact with the Au substrate not only

through their thiol moieties, but can also exhibit charge transfer through nitrogen sites present in the bases, which adsorb on the sample surface.

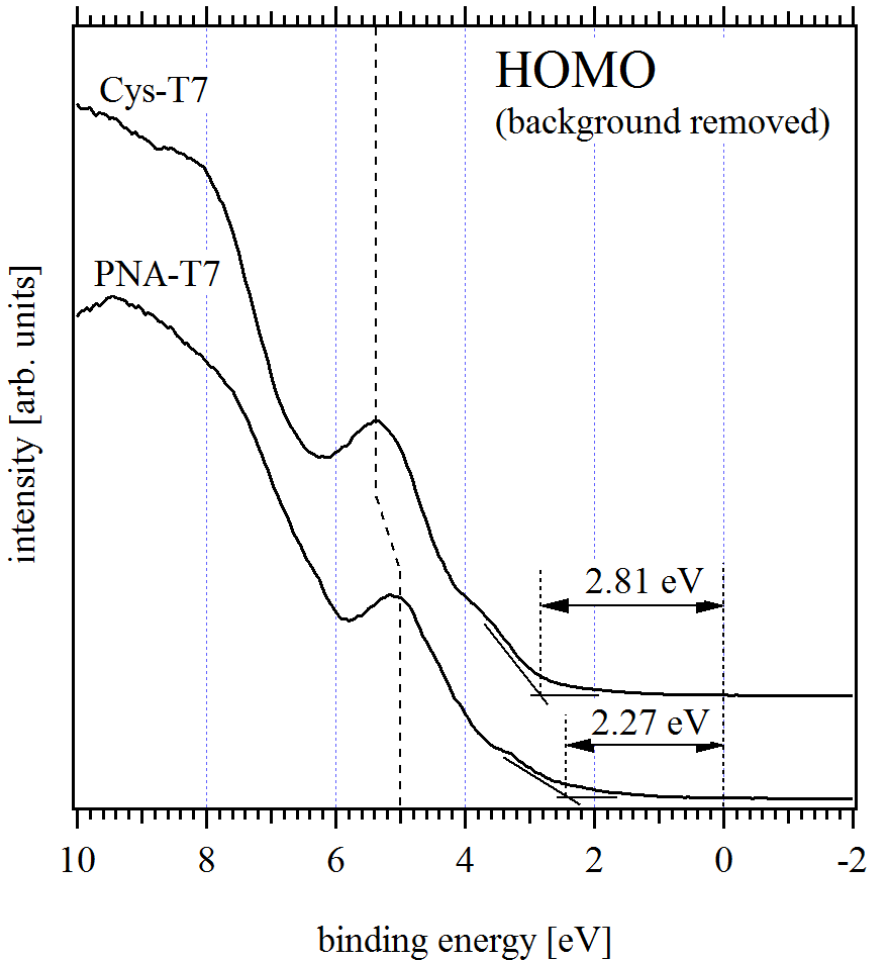

Figure 43: Background removed HOMO emission features of Cys-T7 and PNA-T7. A shift of the hole injection barrier by 0.54 eV is evident and a similar shift can be observed for the emission peak at around 5 eV.

The reconfiguration of the molecular orbitals at the interface is also demonstrated through a shift of the second HOMO peak from around 5.4 eV (Cys-T7) to approximately 5 eV (PNA-T7). As a shift was only detected for the HOMO peak and the hole injection barrier, but for none of the core level emission lines, it can be assumed that this shift is indeed a result of molecular orbital reconfiguration and not final state screening effects,

which are common in thin layers and usually result in a shift of all emission features to lower binding energies.

Finally, with the obtained work functions and hole injection barrier, the band line-up of the Au/PNA-T7 interface can be determined and is shown in Figure 44.

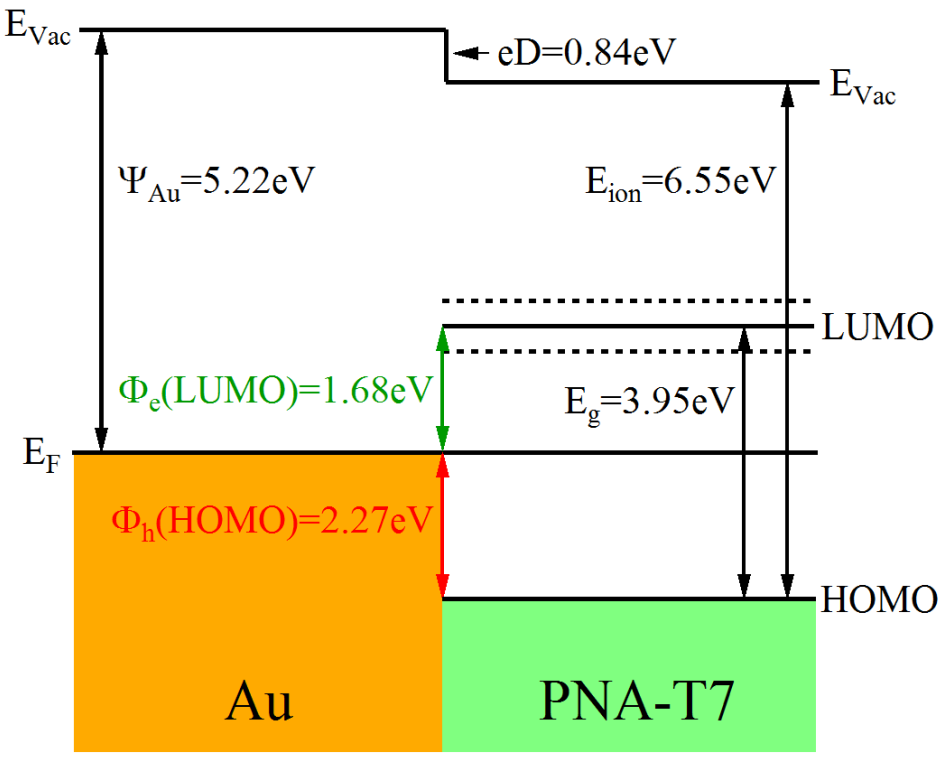

Figure 44: Band line-up of the Au/PNA-T7 interface. The dotted lines represent the uncertainty of the LUMO level position.

The observed interfacial dipole at this interface was calculated from the difference between the work functions before and after incubation. It resulted in a value of 0.84 eV, which is lower than what was measured for the Au/Cys-T7 interface (1.08 eV). The difference in dipoles may be a result of a lower density of the PNA-T7 layer in comparison to the Cys-T7 SAM, which evidently offer less intrinsic molecular dipoles present in the layer and therefore lower the overall dipole of the film. The orientation of

the PNA molecules in the layer could also have an impact on the interfacial dipole, since the DOS calculations for Cys-T7 showed that the backbone is the main origin of the intrinsic dipole. The backbone dipole is oriented along the molecule and this dipole is only significant for the orbital line-up if it is oriented perpendicular to the surface. Hence, if the molecules lie flat, the dipole at the interface is reduced. Taking the calculated thickness value for the PNA-T7 film and the presence of adsorbed nitrogen into consideration, it can be assumed that the latter is the case, as a less dense film would also result in a UP-spectrum that would exhibit Au4f valance band emissions which were not observed here.

The position of the electron injection barrier Φ_e was calculated in a similar way as for the Cys-T7 SAM (see 4.2) by subtracting the value for the hole injection barrier Φ_h from the transfer gap E_g. The transfer gap was estimated from the DOS calculation of Cys-T7, and taking the corresponding uncertainties into account, led to error margins of ±0.28 eV. This resulted in a value of 1.68 eV for Φ_e, which is higher than for the Au/Cys-T7 interface. The higher value is a result of the shift of Φ_h towards lower energies due to the charge transfer through the nitrogen in the thymine bases.

The PNA-T7 experiment successfully demonstrated that the orientation of the PNA molecules in the film can be crucial for the injection barriers at the interface. The adsorption of the PNA molecules through the nitrogen sites of the attached thymine bases led to a decrease of the hole injection barrier by 0.54 eV in comparison to self-assembled Cys-T7. It was shown that this decrease is not a result of a final state screening effect, but proof of a reconfiguration of the molecular orbitals due to increased PNA-Au interactions.

The dependence of the electronic structure on the orientation of the strands is of great importance for the field of molecular devices where charge injection barriers play a vital role. Incomplete films of self-assembled PNA, which would be used in such devices, would lead to the wrong assessment of the band alignment at the interface. The resulting base-surface interactions would offer more sites for charge transfer between the surface and the molecule, and also be in competition with base-base interactions [182]. This would mean that hydrogen bonding between PNA strands would be partly obstructed in less denser films, which could play an important role in the field of biochip technology and organic devices. And while the exact degree to which various molecule orientations and film densities affect the electronic structure of the deposited organic layer is unclear, it seems reasonable that only dense films will result in reproducible values for the charge injection barriers.

CHAPTER 5: ELECTRONIC STRUCTURE OF SELF-ASSEMBLED TETRAPHENYLPROPHYRIN MONOLAYERS AND ARRAYS

Self-assembled organic molecules generally form well-ordered structures of partial high complexity and functionality. Such arrays of molecules could be used as molecular wires for applications in molecular electronics if interaction between neighboring molecules is achieved. Tetraphenylporphyrin (TPP) represents a potential building block for self-assembled monolayers of long-range conductive arrays since it allows for easy incorporation of functional groups for coordination purposes. The characterization of the electronic structure of thiolated TPP (TPP-S) is covered in the first part of this chapter, since TPP-S offers means of self-assembled porphyrin structures on gold surfaces. In the second part of the chapter, a TPP derivative containing nitrogen groups attached at its peripheral sites (TPP-CN) was studied, by forming structures of TPP-CN on gold substrates through the exposure of the sample to silver nitrate ($AgNO_3$). The addition of $AgNO_3$ allowed for an arrangement of the TPP-CN molecules into defined structures through ionic coordination driven by bond formation between Ag ions and the nitrogen groups of the TPP-CN molecules. The structures were further compared to adsorbed TPP-CN, a metalloporphyrin containing cobalt (CoTPP), and free base TPP in order to highlight the differences in core level binding energies.

5.1: Experimental

The Au substrates used for the described experiments were cleaned with organic solvents (see 3.4.1) before inserting them into the vacuum chamber and were subsequently sputter cleaned to remove any residual contaminants. Next, they were transferred into the analysis chamber and characterized with XPS, LIXPS and UPS. The substrates were then moved into the glove box, which is attached to the vacuum chamber and was described earlier in section 3.4, and incubated in various TPP solutions.

In the first set of experiments the substrates were submerged in a 1mg/1ml solution of TPP-S in dichloromethane (DCM) for 10 minutes at room temperature, as molecules containing thiol moieties are expected to readily form a monolayer on clean substrate surfaces [18]. The TPP-S was provided by Dr. Shengqian Ma's lab at the University of South Florida and exhibited a characteristic dark purple color typical for porphyrin solutions. Contamination of the surface was kept to a minimum during the incubation process due to the nitrogen atmosphere in the glove box.

Next, the sample was removed from the solution, rinsed with DCM to remove excessive, unbound molecules from the surface, and dried in the nitrogen flow of the glove box. The sample was then transferred back into the analyzer chamber analyzed by XPS, LIXPS and UPS.

The TPP-CN related experiments in the second set of measurements followed a similar procedure, in which 1mg/ml solutions of TPP-CN, CoTPP and TPP were used for the incubation process. The TPP-CN was also provided by Dr. Shengqian Ma, while the CoTPP and TPP was obtained from Dr. Peter Zhang (Chemistry Department, University of South Florida).

The Au and Ag substrates used for these experiments were cleaned and prepared in the same manner as previously described in section 3.4.1. The substrates were incubated in the TPP-CN, CoTPP and TPP solutions for 10 minutes, but since it was observed that rinsing of these samples lead to a removal of a majority of the adsorbed molecules, due to the much weaker affinity of Au for nitrogen groups, no rinsing step after incubation was performed. The samples were characterized with the same sequence of XPS, LIXPS and UPS before and after incubation.

The above mentioned experimental procedure represents the protocol for the deposition of weakly adsorbed TPP molecules on Au and Ag surfaces. In order to achieve a structured assembly of TPP-CN molecules on an Au surface, an additional step was inserted prior to incubation, were $AgNO_3$ was deposited on the clean substrate surface by *in situ* electrospray. For this purpose, the clean Au sample was transferred into the electrospray chamber after the initial PES characterization. A 1mg/ml solution of $AgNO_3$ in DCM was prepared and filled into a Hamilton 1ml syringe which was placed approximately 1 cm away from the orifice of the electrospray chamber column. A voltage of 3kV was applied to the syringe needle and the $AgNO_3$ solution was sprayed at a rate of 2ml/h. The solution was sprayed for 15 minutes resulting in a deposition of 0.5 ml of $AgNO_3$ solution. The pressure inside the electrospray chamber was approximately 10^{-5} mbar during the electrospray deposition. After the deposition was completed, the sample was transferred back into the analyzer chamber for XPS, LIXPS and UPS characterization. It was subsequently transferred into the glove box for the following sample incubation in a 1mg/ml TPP-CN solution.

A third, separate experiment was conducted to characterize the arrangement of TPP-CN into crystals upon $AgNO_3$ exposure. Due to the insulating characteristic of the SiO_2 surface used in this experiment and the resulting charging of the sample, electrospray deposition proved unsuccessful. Hence, drop deposition of the $AgNO_3$ solution inside the glove box was employed. After deposition of $AgNO_3$ on the substrate surface, the sample was characterized by XPS, LIXPS and UPS and moved back into the glove box. Si does not display an affinity for nitrogen and an adsorption of TPP-CN molecules on the surface was not observed after sample incubation, as they were immediately washed off the surface by solvent residues after removal from the incubation vial. Therefore, the molecules were deposited on the surface through drop deposition and letting the drops dry in the nitrogen atmosphere of the glove box. The sample was moved back into the analysis chamber after the deposition of TPP-CN molecules for a final PES characterization. All samples were further investigated by scanning electron microscopy (SEM) using the Hitachi S-800 Scanning Electron Microscope at the Nanotechnology Research & Education Center at the University of South Florida.

5.2: The Interface of Self-Assembled TPP-S on Au

The focus of the PES measurements of self-assembled TPP-S monolayers on Au was the characterization of the formed interface. The potential application of TPP-S in the self-assembly of nanowires or larger networks, containing derivatives of TPP, make a detailed study of the charge transfer across the interface interesting. PES measurements allow for the determination of interface dipoles and charge injection barriers, which are generally present at metal/organic interfaces and can potentially obstruct charge transfer.

Figure 45 shows the XPS high resolution spectra of the C1s, N1s and S2p region recorded for the clean Au substrate and the formed TPP-S monolayer. The C1s emission feature of the TPP-S monolayer exhibits one strong asymmetric peak located at around 284.5 eV, which is related to the aromatic hydrocarbons of the porphyrin molecule. The binding energy of this peak is in good agreement with literature values obtained for various porphyrin molecules, which all have aromatic carbon emissions in common [71, 183-186]. The C1s emission feature was not expected to show any shoulders due to the fact that only one type of carbon bonds is present in the tetraphenylporphyrin molecule.

Tetraphenylporphyrin and its derivatives usually contain four nitrogen atoms in the center, which are of pyrrolic (-NH-) and iminic (-N=) nature. The binding energies for the emission lines associated with these two types of nitrogen were already extensively investigated in the past, and were assigned to iminic (398 eV) and pyrrolic (400 eV) nitrogen with almost equal intensities [73, 184-190]. The N1s emission feature observed for the TPP-S monolayer shows a broad peak ranging from around 396 eV to 401 eV.

Due to the low signal to noise ratio it is difficult to identify the emission lines that contribute to this feature. However, its broadness suggests that it may consist of the two pyrrolic and iminic nitrogen related lines. The low signal to noise ratio of the nitrogen emission feature additionally implies that only a small amount of TPP-S was deposited which is consistent with the formation of a monolayer on the Au surface.

The porphyrin derivative used in the presented experiment contains thiol groups at its peripheral positions, through which the molecule can bond to the substrate surface. By analyzing the S2p emission feature using XPS, one can determine the quality of the assembled monolayer and the presumed orientation of the molecules. The right panel in

Figure 45 displays the high resolution spectrum of the S2p region. A broad peak can be seen here for the TPP-S monolayer at about 164 eV. The S2p emission feature is in general a doublet that contains two emission lines separated by 1.2 eV and exhibiting a 2:1 area ratio [191]. Due to the broad nature of the peak seen in Figure 45, it is reasonable to assume that it consists of more than one doublet. Two doublets were therefore fitted with a Gaussian-Lorentzian peak fit into the background removed S2p emission peak and the result is shown in Figure 46.

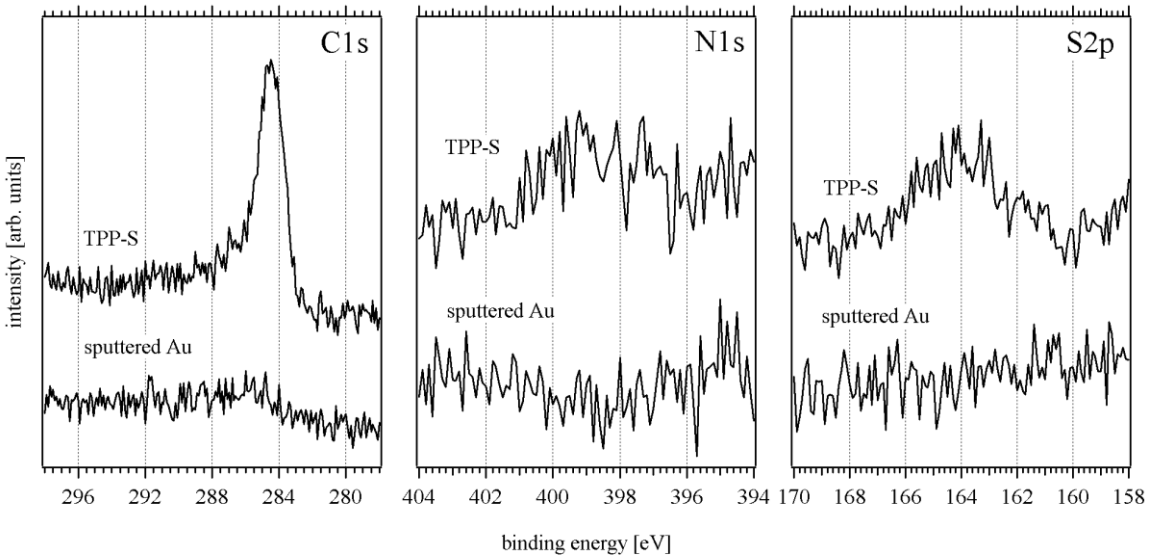

Figure 45: XPS high resolution spectra of the C1s, N1s and S2p emission features of TPP-S.

The two doublets are located at 161.54 ±0.2 eV (considering the low signal to noise ratio) and 163.94 ±0.2eV and exhibit full widths at half maximum (FWHM) of 1.6. The fitted doublet at lower binding energy can be attributed to sulfur bound to the gold substrate and is in good agreement with published values [33, 80, 87, 156, 191-194]. While the first doublet corresponds to thiol-functionalized monolayers covalently bound to gold, the second doublet at higher binding energy can be assigned to the presence of unbound thiol groups [82, 87, 88, 194].

The intensity ratio between bound and unbound thiols is 1:2.1 which means that, on average, about one to two out of four thiolates per porphyrin likely bond to the gold substrate. Since sulfur has a high affinity to gold, it is expected that all sulfur atoms should bond to the surface, which would result in a coplanar orientation of the molecules with the Au surface. Hence, it is surprising why about half of the thiol groups did not bond with the Au surface. Oxidation of the thiol groups as a reason for unbound sulfur can be excluded since this would result in an emission line at higher binding energies of approximately 167 eV [80].

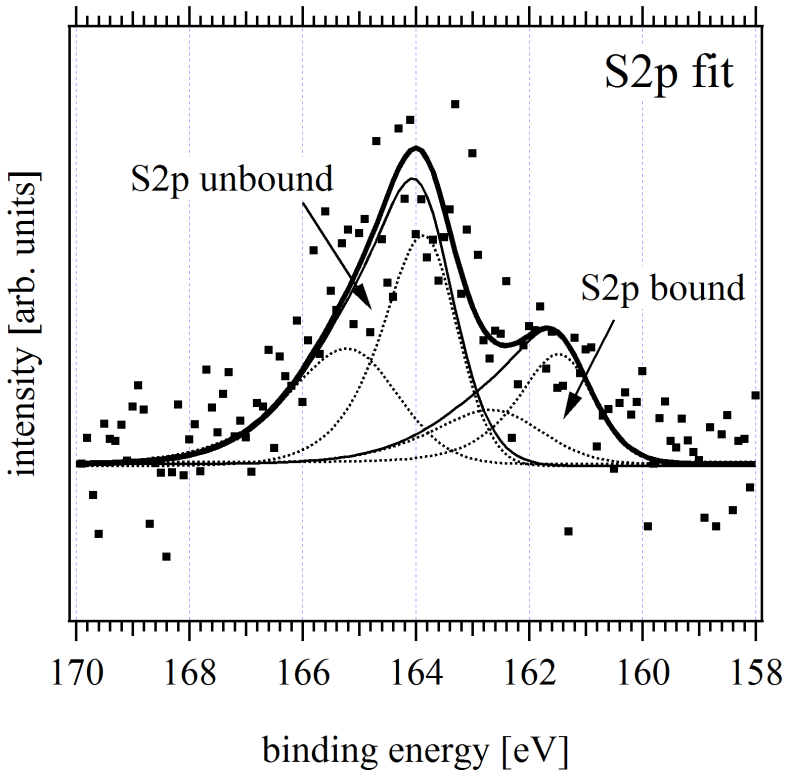

Figure 46: XPS high resolution spectrum of the sulfur emission feature of the TPP-S monolayer with two fitted doublets. The dotted lines symbolize each of the $S2p_{1/2}$ (lower intensity) and $S2p_{3/2}$ (higher intensity) related emission features that contribute to the doublets. The doublet at lower binding energy is related to sulfur bound to gold while the second doublet at higher binding energy originates from unbound sulfur.

This leads to the hypothesis that the self-assembled TPP-S molecules do not exhibit a coplanar orientation, but may be positioned on their edge at an angle to the surface, as shown in Figure 47. In fact, the self-assembly of thiol-derivatives of TPP, which orient themselves at a low angle away from the surface, was reported previously [88, 184, 195] with layer thicknesses in the range of 10-20 Å, depending on the employed thiol group.

If the TPP-S molecules are in fact positioned at their edge, this would also mean that the intensity of the emission line attributed to the sulfur atoms located at the Au/TPP-S interface would be significantly attenuated as a result of the porphyrin molecule located above the bound sulfur. Therefore, the originally calculated ratio between unbound and bound sulfur could be lower than the actual ratio, indicating that on average two or more sulfur atoms bonded with the Au substrate, which would be more in agreement with an angled assembly.

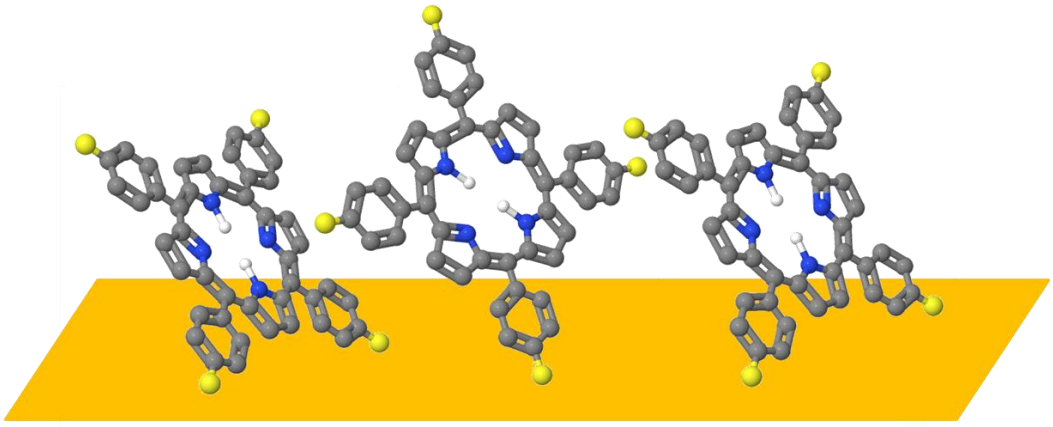

Figure 47: Orientation in which the TPP-S molecules most likely assembled on the Au surface. On some of the molecules only one thiol group presumably bonded with the substrate, while on others two or more could have bonded.

The amount of unbound sulfur could however be also explained with the presence of excessive TPP-S molecules atop of the self-assembled TPP-S monolayer. The attractive interactions between porphyrins can lead to crystal formation and such aggregations are a common occurrence in porhyrin solutions [196, 197]. Although this would explain the unbound sulfur, it would stand in contrast to the low intensities of the nitrogen, carbon and sulfur emission lines that imply that only a small amount of TPP-S is present at the surface. Furthermore, the sample was rinsed with DCM after the incubation was completed, which can effectively remove weakly adsorbed molecules (as observed for TPP, CoTPP and TPP-CN) from the surface. It was also shown in the past that organic solvents can disrupt the interaction between porphyrins and easily open up folded or stacked conformations [198]. Hence, if excessive TPP-S molecules adsorbed on the self-assembled monolayer, they most likely would be removed from the surface during the rinsing step.

The analysis of the $Au4f_{7/2}$ emission line at 84 eV before and after deposition (Figure 48) was used to determine the thickness of the layer. The intensity ratio between the emission lines before and after incubation is 1.5 and using 33 Å as the mean free path of electrons in tetraphenylporphyrins [80, 81], a monolayer thickness of 13.7 Å can be calculated. This is in good agreement with the dimensions of TPP-S molecules (15 Å length; 11 Å width) and suggests that the TPP-S molecules likely assembled on their edge. Conversely, an assembly of TPP-S molecules with a coplanar orientation should result in a thickness close to 5 Å [199].

The particular orientation assumed by the TPP-S molecules during the self-assembly could be explained due to a high concentration of the molecules in the solution

and an oversaturation of the surface with TPP-S molecules during incubation, creating a dense monolayer in which not all of the thiol groups were able to bond with the Au surface.

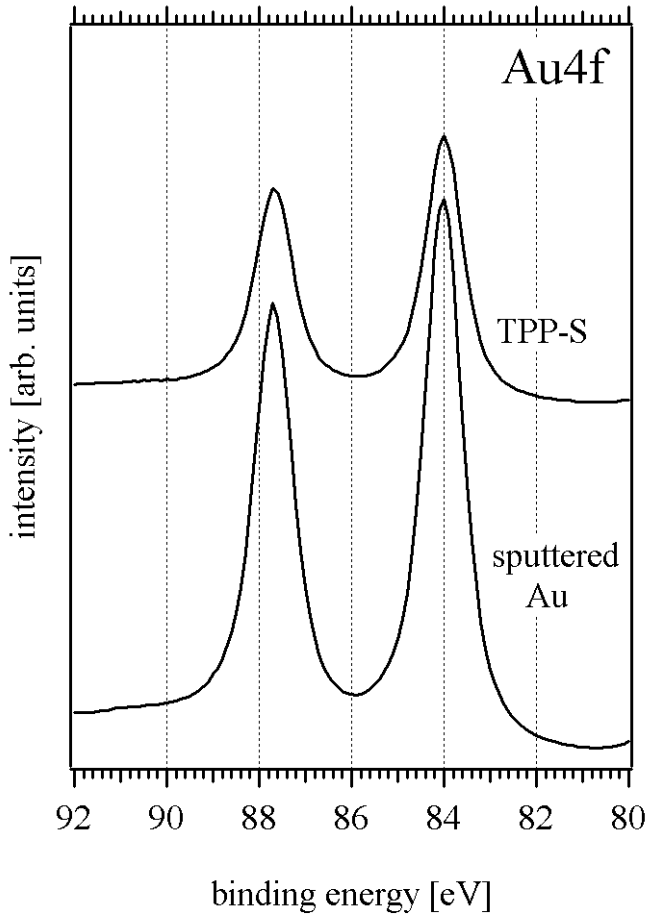

Figure 48: XPS high resolution spectrum of the substrate related Au4f peak. Upon TPP-S monolayer self-assembly, the intensity of the emission feature drops significantly, and the ratio between intensities before and after incubation allows for an estimation of the monolayer thickness.

While the XPS measurements of the TPP-S self-assembled monolayer give insight into the chemical composition of the film, the UPS measurements (shown in Figure 49) provide detailed information about the highest occupied molecular orbital (HOMO) of the monolayer and the band alignment between the substrate and the

monolayer at the interface. The secondary edges of the spectra shown in the left panel are located between 16 eV and 18 eV and are defined by the work function of the sample.

The secondary edge noticeably shifted to a higher binding energy after incubation, which indicates that the work function of the sample decreased due to the interaction between the Au surface and the molecular film. The work function of the TPP-S monolayer was estimated to be 4.69 eV, while the Au substrate exhibited a work function of 5.53 eV.

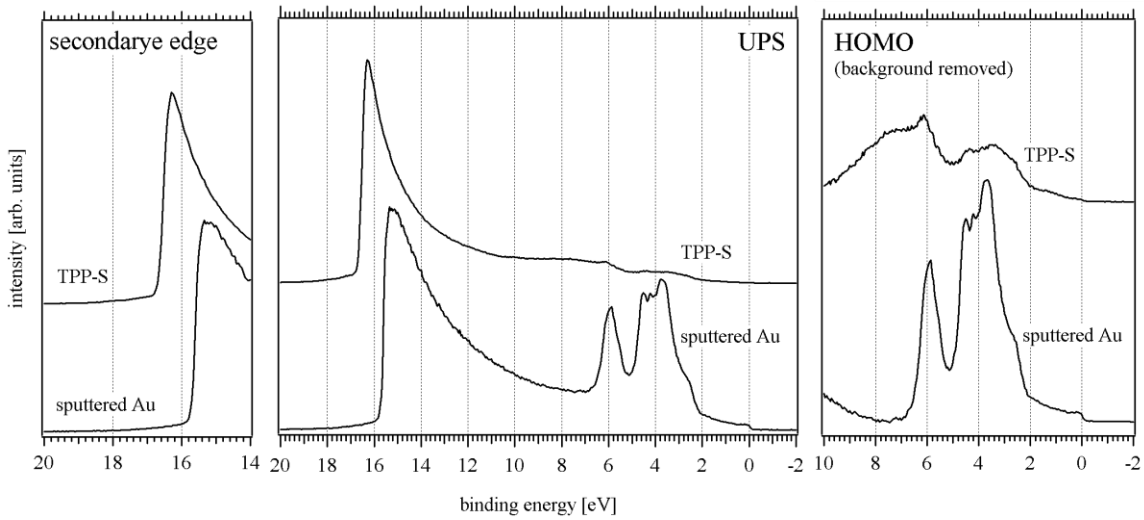

Figure 49: The UP-spectrum of a self-assembled TPP-S monolayer (top) and the sputtered Au surface (bottom) is shown in the middle, while the secondary edges are shown on the left. The HOMO region at lower binging energies, from which the background was subtracted, is shown on the right.

The change in work function indicates the formation of an interface dipole eD of 0.84 eV. This dipole is in good agreement with dipoles measured by other groups on monolayers of metalloporphyrins, such as CoTPP and ZnTPP, and free base porphyrins deposited on Au by evaporation [71, 127, 129, 199-201]. In these experiments, the dipoles varied between 0.57 eV (ZnTPP) and 1.01 eV (TPP). The reduction of the work function can mainly be attributed to Pauli repulsion between the electrons of the TPP-S

molecule and the gold surface. Through this 'cushion-effect', the charge density between the TPP-S molecules and the gold surface is depleted, leading to a modification of the dipole layer [202].

The right panel of Figure 49 shows the top edges of the spectra located directly below the Au Fermi energy (0 eV) and correspond to the valence bands/highest occupied molecular orbitals. The formation of the TPP-S monolayer gave rise to spectral lines corresponding to the HOMOs of the deposited molecules. At the same time, the Au valence bands emissions at 0-6 eV below the Fermi level were attenuated. Due to the monolayer character of the TPP-S layer, the valence band emissions of the Au substrate overlap with the HOMO related emissions of the TPP-S monolayer. This is evident in the emissions at the Fermi edge, which are not expected for TPP derivatives, and residual Au valence bands emission at 4 eV and 6 eV.

In order to correctly analyze the HOMO emissions of the TPP-S monolayer, both spectra were normalized to the Fermi edge emissions. This enabled the subtraction of the Au related emissions from the TPP-S spectrum. The TPP-S spectrum after Au emission removal is shown in Figure 50. Three emission peaks dominate the spectrum. The first peak (A) is located at approximately 1.2 eV which corresponds to peak positions reported for TPP [127, 129]. The second peak (B) can be found at around 3 eV but due to the removal of the Au related emissions the spectrum, this peak is slightly distorted in the area between 4 eV and 6 eV and its position may be at a higher energy. A third broad peak (C) is present at approximately 7 eV.

Peak A is attributed to the almost degenerate π orbitals, which are delocalized over the central macrocycle and have major electron densities only on the porphyrin ring

[72, 129, 183, 200, 203], while peak B is assigned to orbitals localized on the phenyl rings [72, 183]. Peak C is a common feature seen in metalloporphyrins and free base porphyrins, and originates from σ orbitals delocalized over the porphyrin ring [71, 72, 201].

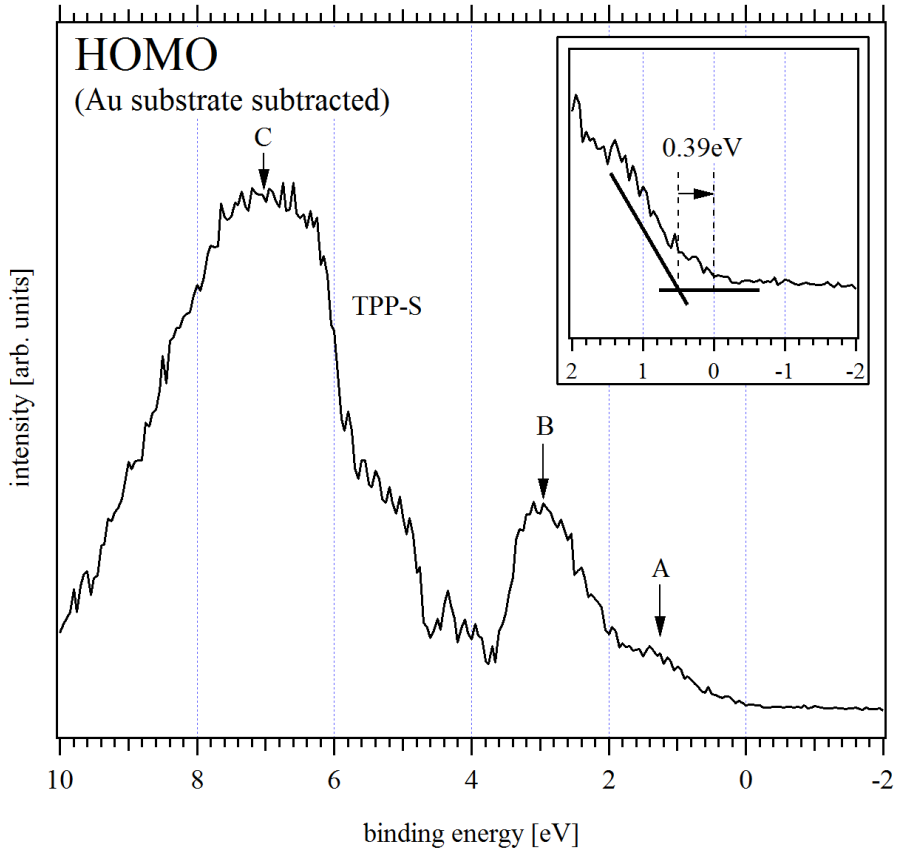

Figure 50: UP-spectrum of the HOMO region of the TPP-S thin film. The emissions from the gold substrate were removed in order to highlight the TPP-S related emission features. The insert shows the low binding energy onset used for the determination of the hole injection barrier.

The insert in Figure 50 shows the low binding energy onset of peak A. This onset is located at 0.39 eV and represents the hole injection barrier Φ_h at the Au/TPP-S interface. The hole injection barrier is considerably lower than values published for thin films of free base porphyrins and metalloporphyrins [71, 127, 129, 183, 199, 201]. This

difference is not surprising since the charge transfer is mediated through the thiol moiety at the periphery of the TPP molecule instead of a metal ion centered in the porphyrin ring or the ring itself, as it is the case for adsorbed free base porphyrins and metallo-porphyrins.

By incorporating the determined work function values and the hole injection barrier, the orbital line-up at the Au/TPP-S interface can be established, as shown in Figure 51. The band line-up displays the work function Ψ_{Au} of the clean Au substrate and the existing interface dipole eD. The hole injection barrier Φ_h of 0.39 eV, as determined from the UPS measurements, poses a limitation for charge injection into the monolayer, although it is lower than what was reported for other TPP derivatives. By subtracting the value for Φ_h from the transfer gap of the TPP-S molecule, the electron injection barrier Φ_e, which is the onset of the lowest unoccupied molecular orbital (LUMO), was calculated. Since transfer gap values for TPP and its derivatives vary from 2.34 eV to up to 2.9 eV in literature [204, 205], the average of these values (2.62 ±0.28eV) was assumed for the transfer gap of TPP-S. TPP-S is a novel TPP derivative and the exact value of the transfer gap is as of yet unknown. Therefore, the assumed value needs to be considered a rough estimate. With this transfer gap value, the electron injection barrier Φ_e was estimated to be 2.23 ±0.28 eV.

Adding the work function of TPP-S to the hole injection barrier Φ_h resulted in the value for the ionization energy E_{ion} of the TPP-S monolayer. The ionization energy E_{ion} is with 5.08 eV somewhat lower than the 5.3 eV that were reported for multilayers of ZnTPP and TPP in the past [127, 129, 201], but this difference can be simply explained with the lower hole injection barrier of the TPP-S monolayer. It was reported in the past

that a correlation between ionization energy and conduction type exists for porphyrins [201]. A value of 5.03 eV suggests that TPP-S exhibits p-type character, like ZnTPP and TPP molecules, and higher ionization energies were reported for porphyrin derivatives of n-type character [201]. A comparable link between the ionization energy and conduction type of phthalocyanine derivatives was made in the past as well [206].

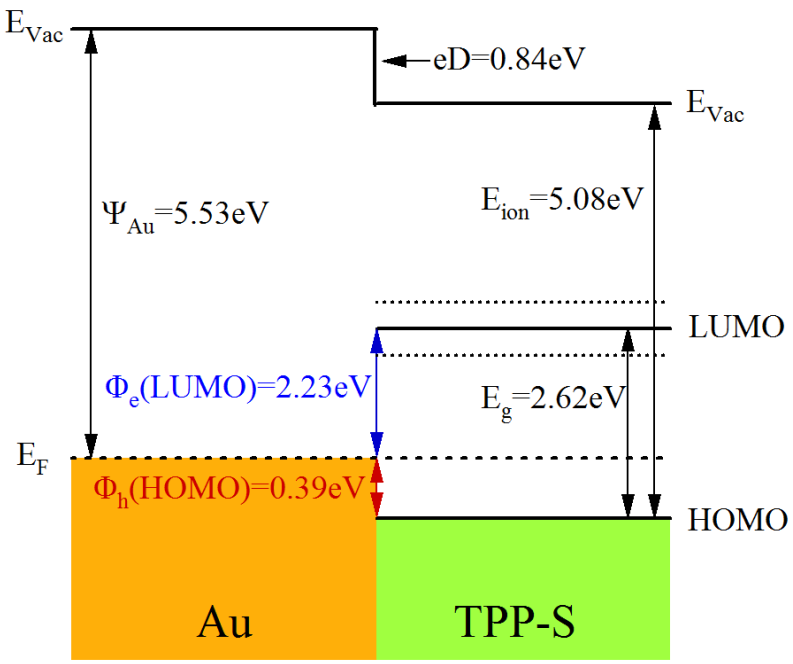

Figure 51: Band line-up of the Au/TPP-S interface as determined from the UPS measurements. The dotted lines indicate the uncertainty of the estimated LUMO level.

The measurements demonstrate in conclusion that the deposited TPP-S molecules form a monolayer on gold from solution. The data suggests that the molecules have a predominantly angled orientation in contrast to the coplanar orientation of adsorbed free base porphyrins and metalloporphyrins. The bond formed between the sulfur atoms and the Au surface offers means for charge transfer between substrate and molecule, due to the low resulting hole injection barrier of 0.39 eV.

TPP-S offers the possibility to create a stable monolayer with a low hole injection barrier and the fact that only one to two thiol groups have to bond with the surface for successful monolayer formation, leaves at least two phenyl rings open for chemical modifications. The modifications could include functionalized groups which can lead to interactions between neighboring molecules (and charge transfer parallel to the surface) and offer bonding sites for other organic molecules on top of the formed monolayer (for charge transfer perpendicular to the surface).

5.3: The Electronic Structure of TPP-CN Arrays Formed on Au

The coupling of structurally different molecules by coulombic interactions represents a powerful technique for the self-organization of building blocks and the creation of new materials. This so-called ionic self-assembly is usually accompanied by a cooperative binding mechanism resulting in reliable self-assembled structures [90]. It offers an inexpensive and flexible way of self-assembly and allows for a broader range of applications than offered by regular hydrogen-bonding. In this context, a study of TPP array formations driven by electrostatic interactions can provide information on the feasibility of ionic self-assembly for the creation of molecular long-range conductive wires. The following experiments were designed to investigate the coulombic binding of Ag ions with nitrogen groups located at the periphery of TPP-CN molecules. For this purpose, the Au substrates were exposed to silver nitrate (Figure 52) prior to sample incubation, which resulted in the formation of TPP-CN arrays through ionic self-assembly. These networks could be potentially used to incorporate functionalized TPP derivatives or other organic molecules with optoelectronic or biosensing capabilities, resulting in a self-assembled molecular circuit.

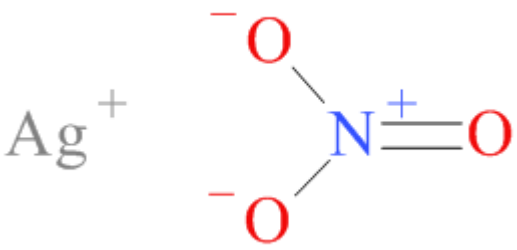

Figure 52: The inorganic compound silver nitrate, which has the chemical formula $AgNO_3$

In the presented study, the TPP derivative TPP-CN was studied with XPS, LIXPS and UPS in order to characterize the electronic structure of the formed TPP-CN thin films and investigate the impact of $AgNO_3$ on the quality of the deposited organic thin films. As mentioned in the experimental section of this chapter, TPP-CN was deposited on a gold substrate by incubating the sample in TPP-CN solution for 10 minutes, while in a separate experiment, $AgNO_3$ was electrospray deposited on a gold substrate prior to TPP-CN incubation. The electrospray approach was chosen in order to achieve a homogenous deposition of silver nitrate on the Au surface without exposing it to the ambient atmosphere. This allowed a direct comparison between samples with and without Ag present during assembly.

Figure 53 shows the XPS high resolution spectra of the C1s, N1s, Ag3d and O1s regions of the TPP-CN film (TPP-CN), the substrate after $AgNO_3$ deposition (Ag^+), and the TPP-CN film after $AgNO_3$ exposure (TPP-CN/Ag^+). The C1s emission line for TPP-CN has a binding energy of about 284.9 eV and is in agreement with the peak location in the TPP-S experiments (compare 5.2) as well as with literature reports [71, 183-186]. This peak shifted by about 0.4 eV in the TPP-CN/Ag^+ experiment, where it has a binding energy of 284.5 eV.

The N1s emission feature of the TPP-CN film consists of at least two emission lines. This is expected since the TPP molecule contains pyrrolic (-NH-) and iminic (-N=) nitrogen. The two emission lines are located at about 398 eV and 399.5 eV, which is in good agreement with values obtained for both species of nitrogen in other experiments [73, 184-190, 199]. Conversely, the $AgNO_3$ film only shows one N1s feature located at about 406 eV. This peak corresponds to published values for $AgNO_3$ [207-209]. Adding TPP-CN to the $AgNO_3$ covered Au substrate results in the return of the pyrrolic and iminic lines, while the $AgNO_3$ related N1s peak decreases in intensity. The TPP-CN/Ag^+ related N1s peaks are with approximately 399 eV and 397.5 eV at slightly lower binding energies than for the pure TPP-CN film and the shift of the binding energies may be an indicator for Ag-N bond formation.

The $Ag3d_{5/2}$ line for both, the deposited $AgNO_3$ and the TPP-CN/Ag^+ film, is located at around 368 eV and the energy of these peaks is similar to literature values [207, 209]. The $Ag3d_{5/2}$ emission line of the TPP-CN/Ag^+ film displays a small shift to higher binding energies, which is likely related to Ag-N interaction. The intensity drop after TPP-CN incubation is a result of the solvation of a fraction of the deposited $AgNO_3$ from the surface into the TPP-CN solution. This hypothesis is also in agreement with the intensity decrease of the $AgNO_3$ related N1s emission line.

The O1s spectrum of the TPP-CN film shows a small and broad peak at around 532 eV. Since neither TPP-CN nor the solvent (DCM) contain oxygen, it can be assumed that this peak is related to residual surface contamination of the Au substrate. The spectra for Ag^+ and TPP-CN/Ag^+ show both a strong emission line at around 532 eV which is related to $AgNO_3$ and is in close agreement with published values [207, 209].

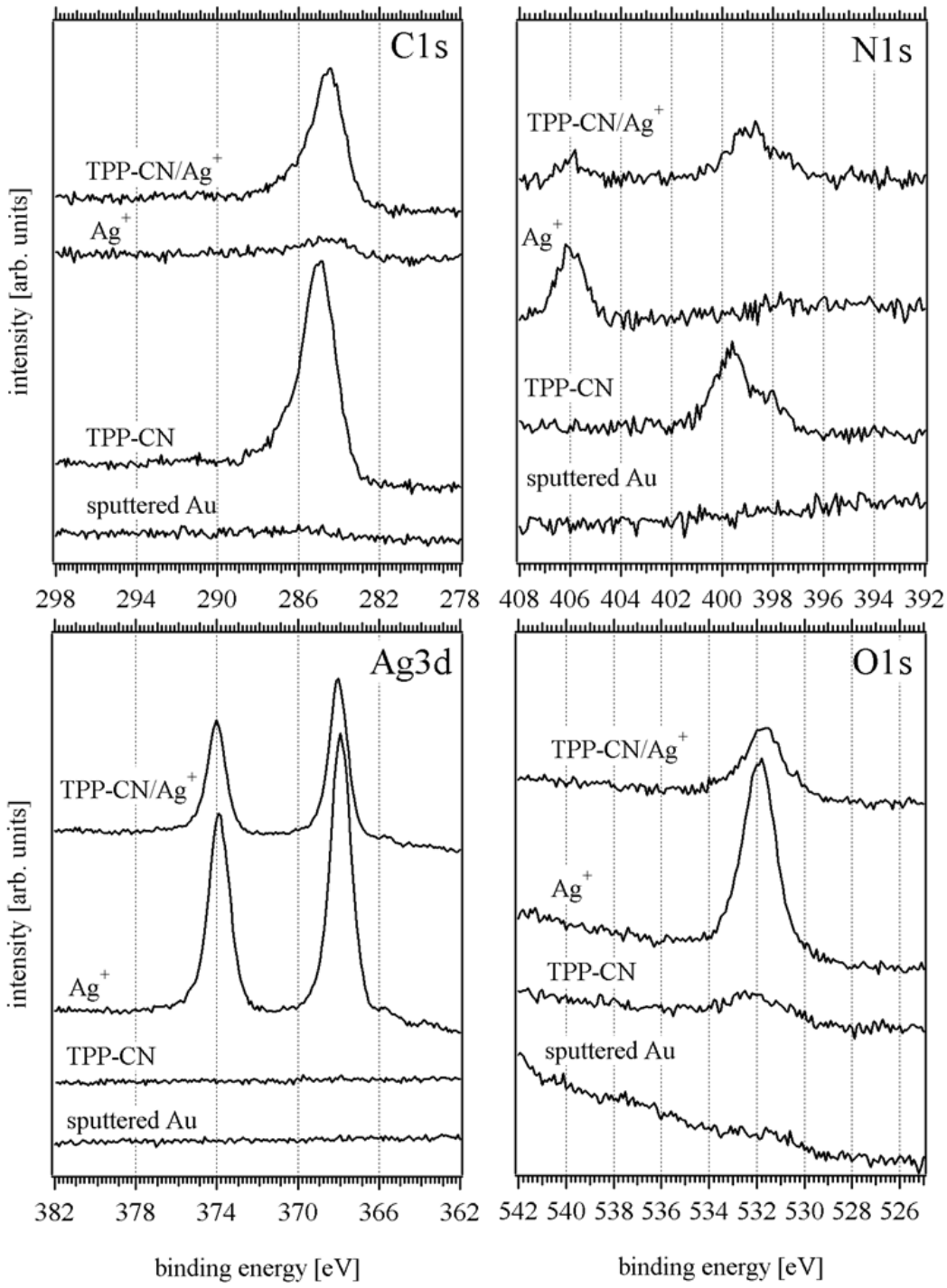

Figure 53: The high resolution XP-spectra of the C1s, N1s, Ag3d and O1s emission features for TPP-CN, $AgNO_3$ (Ag^+) and TPP-CN with $AgNO_3$ (TPP-CN/Ag^+)

5.3.1: Bond Formation Between Ag and N

The N1s emission feature is an important indicator for the interaction between the Ag atoms and the TPP-CN molecules. The incorporation of metal atoms in the center of porphyrins results in bond formations between the nitrogen atoms and the metal atom and leads to the appearance of a new emission line commonly observed between the emission lines of pyrollic and iminic nitrogen [71, 73, 186, 199]. To study the possible presence of this third peak, the TPP-CN and TPP-CN/Ag^+ related N1s emission features were fitted with Gaussian-Lorentzian fits after background removal and the results are shown in Figure 54. The TPP-CN related emission feature was fitted with two peaks located at 399.68 eV and 398.08 eV. These peak positions are similar to values reported for pyrrolic and iminic nitrogen of various metalloporphyrins and free base porphyrins [73, 184-188, 199, 210, 211]. The intensity ratio between the pyrrolic and iminic nitrogen peaks was estimated to be 2.4:1. This ratio reflects the presence of the six pyrrolic and two iminic nitrogen atoms incorporated into the TPP-CN molecule.

The spectrum of the N1s emission feature of the TPP-CN/Ag^+ film exhibits a higher amount of noise, making the fitting procedure and peak location slightly more difficult. However, literature suggests that films of porphyrins with electrostatically bound metal atoms exhibit a third emission line in the N1s binding energy range in addition to the pyrrolic and iminic lines. The N1s emission feature was therefore fitted with three peaks. The emission peaks of pyrrolic and iminic nitrogen can be found at 399.22 eV and at 397.56 eV, respectively, representing a shift of 0.46 eV and 0.52 eV towards lower binding energies in comparison to the TPP-CN film. The mentioned third peak is positioned in between the emission lines of pyrrolic and iminic nitrogen at

398.62 eV. The binding energy of this peak is similar to values published for a wide range of metalloporphyrins [71, 73, 186, 199] and suggests that an interaction between the deposited Ag atoms and the TPP-CN molecules took place. Based on the fitted emission peaks, it can be assumed that the Ag atoms likely bonded to some extent with the pyrrolic and iminic nitrogen located at the center of the molecule.

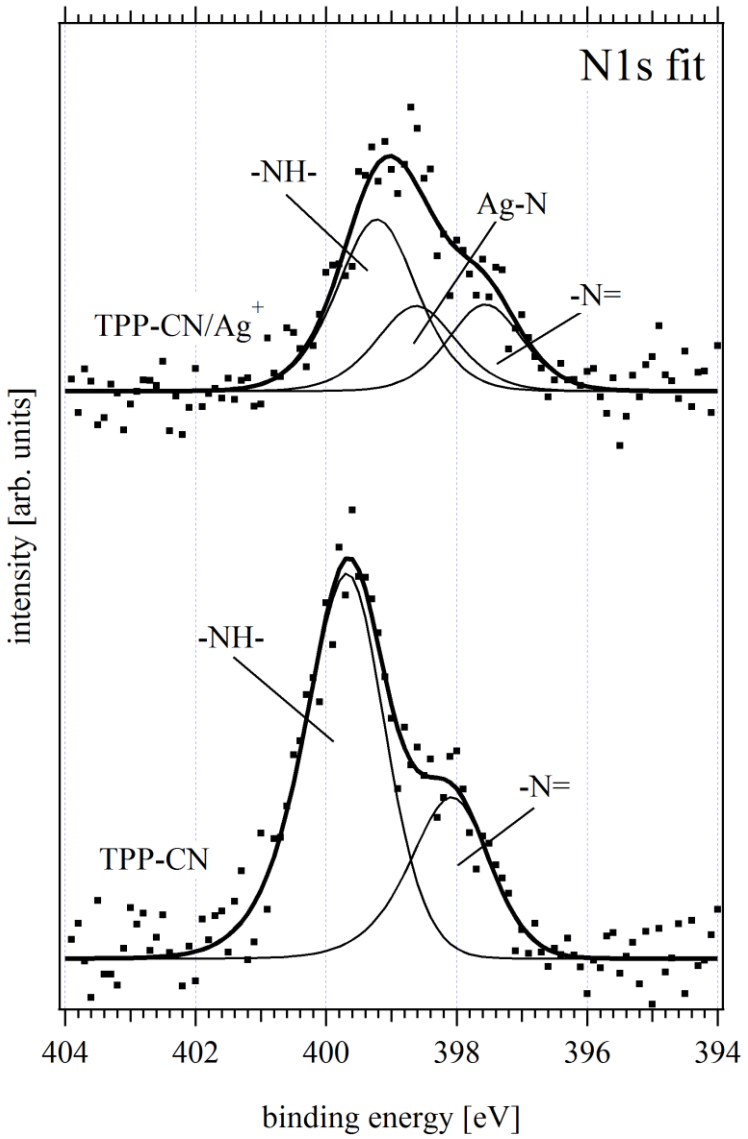

Figure 54: Gaussian-Lorentzian fits of the N1s emission features of TPP-CN and TPP-CN with $AgNO_3$. While TPP-CN alone can be fitted with two peaks related to pyrrolic and iminic nitrogen, the emission of the TPP-CN/Ag^+ film can be fitted with an additional third peak, which is attributed to the Ag-N bond.

Such a 'pick up' of metal atoms by free base porphyrins was reported for Zn, Co and Fe in the past [73, 187, 188]. The interaction driven by coulombic bonding between the nitrogen and silver atoms is also evident in the change of the intensity ratio between pyrrolic and iminic nitrogen. The ratio of 1.98:1 indicates that less pyrrolic nitrogens are present in the TPP-CN/Ag^+ film in comparison to the TPP-CN film. This corresponds with the hypothesis that the pyrrolic nitrogen atoms on the periphery of the TPP-CN molecule presumably bonded with the silver atoms present in $AgNO_3$.Further proof for electrostatic interaction between the TPP-CN molecules and Ag atoms was obtained by comparing the N1s emission features shown above to PES measurements conducted on TPP-CN deposited on Ag, CoTPP on Au, and TPP on Au. The N1s emission features of all TPP films were fitted with Gaussian-Lorentzian fits and the resulting peaks are shown in Figure 55 for comparison. The peak positions of pyrrolic nitrogen, iminic nitrogen, and nitrogen in a metal bond are indicated with the dotted lines and the exact values are given in Table 3.

Table 3: Nitrogen related peak position for several TPP derivatives in eV. The investigated nitrogen species are pyrrolic (-NH-), iminic (-N=) and nitrogen bound to a metal atom (M-N)

	-NH-	**M-N**	**-N=**
TPP-CN on Au	399.68		398.08
TPP-CN/Ag+ on Au	399.22	398.62	397.56
TPP-CN on Ag	399.58		398.08
CoTPP		398.24	
TPP	399.68		397.9

The binding energies of pyrrolic and iminic nitrogen are similar in value for films containing TPP or TPP-CN, but are on average about 0.4 eV higher than what was

measured for the TPP-CN/Ag^+ film. Conversely, the emission line attributed to the metal-nitrogen bond in the CoTPP molecules exhibits a binding energy which is 0.38 eV lower than of the corresponding emission line of the TPP-CN/Ag^+ film. The observed shifts of roughly 0.4 eV in opposite directions are likely charge transfer related and indicate a donation of electrons from the Ag atom towards the TPP-CN molecule across the Ag-N bond.

The difference in peak positions between the TPP-CN film deposited on Ag and the TPP-CN/Ag^+ deposition on Au suggests that the clean Ag surface is not sufficient for the formation of coulombic bonds between the molecules. The presence of Ag ions on the surface in a salt (like $AgNO_3$) is most likely a prerequisite for electrostatic interaction.

The fraction of ions which formed Ag-N bonds with the TPP-CN molecules can be estimated by comparing the stoichiometric ratios between the N1s and $Ag3d_{5/2}$ emission peaks of the $AgNO_3$ compound before and after incubation. For this purpose the background was removed from the N1s emission peaks located at 406 eV, which are attributed to $AgNO_3$, and the $Ag3d_{5/2}$ peaks at 368 eV (see Figure 56). The areas of these peaks were integrated and the resulting values were adjusted for the specific ionization cross sections by employing the characteristic Scofield factors [145]. The N1s and $Ag3d_{5/2}$ emission peaks should exhibit a theoretical stoichiometric ratio of 1:1 for $AgNO_3$ and a formation of coulombic bonds between Ag and TPP-CN molecules is supposed to lead to a change in the stoichiometric ratio as the leftover nitric acid component of $AgNO_3$ should be washed off the surface.

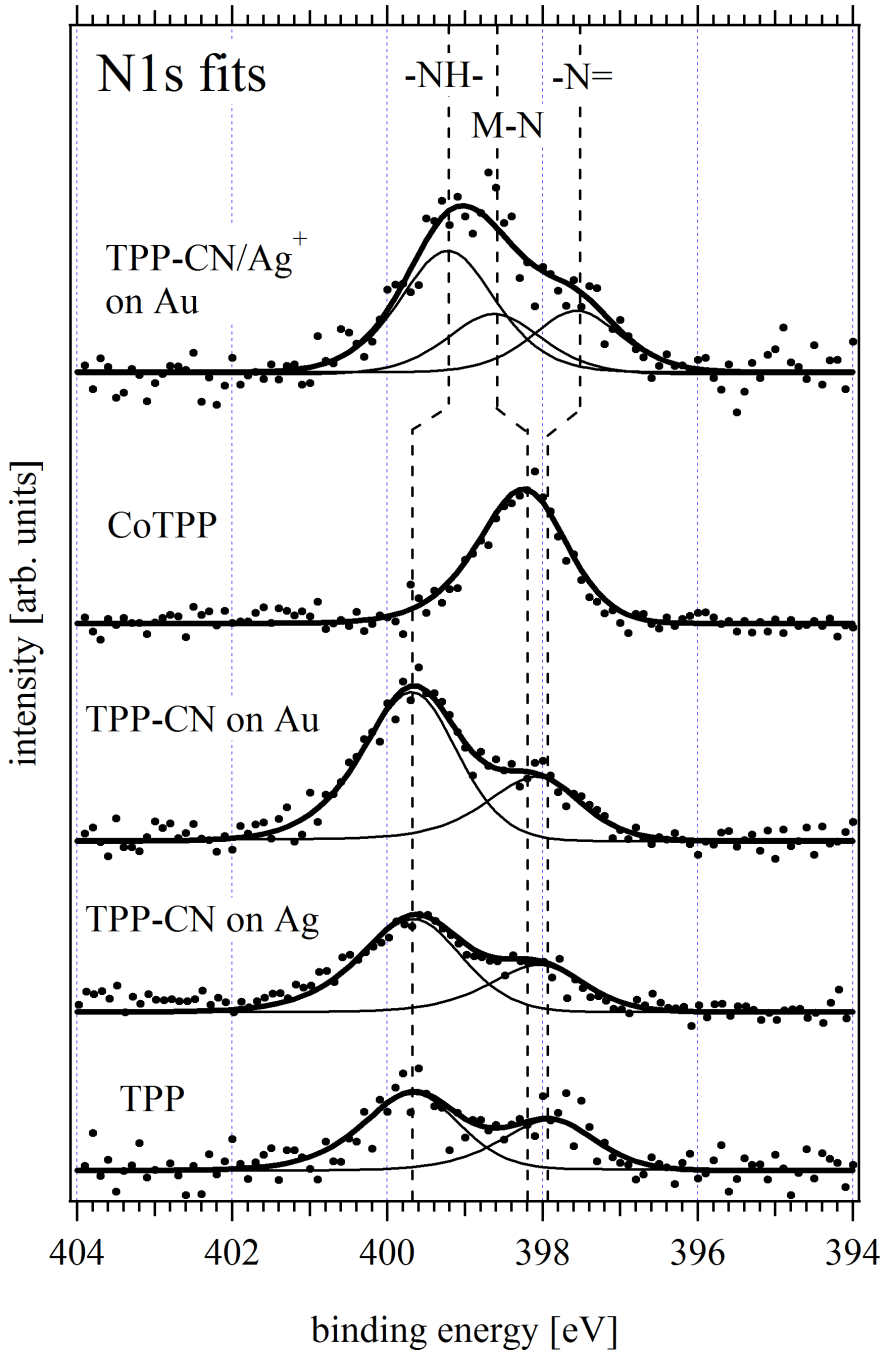

Figure 55: High resolution XP-spectra of the N1s region with Gaussian-Lorentzian fits. The dotted lines symbolize the peak positions of pyrrolic nitrogen (-NH-), iminic nitrogen (-N=), and nitrogen in a metal bond (M-N).

The calculated stoichiometric ratio between nitrogen and silver in the $AgNO_3$ film prior to incubation resulted in a value of 1:2.63. This ratio differs from the theoretical

ratio of 1:1, which would be expected for a solution of silver nitrate, containing silver ions and nitric acid. The deposited film could, however, contain Ag agglomerates or oxidized silver particles and less nitric acid, since nitric acid exhibits a relatively high vapor pressure [212] and a significant amount could have evaporated during the electrospray process. This would lead to an increased amount of silver at the surface in comparison to nitric acid.

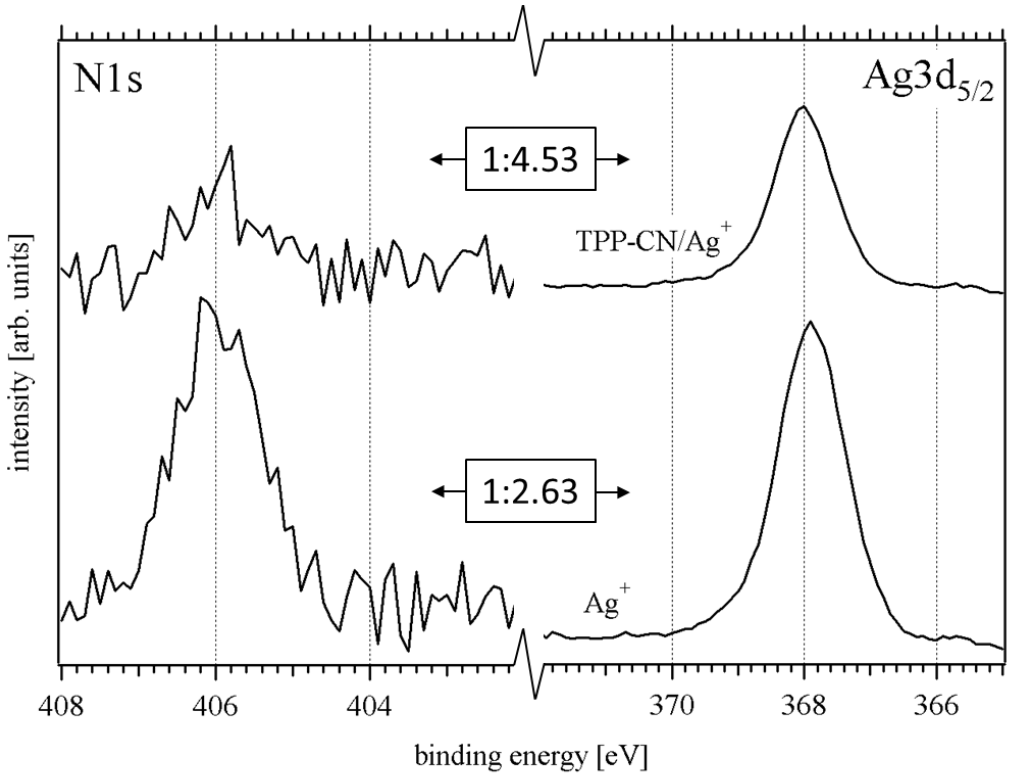

Figure 56: N1s and $Ag3d_{5/2}$ peaks used for stoichiometric ratio calculations with the corresponding ratios displayed in the center.

Since the binding energies for oxidized Ag and Ag found in $AgNO_3$ are very similar [213, 214], it is difficult to distinguish between these two forms of silver. The determined ratio can still be used for comparative purposes as the focus lies here on its change after TPP-CN deposition. The ratio between nitrogen and silver increased to

1:4.53 after TPP-CN deposition, indicating that roughly 42% more Ag atoms than nitric acid molecules remained on the surface. The higher amount of Ag atoms is an indicator for the capture of these atoms in Ag-N bonds.

5.3.2: Charge Transfer Related Binding Energy Shifts

The formation of TPP-CN arrays through coulombic bonds between the Ag atoms and TPP-CN molecules likely resulted in charge redistribution across the bonds. The observed energy shifts in the N1s and C1s spectra of TPP-CN and TPP-CN/Ag^+, and the $Ag3d_{5/2}$ emission peaks of $AgNO_3$ and TPP-CN/Ag^+ are a strong indicator for such a charge transfer. The N1s, $Ag3d_{5/2}$ and C1s related emission features are displayed with their respective Gaussian-Lorentzian fits in Figure 57 for comparison. As mentioned earlier, the emission lines of pyrrolic and iminic nitrogen showed with the introduction of $AgNO_3$ binding energy shifts of 0.46 eV and 0.52 eV, respectively, which are symbolized with dotted lines. The C1s emission peak displayed a similar shift of 0.44 eV from 284.87 eV to 284.43 eV.

The $Ag3d_{5/2}$ emission peak on the other hand exhibits a shift of 0.12 eV to higher binding energies from 367.87 eV to 367.99 eV. The shift of the N1s and C1s peaks to lower binding energies and the shift of the $Ag3d_{5/2}$ peak to higher energies indicate that electrons were donated from the silver atom to the TPP-CN molecule, as electron loss usually results in higher binding energies. The earlier mentioned shift of the nitrogen emission line related to the Ag-N bond to higher binding energies by 0.38 eV, in comparison to Co-N in CoTPP, further supports the assumption of electron donation from the TPP-CN molecule to the Ag atom across the Ag-N bond.

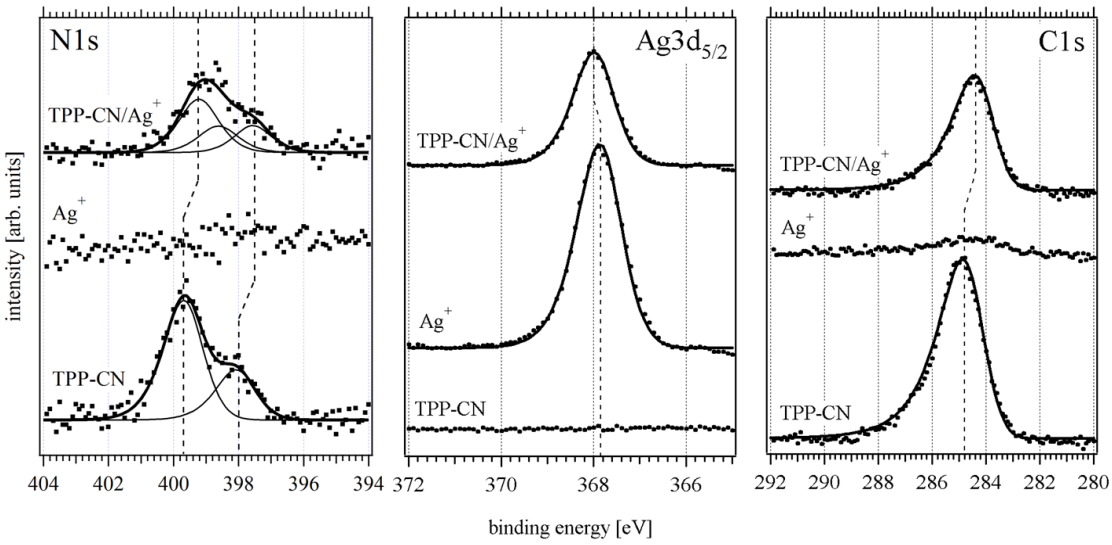

Figure 57: N1s, $Ag3d_{5/2}$ and C1s emission features with Gaussian-Lorentzian fits in comparison. The dotted lines indicate the observed shifts between the different peaks. While the N1s and C1s related emission lines shifted to lower binding energies, the $Ag3d_{5/2}$ related line shifted to higher binding energies.

It should be noted here that the energy shifts may also be a result of final state screening of the organic thin film, as similar changes in binding energies were observed for monolayers of CoTPP and TPP in comparison to their corresponding multilayers [199]. Final state screening occurs when photoelectrons originating from a thin organic layer are screened by the metal substrate, which in return lowers their kinetic energy. This process would result in a shift of the emission features to lower binding energies, as was observed for the N1s and C1s emission features. Although the $Ag3d_{5/2}$ peak shifted to higher binding energies, it should be pointed out that final state screening does not affect metal atoms as it does for organic layers, and this shift could be therefore explained with the uncertainty that comes with PES measurements, since the observed shift is only slightly larger than the energy resolution of the analyzer.

To investigate the possibility of final state screening, the film thicknesses of the deposited TPP-CN films were calculated based on the attenuation of the Au4f emission features shown in Figure 58.

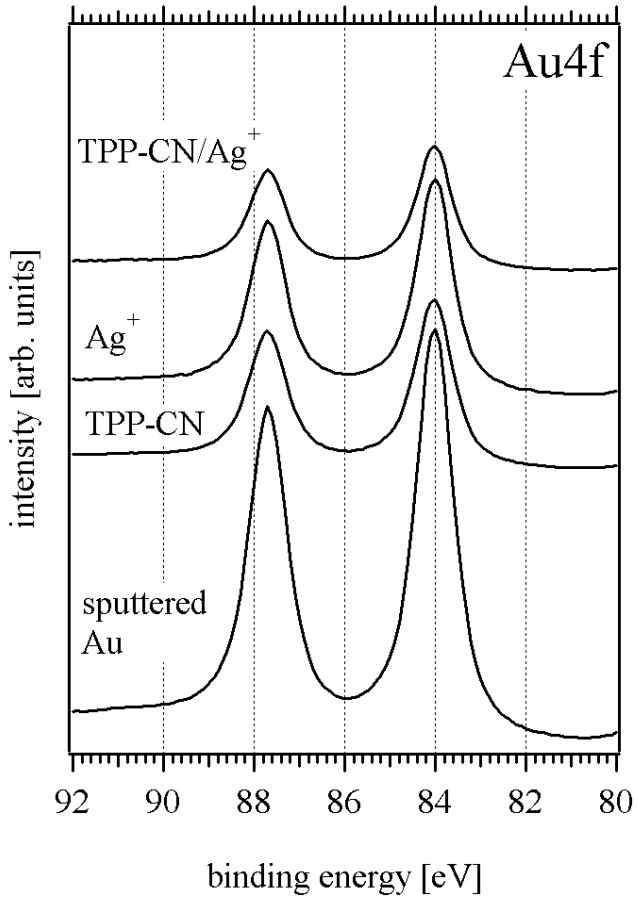

Figure 58: XPS high resolution spectrum of the Au4f emission feature.

By employing a mean free path of electrons in TPP-CN of 33 Å [80, 81], a thickness of 29.4 Å was calculated for the TPP-CN film. The $AgNO_3$ film is expected to exhibit a different mean free path and since stoichiometric ratio calculations showed that nearly three times as many silver atoms are present in the film in comparison to nitric acid, the mean free path for Ag of 12 Å [215] was used in this calculation. The resulting thickness of the $AgNO_3$ thin film was estimated to be 7.7 Å, while it should be pointed

out that this thickness estimation is a rough approximation, as nitric acid is still present in the film, which should alter the mean free path noticeably.

The thickness of the TPP-CN/Ag^+ film was determined to be 39.3 Å by employing a mean free path of 33 Å. The TPP-CN/Ag^+ film must therefore either be thicker in comparison to the TPP-CN film, or contain less pinholes and defects. The presence of Ag atoms in the film can, however, likely reduce the mean free path of electrons, resulting in a lower value for the thickness of the TPP-CN/Ag^+ film. Nonetheless, the calculated value is far off from values of around 5 Å, which would be expected for a TPP monolayer [199].

Based on these thickness calculations, it can be assumed that a multilayer of TPP-CN formed on the Au surface after $AgNO_3$ exposure. Multilayers of organic molecules are usually not expected to exhibit final state screening related energy shifts, which can therefore be safely excluded as the origin of the observed energy shifts.

5.3.3: Surface Characterization of TPP-CN Films Deposited on Au

The XPS measurements present evidence of coulombic Ag-N bonds in the TPP-CN/Ag^+ film. However, they do not allow for conclusions regarding the scale at which these electrostatic interactions took place. The deposited TPP-CN/Ag^+ and TPP-CN films were therefore characterized by employing a scanning electron microscope. Figure 59 shows a SEM image of the TPP-CN/Ag^+ film surface.

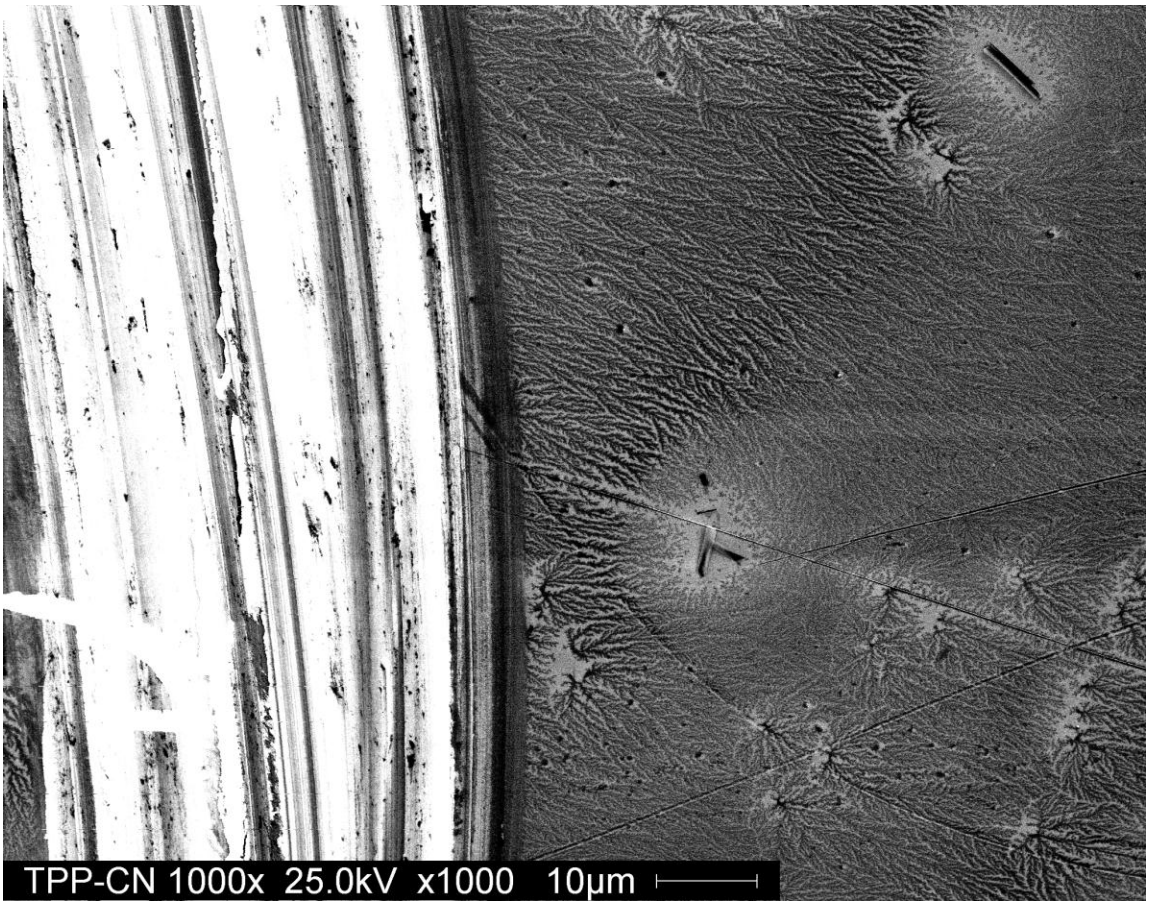

Figure 59: Contrast enhanced SEM image of TPP-CN on Au after $AgNO_3$ exposure. Fine structures formed by the TPP-CN can be seen as well as larger crystals (top right corner and close to center)

The right side of the image clearly displays big, branch-like structures which expand over several µm. Several larger structures, presumably TPP-CN crystals, can be seen in the top and bottom right of the image. These crystals formed likely due to agglomerated material on the surface. It is also evident that the area around these crystals displays a denser film, as no dark background can be seen. Figure 60 shows an enhanced image of the TPP-CN/Ag^+ surface, in which the detailed structure of the observed branches can be seen.

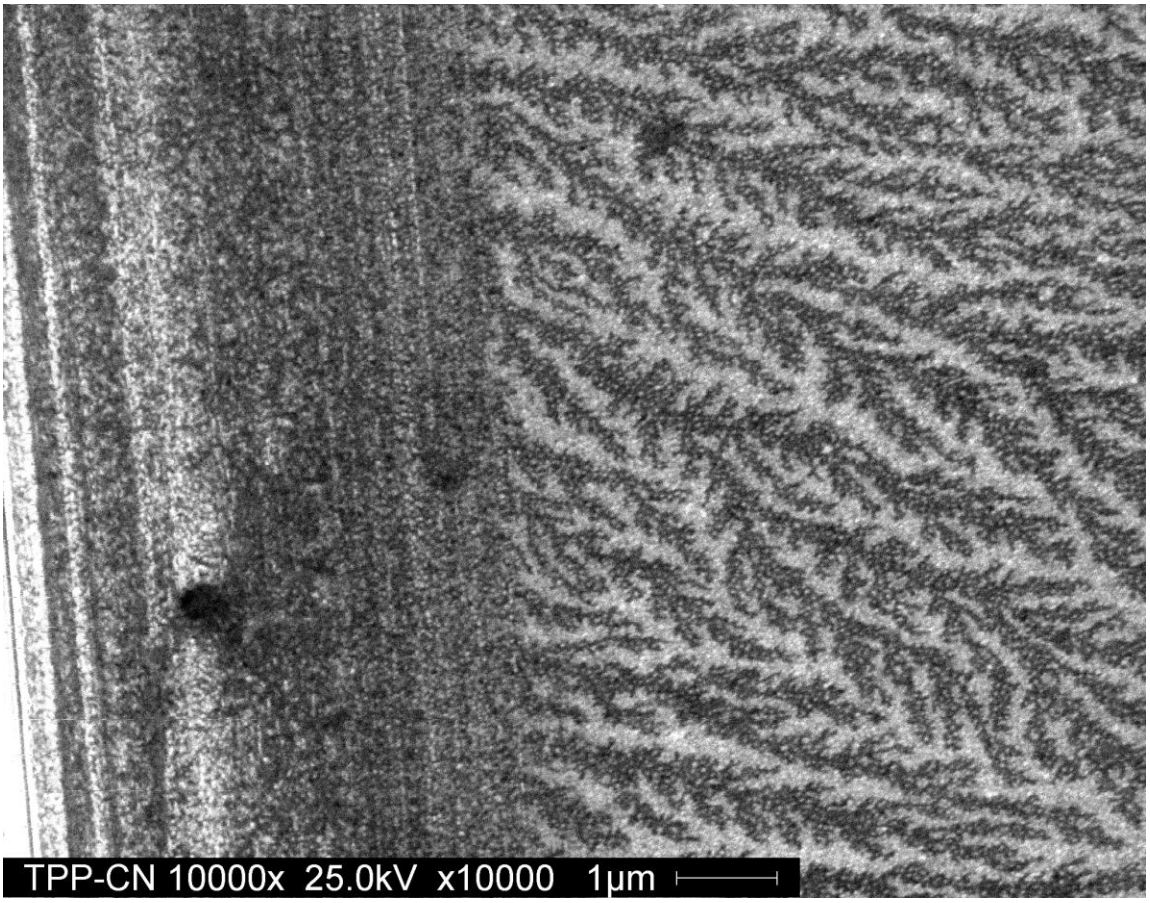

Figure 60: Clearly visible branch-like network formed by TPP-CN in presence of $AgNO_3$ (contrast enhanced image).

The darker background originating from the Au surface can be seen on the left in comparison, as this part was scratched prior to SEM imaging. The branches seemed to have extended into various directions, suggesting an interconnected network of molecules.

A third SEM image was taken of a denser part of the TPP-CN/Ag^+ film and is shown in Figure 61. Here it can be seen that these parts of the film contain finer branches of TPP-CN molecules and even display patches with full substrate coverage. The images support the hypothesis that the bond formation between Ag atoms and TPP-CN

molecules may have resulted in interconnected long-range arrays spanning several μm in length and width.

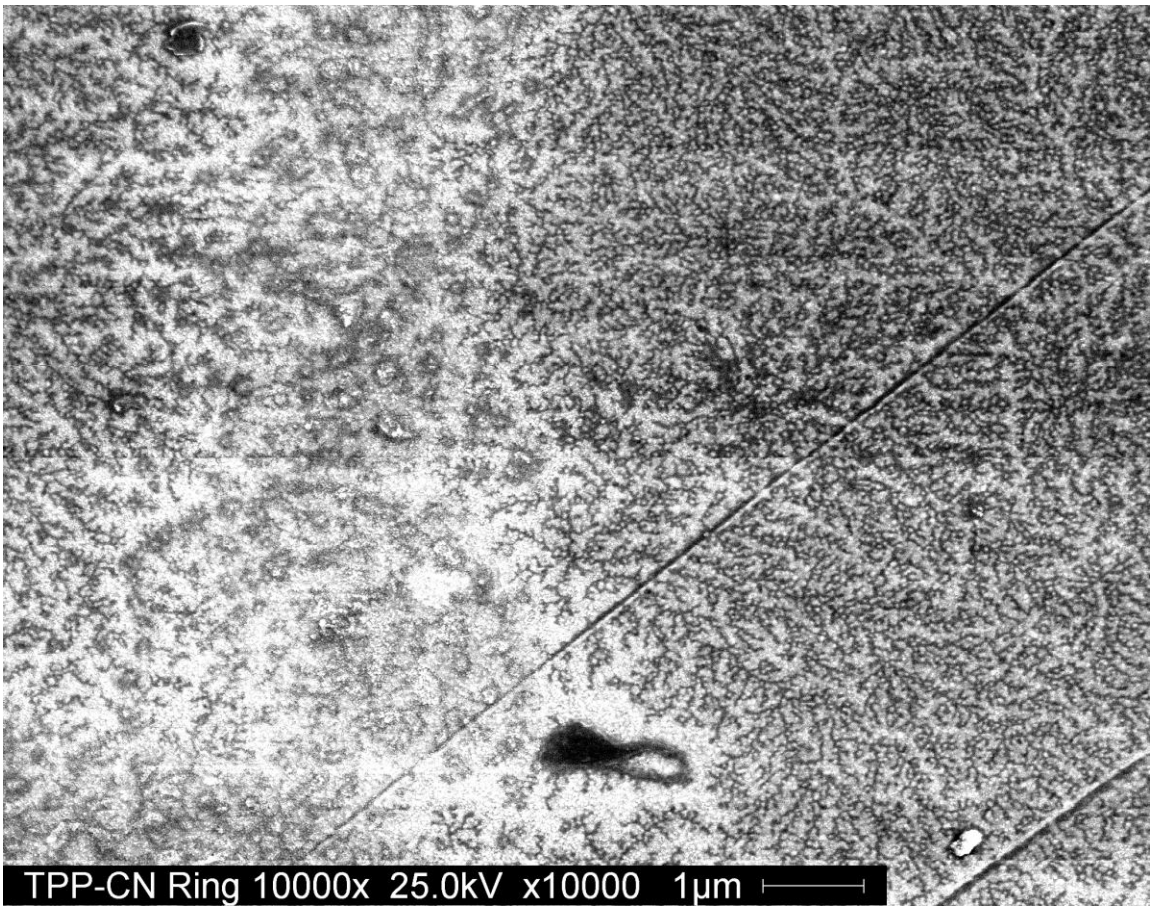

Figure 61: The contrast enhanced image shows an area with a denser TPP-CN/Ag^+ film, exhibiting finer branch-like structures and displaying denser surface coverage (light gray areas)

In order to demonstrate that such an arrangement only takes place with the introduction of $AgNO_3$ prior to incubation, SEM images were obtained for a TPP-CN film on Au. Figure 62 shows a larger area of this film and in comparison to the TPP-CN/Ag^+ film, no branch-like arrays were formed here. Instead, isolated islands of TPP-CN molecules are observed on the surface. A few crystals can also be seen on the right side and the top of the image. These crystals are most likely a result of the

agglomeration of TPP-CN molecules, which is commonly observed in solutions of porphyrins [196, 197].

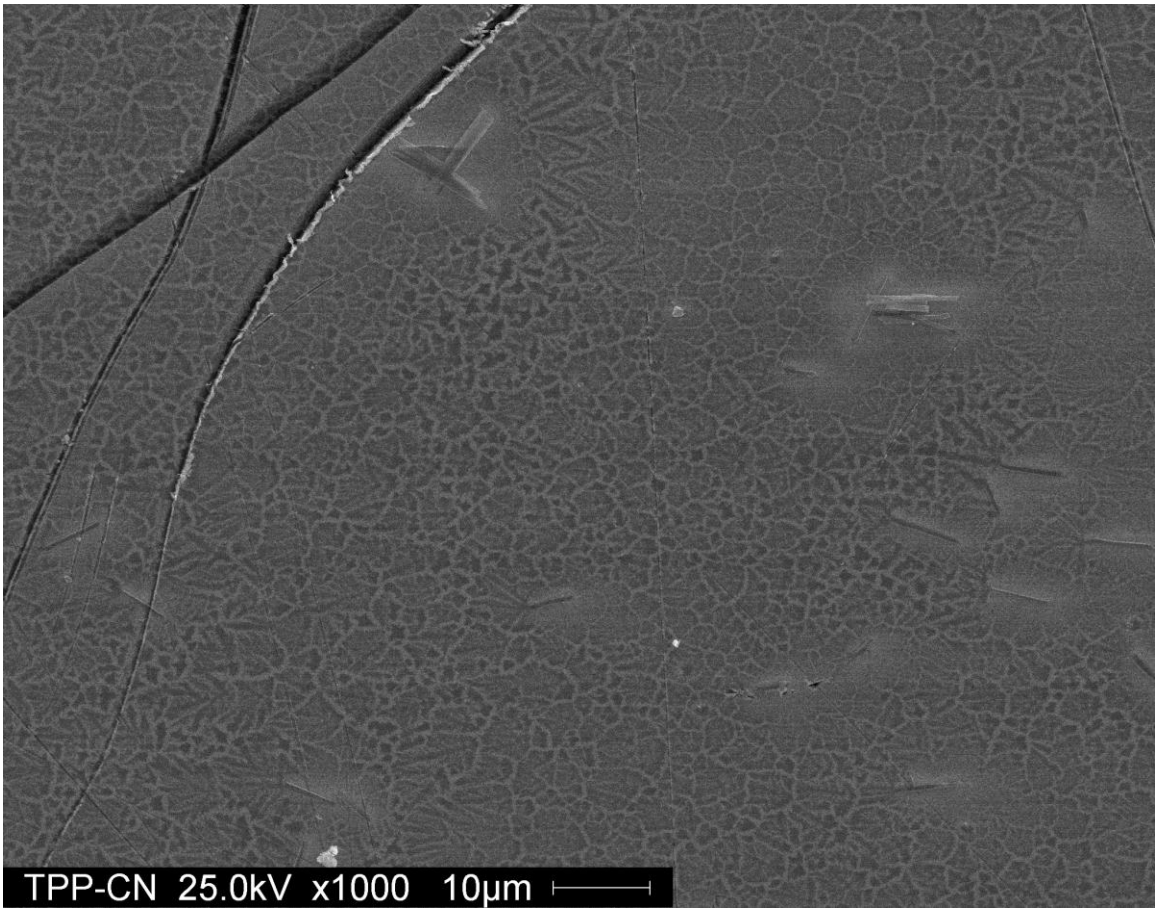

Figure 62: Thin film of TPP-CN on Au with no exposure to $AgNO_3$ (contrast enhanced image).

Figure 63 shows a closer look at the structures that formed in the TPP-CN film on Au. It is evident that the TPP-CN film only consists of islands, which have little to no connections between them. The islands are also rather wide and do not exhibit the fine structure like the TPP-CN/Ag^+ film.

While the SEM images offer an insight into the structure of the formed arrays of TPP-CN molecules, it is difficult to determine the thickness of such a film from these images. To estimate the thickness of the formed TPP-CN structures, $AgNO_3$ and TPP-CN

was deposited on a clean Si surface through drop deposition in the glove box. As mentioned earlier, the hydrophobic and insulating characteristics of Si did not allow for electrospray deposition of $AgNO_3$ and incubation in TPP-CN.

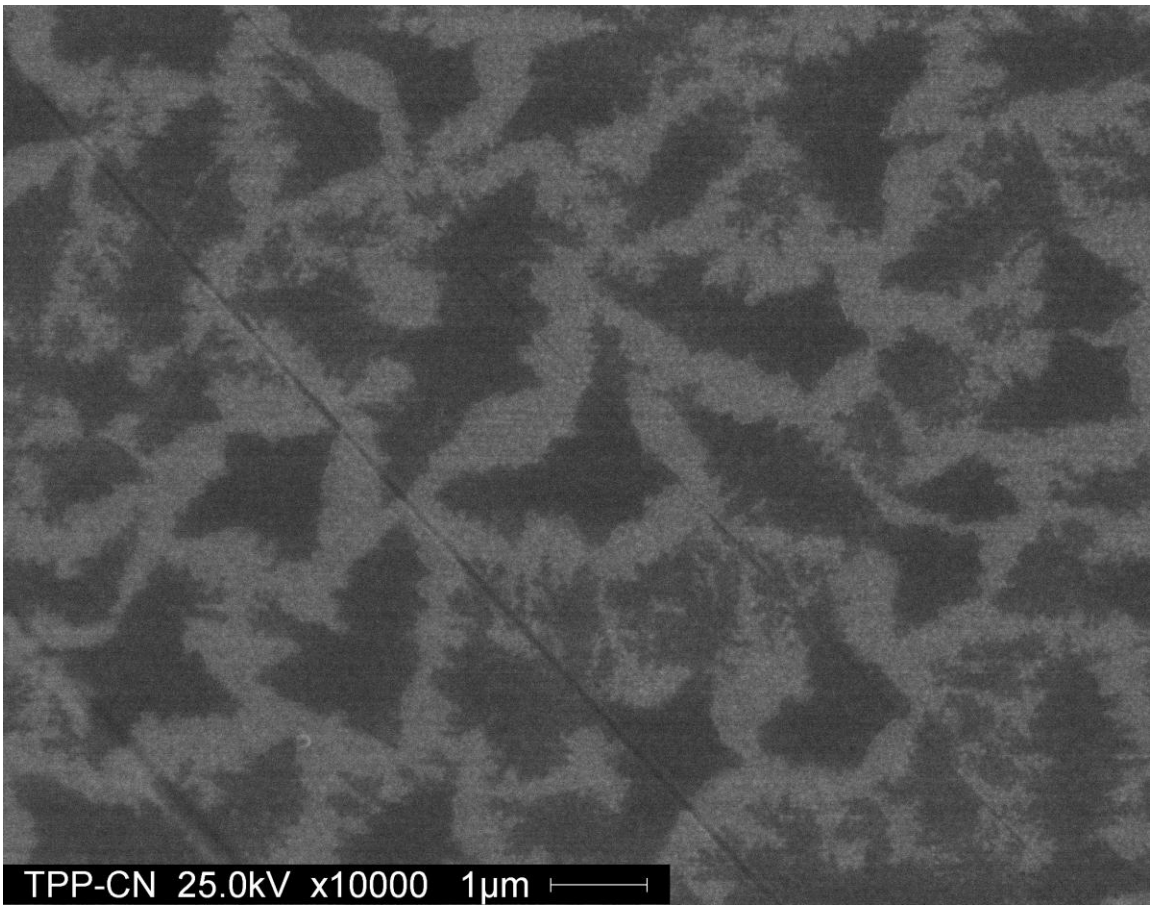

Figure 63: A closer look at the structures formed by TPP-CN on Au (contrast enhanced image).

The smooth surface of the Si sample allowed for surface characterization using an atomic force microscope (AFM). The AFM images obtained for the TPP-CN/Ag^+ film on Si are shown in Figure 64 and Figure 66. The respective height profiles are displayed in Figure 65 and Figure 67.

Figure 64 shows large elongated crystals of TPP-CN molecules that formed on the Si surface after TPP-CN deposition. The Si substrate was predominantly covered with

these crystals and could be likely explained by the hydrophobic characteristics of the Si surface. The use of a hydrophobic substrate may lead to small droplet formation on the surface promoting agglomeration and crystal formation of TPP-CN molecules. Since most likely no interaction takes place between the hydrophobic substrate and the TPP-CN molecules, larger three dimensional structures can therefore be formed.

An assembly of TPP-CN molecules in extended structures, as seen in the SEM images of the TPP-CN/Ag^+ film on Au, likely requires a substrates with hydrophilic characteristics. In that case, the TPP-CN molecules can interact with the surface on a larger scale, as the solvent can spread over a bigger area and allow for the formation of long-range structures.

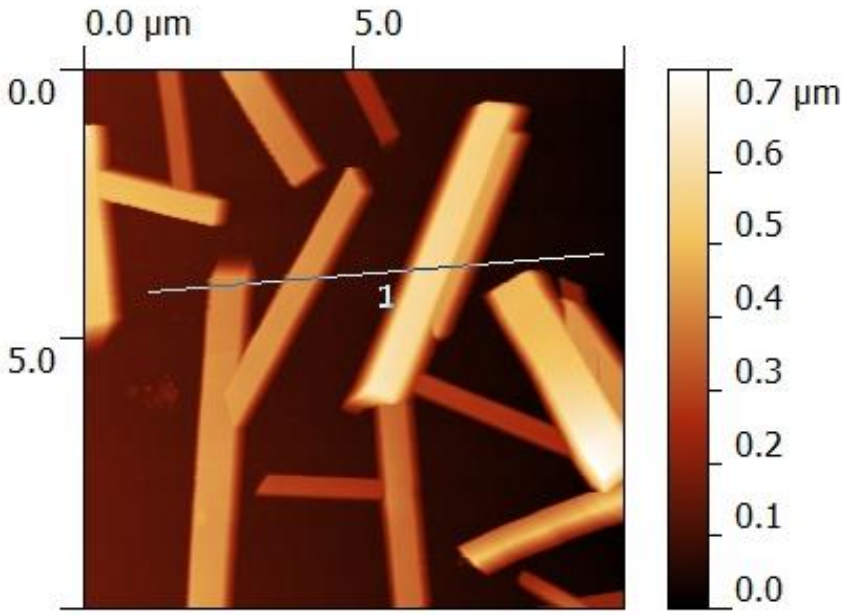

Figure 64: AFM scan of TPP-CN crystals formed on Si

The height profile shown in Figure 65 suggests that the formed crystals are at least 300 nm in height. The deviation from the thickness estimation of approximately 4 nm based on the XPS measurements is mainly due to the fact that the studied crystals

do not represent the surface of a TPP-CN/Ag^+ film on Au. Such crystals were rare in the TPP-CN/Ag^+ film and it predominantly contained arrays of smaller dimensions.

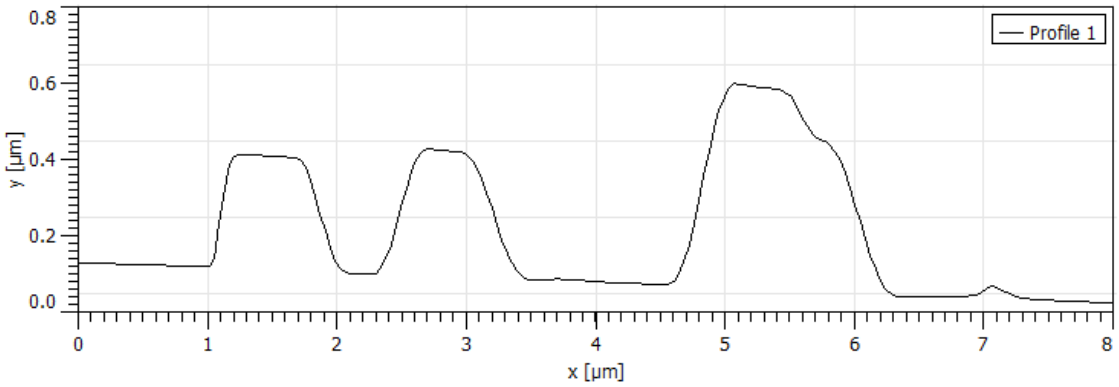

Figure 65: Height profile taken along the line as marked in Figure 64

The Si surface contained a few patches which seemed to consist of structures resembling the structures observed for the TPP-CN/Ag^+ film on Au. The AFM image of such a patch (Figure 66) displays similar branch-like structures, which appear to also have grown coplanar to the sample surface.

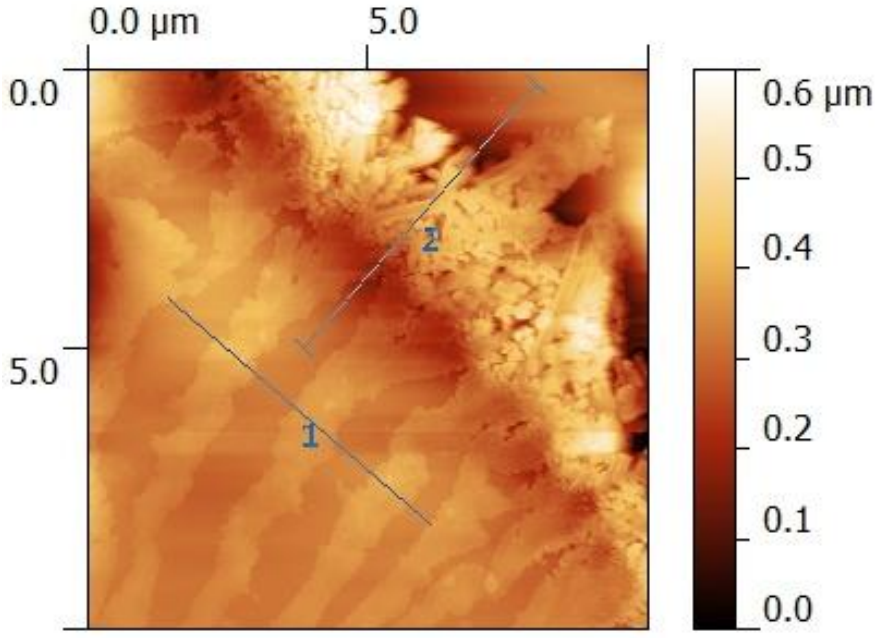

Figure 66: AFM scan of a TPP-CN/Ag^+ array as formed on Si

A height profile scan (see Figure 67) across these branch-like structures revealed heights of 30 nm to 50 nm. Although this value is not in agreement with the thickness from the XPS measurements (4 nm), the XPS based estimation does not take pinholes and other defects into account, which usually leads to an underestimation of the calculated film thickness. The SEM images of the TPP-CN/Ag^+ film demonstrated that the film does indeed contain pinholes and the thickness estimated from the XPS measurements should likely be more than the calculated 4 nm. It is questionable though, that the thickness of the TPP-CN/Ag^+ film may be underestimated by as much as a factor of around 10. However, the XPS measurements were performed on a TPP-CN film deposited on Au, while the AFM images were obtained for a TPP-CN film on Si. It is uncertain how the hydrophobic and hydrophilic characteristics of the two different substrates influence the TPP-CN structure formation. As seen in the AFM pictures, TPP-CN predominantly assembled into large crystals on Si, which could mean that it might also form thicker branches on a Si surface in comparison to an Au surface.

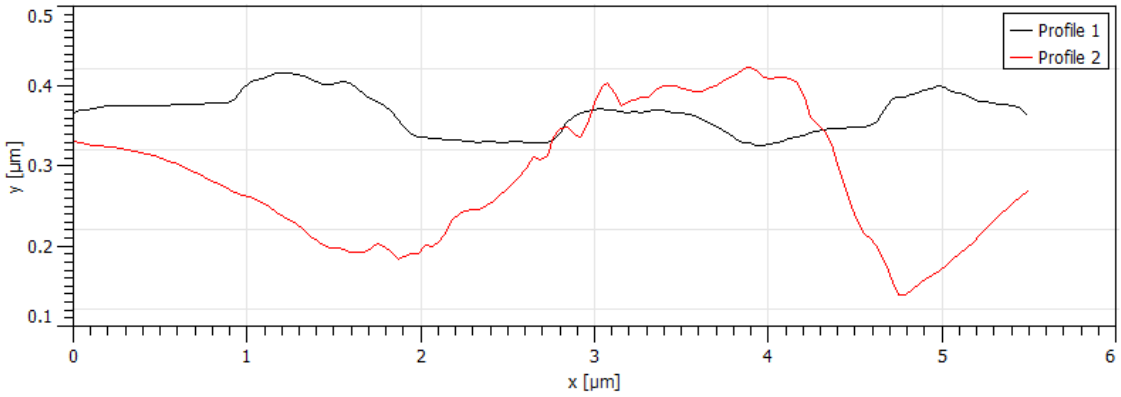

Figure 67: Height profile scan along lines 1 and 2 as seen in Figure 66

5.3.4: Orbital Band Alignment at the Au/TPP-CN and Au/TPP-CN/Ag^+ Interfaces

The detailed analysis by employing XPS, SEM, AFM and XRD suggests that TPP-CN arrays may form on a gold surface induced by the introduction of $AgNO_3$. The study of the electronic structure of the Au/TPP-CN and Au/TPP-CN/Ag^+ interfaces can provide information about the impact of the array formation on the work function and charge injection barriers of the films. The TPP-CN, $AgNO_3$ and TPP-CN/Ag^+ samples were therefore characterized by means of LIXPS and UPS. The full UP-spectra of the TPP-CN, $AgNO_3$, and TPP-CN/Ag^+ films are shown in the center of Figure 68, while the secondary edges are shown on the left and the background removed HOMO emissions are shown on the right.

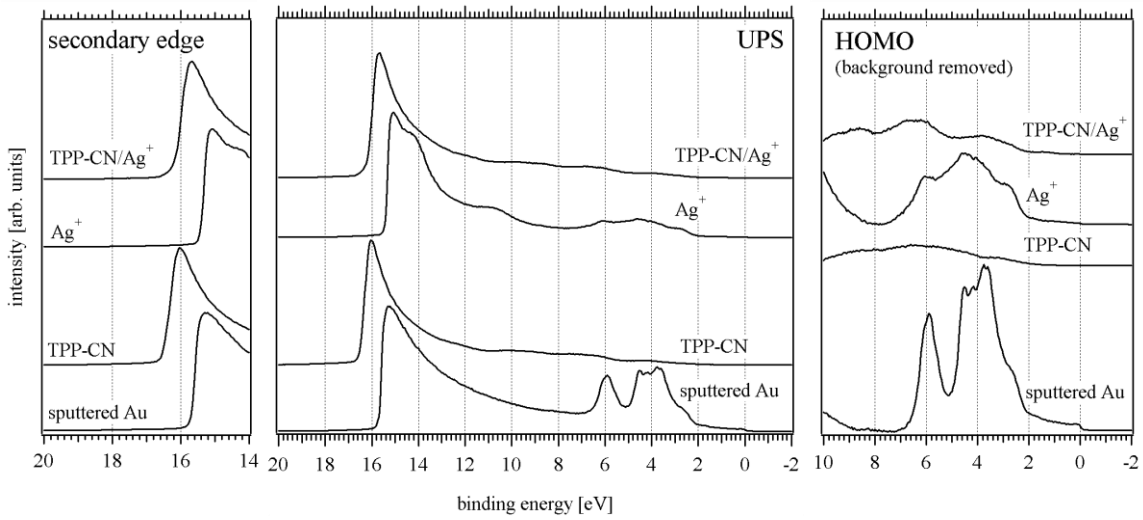

Figure 68: UP-spectrum of adsorbed TPP-CN, $AgNO_3$ deposited on gold (Ag^+), and TPP-CN deposited after exposure of the gold substrate to $AgNO_3$ (TPP-CN/Ag^+).

The measured work function values were 5.42 eV for the clean Au substrate, 4.87 eV for the TPP-CN film, 5.95 eV for the $AgNO_3$ film, and 5.33 eV for the TPP-CN/Ag^+ film. The interface dipole eD of the Au/TPP-CN interface estimated from

the difference between the work functions is with 0.55 eV in close agreement with dipole values obtained for metalloporphyrins deposited on Au [71, 127, 129, 199-201].

The deposition of $AgNO_3$ on the clean Au substrate has the reverse effect on the substrate work function and results in a positive dipole of 0.53 eV. This work function increase can be attributed to the dipole of $AgNO_3$, since the presence of Ag ions and nitric acids may polarize the surface, as was shown for other salts [216]. This dipole can have a big impact on the work function of the substrate and may be one of the reasons for the work function increase. Secondly, the $AgNO_3$ film may contain small clusters of Ag atoms which might have separated from the nitric acid during the electrospray process. Work function measurements of Ag nanoparticles conducted by Schnippering et al. in the past revealed that the work function of nanoparticles increased with decreasing particle size and 4 nm big particles exhibited work functions of 5.51 eV [217]. If small Ag clusters of similar dimensions are present at the sample surface, the measured increase in work function could be attributed to these particles. Since the $AgNO_3$ film is likely a mixture of $AgNO_3$ and Ag clusters, the work function increase may also be a result of both, the dipole of $AgNO_3$ and the specific work function of the Ag particles.

The TPP-CN/Ag^+ film displays a work function of 5.33 eV, which is higher than what was measured for the TPP-CN film. The difference between work functions translates into a dipole of 0.09 eV at the Au/TPP-CN/Ag^+ interface. Such a low value nearly implies vacuum level alignment between the TPP-CN/Ag^+ film and the Au substrate, as it is similar to the energy resolution of the PES system. The low dipole may be explained through the charge transfer between Ag atoms and TPP-CN molecules, which was discussed in section 5.3.2. Charge transfer generally induces a dipole that can

either reduce or increase the work function of the studied sample and such charge induced dipoles were reported in the past for various organic layers [8]. The difference of 0.46 eV between the dipoles of the TPP-CN and TPP-CN/Ag^+ films corresponds with the charge transfer related shifts observed for the N1s and C1s emission peaks.

The background removed HOMO emissions of the TPP-CN and TPP-CN/Ag^+ films, from which the substrate related emission were removed, are shown in Figure 69. Three peaks are commonly expected for TPP derivatives at approximately 1 eV, 3 eV and 6 eV and these peaks are related to the degenerate π orbitals on the porphyrin ring [72, 129, 183, 200, 203], orbitals localized on the phenyl rings [72, 183], and σ orbitals delocalized on the porphyrin ring [71, 72, 201]. While the TPP-CN film displays two apparent peaks at approximately 9 eV and 7 eV, the peaks located at lower energies (approximately 4 eV and 2 eV) are difficult to identify due to artifacts introduced during the removal of the substrate related emissions.

It is obvious that the spectrum of the TPP-CN/Ag+ film is shifted towards lower binding energies in comparison with that of the TPP-CN film. The shift is indicated with dotted lines. This shift is consistent with charge transfer between the Ag atoms and the TPP-CN molecules, as all peaks shift by approximately 0.4 eV, which is in agreement with the observed N1s and C1s peak shifts, as well as the earlier mentioned change of the interface dipole.

While the emission peaks at higher binding energies (9 eV, 7 eV and 4 eV) only exhibit shifts of approximately 0.4 eV, the emission peak located at 2 eV shows a much stronger shift of around 0.8 eV. This shift may be related to the formation of Ag-N bonds due to the interaction of $AgNO_3$ and TPP-CN molecules, which may have caused a larger

shift of the π orbital related emission peak towards lower binding energies. A similar peak location was observed for various metalloporhyrins [183, 199], indicating that the presence of metal-nitrogen bonds is a prerequisite for an emission peak at such low energies.

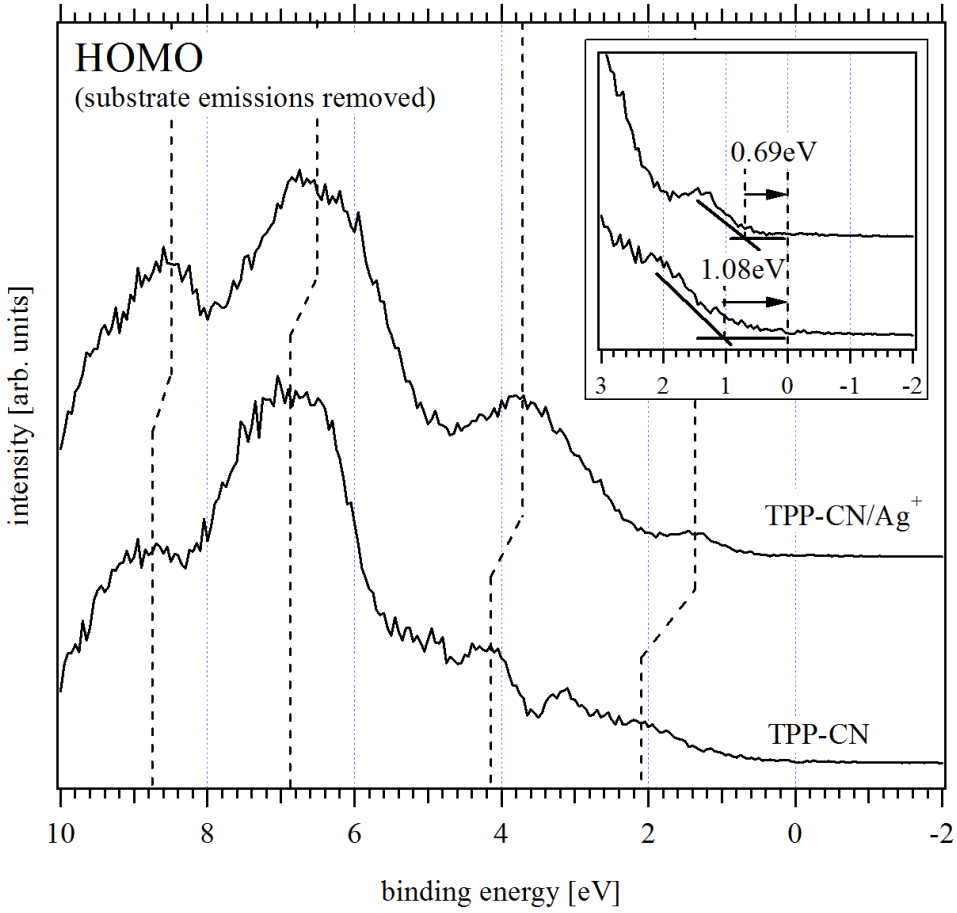

Figure 69: HOMO emission features of the TPP-CN and TPP-CN/Ag^+ film deposited on Au. The substrate emissions were removed from the emission features and the insert shows the HOMO onsets of both films.

In order to determine the hole injection barriers of the Au/TPP-CN and the Au/TPP-CN/Ag^+ interfaces, the position of the HOMO onsets were estimated and are shown in the insert in Figure 69. The hole injection barriers Φ_h were located at 1.08 eV for the TPP-CN film, and 0.69 eV for the TPP-CN/Ag^+ film. The difference of 0.39 eV

corresponds again with the observed charge transfer related shifts of the core level lines of N1s and C1s, and the change in work function.

With the calculated work functions and hole injection barriers of both films, the orbital line-ups can be drawn. The band line-up of the Au/TPP-CN interface is shown in Figure 70, while the band line-up obtained for the Au/TPP-CN/Ag^+ film is displayed in Figure 71.

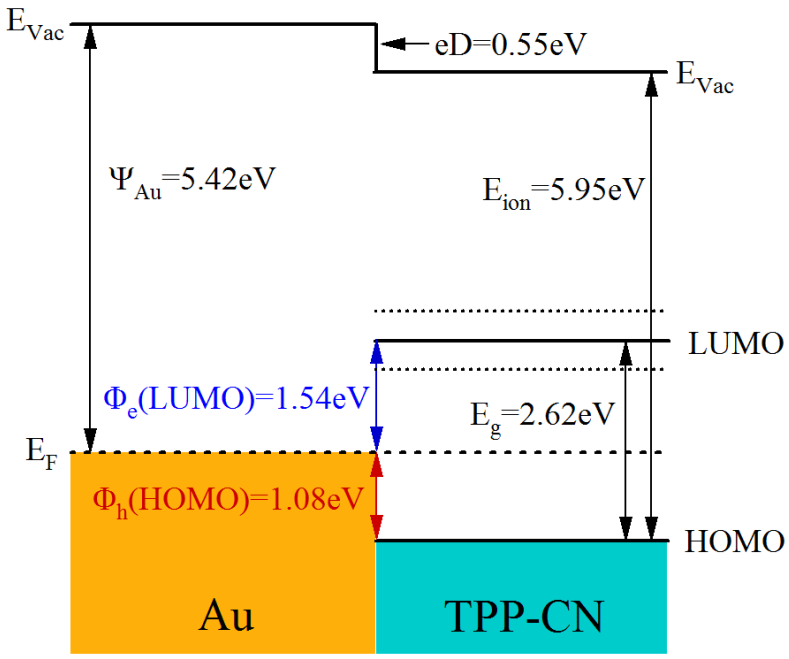

Figure 70: Band line-up at the interface of Au and TPP-CN as determined from the UPS measurements. The dotted lines symbolize the uncertainty of the estimated LUMO level.

In order to estimate the electron injection barriers Φ_e, the hole injection barriers of TPP-CN and TPP-CN/Ag^+ were subtracted from the transfer gap of TPP-CN. As the true transfer gap value of TPP-CN is as of yet unknown, it was approximated by using an average of transfer gap values reported for free base porphyrins and metalloporphyrins, which vary from 2.34 eV to up to 2.9 eV in literature

[204, 205]. The estimated transfer gap of 2.62 ±0.28 eV yielded electron injection barriers of 1.54 ±0.28 eV and 1.93 ±0.28 eV for TPP-CN and TPP-CN/Ag^+, respectively. The ionization energies of both films are in close agreement and show that the metallization of the TPP-CN molecule through the addition of $AgNO_3$ did not result in a significant change of this energy. The values of 5.95 eV and 6.02 eV are higher than ionization energies of around 5.3 eV published for multilayers of ZnTPP and TPP in the past [127, 129, 201]. Since a correlation exists between the ionization energy and the conduction type for porphyrins [201], TPP-CN may be an n-type conductor due to its high ionization energy.

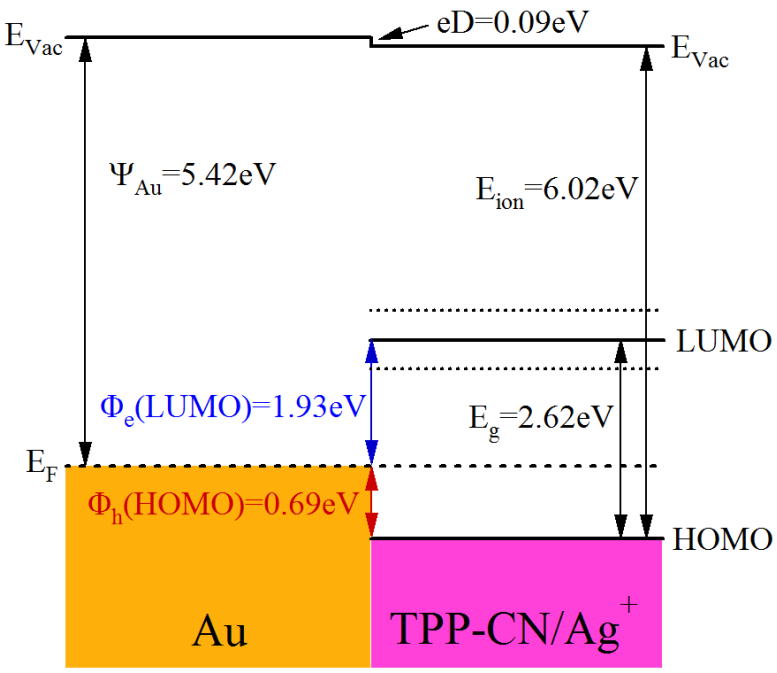

Figure 71: Band line-up as measured at the interface of Au and TPP-CN/Ag^+ with UPS. Just like in the band line-ups for TPP-S and TPP-CN, the dotted lines display the uncertainty of the estimated LUMO level.

Summarizing, the performed experiments suggest that TPP-CN may form structures that contain molecular arrays, if Ag atoms are available for the formation of Coulomb bonds. The presented experiments showed that TPP-CN molecules bond with Ag atoms provided by $AgNO_3$, forming large TPP structures, potentially with long-range connectivity. The resulting film of TPP-CN structures exhibited a lower injection barrier in comparison to a thin film of plainly adsorbed TPP-CN molecules on Au. This barrier may be the result of a charge induced dipole at the Au/TPP-CN/Ag^+ interface.

The structures have potential uses as conductive nano-structures in molecular circuits. The height of the hole injection barrier may still obstruct charge transfer between the TPP-CN structures and the substrate. The PES experiments on TPP-S showed, however, that the incorporation of a thiophenol group into the TPP molecule offers means to bond to the Au surface and create a contact between the substrate and the TPP molecule, reducing the hole injection barrier drastically. The presented approaches of self-assembly (TPP-S) and ionic coordination (TPP-CN) could potentially be used in a wide variety of applications in organic electronics providing a quick and simple way for self-assembled long-range organic networks.

CHAPTER 6: CONCLUSIONS AND OUTLOOK

The work presented in this dissertation demonstrated the successful characterization of the electronic structure of several biomolecular SAMs based on PES measurements. The investigation of self-assembled monolayers of cysteine appended PNA strands of differing nucleobases (adenine and thymine), showed that the nucleobases have a significant impact on the hole injection barriers of the formed SAMs. The height of the determined injection barriers can substantially obstruct the charge transfer through the SAM, but also shows that the right employment of varying nucleobases allows for fine tuning of the hole injection barrier, which can be of great importance for the possible use of PNA strands in organic devices.

The PNA strands were further investigated with regards to the interface of the strands and their ferrocene termini, which are usually used in electrochemistry measurements for charge transfer studies. The experiments showed that the ferrocene terminus significantly lowers the PNA related hole injection barrier at the interface, likely due to a reconfiguration of the molecular orbitals.

The hole injection barriers can not only be affected by the type of nucleobase, but also by the orientation of the PNA molecule at the surface. Incomplete monolayers, which contain flat lying molecules, offer additional means for charge transfer between the substrate and the PNA molecule as the nitrogen sites located in the nucleobases can

lead to an adsorption of the bases onto the Au substrate. The adsorption of PNA molecules through their nucleobases creates new pathways for holes and lower the hole injection barrier noticeably. Such an occurrence could be crucial in the field of organic devices or bimolecular sensors, which employ PNA strands and rely on accurate assessment of the charge injection barriers.

As it was demonstrated in the performed experiments, the charge transfer through a PNA based SAM mostly relies on the nucleobases of the PNA molecule and the cysteine and ferrocene termini are rather stepping stones for the injection and extraction of holes. Therefore, it would be of interest to investigate the two remaining nucleobases (guanine and cytosine) with PES in the future, in order to study their impact on the charge transfer in the PNA SAMs. Furthermore, the variation of the sequence of nucleobases appended to the PNA backbone could potentially identify the grade at which the hole injection barriers could be possibly fine-tuned.

Only PNA strands with 7 segments of N-(2-aminoethyl)glycine units were investigated in this work and the dependency of the electronic structure on the length of the employed PNA strands is as of yet unknown. Hence, the PES based characterization of SAMs containing PNA molecules of various lengths could provide more information on this topic. Furthermore, an investigation of double stranded PNA presents an additional field of study as the interaction of bases can lead to a reconfiguration of the molecular orbitals leading to electronic structures that are different from single stranded PNA.

The study of self-assembled monolayers of tetraphenylporphyrin derivatives containing thiol groups (TPP-S) displayed the easy assembly of monolayers with a rather

small hole injection barrier of 0.39 eV. The formed monolayers could potentially be used as a linker to the metal substrate and provide means for charge transfer due to the low injection barrier. Larger arrays of TPP derivatives or other organic molecules could then be assembled atop the TPP-S monolayer, leading to the design of self-assembled organic circuits and sensor. The potential formation of such TPP based arrays was studied by exposing TPP derivatives with attached nitrogen groups at their peripheries (TPP-CN) to $AgNO_3$. It was shown that the formation of Ag-N bonds resulted in extended TPP structures based on ionic coordination. The structures additionally exhibited a lower hole injection barrier in comparison to adsorbed TPP-CN molecules, due to a charge induced dipole caused by charge transfer across the Ag-N bonds.

The TPP-CN arrays however still exhibited a higher hole injection barrier than the TPP-S monolayer and it would therefore be interesting to investigate the electronic structure of a TPP derivative containing thiol moieties as well as nitrogen groups. Such a TPP derivative would likely allow for the self-assemby of an array with low hole injection barriers towards the Au substrate and charge transfer between neighboring molecules. This approach could be used for the self-assembly of molecular wires, functional arrays or dendrimers used in light-harvesting systems.

The additional study of such arrays by means of inverse photoemission spectroscopy (IPES) and scanning tunneling microscopy (STM) would allow for a detailed analysis of the electronic structure and array quality.

REFERENCES

1. Greenham, N.C. and R.H. Friend, *Semiconductor Device Physics of Conjugated Polymers*, in *Solid State Physics*, E. Henry and S. Frans, Editors. 1996, Academic Press. p. 1-149.

2. Simon, J., et al., *Molecular semiconductors: photoelectrical properties and solar cells*. 1985: Springer-Verlag.

3. Barbe, D.F. and C.R. Westgate, *Surface State Parameters of Metal-Free Phthalocyanine Single Crystals.* Journal of Physics and Chemistry of Solids, 1970. 31(12): p. 2679-&.

4. Ebisawa, F., T. Kurokawa, and S. Nara, *Electrical-Properties of Polyacetylene Polysiloxane Interface.* Journal of Applied Physics, 1983. 54(6): p. 3255-3259.

5. Petrova, M.L. and Rozensht.Ld, *Field Effect in Organic Semiconductor Chloranil.* Soviet Physics Solid State,Ussr, 1970. 12(3): p. 756-&.

6. Koezuka, H., A. Tsumura, and T. Ando, *Field-Effect Transistor with Polythiophene Thin-Film.* Synthetic Metals, 1987. 18(1-3): p. 699-704.

7. Koch, N., et al., *Organic molecular films on gold versus conducting polymer: Influence of injection barrier height and morphology on current-voltage characteristics.* Applied Physics Letters, 2003. 82(14): p. 2281-2283.

8. Ishii, H., et al., *Energy Level Alignment and Interfacial Electronic Structures at Organic/Metal and Organic/Organic Interfaces.* Advanced Materials, 1999. 11(8): p. 605-625.

9. Pullman, A. and B. Pullman, *Molecular electrostatic potential of the nucleic acids.* Quarterly Reviews of Biophysics, 1981. 14(03): p. 289-380.

10. Crispin, X., et al., *Characterization of the Interface Dipole at Organic/ Metal Interfaces.* Journal of the American Chemical Society, 2002. 124(27): p. 8131-8141.

11. Zasadzinski, J., et al., *Langmuir-Blodgett films.* Science, 1994. 263(5154): p. 1726-1733.

12. Bjornholm, T., T. Hassenkam, and N. Reitzel, *Supramolecular organization of highly conducting organic thin films by the Langmuir-Blodgett technique.* Journal of Materials Chemistry, 1999. 9(9): p. 1975-1990.

13. Extrand, C.W., *Spin coating of very thin polymer films.* Polymer Engineering & Science, 1994. 34(5): p. 390-394.

14. Hall, D.B., P. Underhill, and J.M. Torkelson, *Spin coating of thin and ultrathin polymer films.* Polymer Engineering & Science, 1998. 38(12): p. 2039-2045.

15. Scudiero, L., D.E. Barlow, and K.W. Hipps, *Physical Properties and Metal Ion Specific Scanning Tunneling Microscopy Images of Metal(II) Tetraphenylporphyrins Deposited from Vapor onto Gold (111).* The Journal of Physical Chemistry B, 2000. 104(50): p. 11899-11905.

16. Dimitrakopoulos, C.D., A.R. Brown, and A. Pomp, *Molecular beam deposited thin films of pentacene for organic field effect transistor applications.* Journal of Applied Physics, 1996. 80(4): p. 2501-2508.

17. Love, J.C., et al., *Self-assembled monolayers of thiolates on metals as a form of nanotechnology.* Chemical Reviews, 2005. 105(4): p. 1103-1169.

18. Ulman, A., *Formation and structure of self-assembled monolayers.* Chemical Reviews, 1996. 96(4): p. 1533-1554.

19. Mrksich, M. and G.M. Whitesides, *Using self-assembled monolayers to understand the interactions of man-made surfaces with proteins and cells.* Annual Review of Biophysics and Biomolecular Structure, 1996. 25: p. 55-78.

20. Chidsey, C.E.D. and D.N. Loiacono, *Chemical functionality in self-assembled monolayers: structural and electrochemical properties.* Langmuir, 1990. 6(3): p. 682-691.

21. Desiraju, G.R., *Supramolecular Synthons in Crystal Engineering - a New Organic-Synthesis.* Angewandte Chemie-International Edition in English, 1995. 34(21): p. 2311-2327.

22. Atwood, J.L. and J.M. Lehn, *Comprehensive supramolecular chemistry*. 1996: Pergamon.

23. Lehn, J.M., *Supramolecular chemistry: concepts and perspectives : a personal account built upon the George Fisher Baker lectures in chemistry at Cornell University [and the] Lezione Lincee, Accademia nazionale dei Lincei, Roma*. 1995: VCH.

24. Baker, H.R., E.G. Shafrin, and W.A. Zisman, *The Adsorption of Hydrophobic Monolayers of Carboxylic Acids.* Journal of Physical Chemistry, 1952. 56(3): p. 405-412.

25. Levine, O. and W.A. Zisman, *Physical Properties of Monolayers Adsorbed at the Solid-Air Interface .1. Friction and Wettability of Aliphatic Polar Compounds and Effect of Halogenation.* Journal of Physical Chemistry, 1957. 61(8): p. 1068-1077.

26. Bigelow, W.C., D.L. Pickett, and W.A. Zisman, *Oleophobic Monolayers .1. Films Adsorbed from Solution in Non-Polar Liquids.* Journal of Colloid Science, 1946. 1(6): p. 513-538.

27. Sagiv, J., *Organized Monolayers by Adsorption .1. Formation and Structure of Oleophobic Mixed Monolayers on Solid-Surfaces.* Journal of the American Chemical Society, 1980. 102(1): p. 92-98.

28. Netzer, L., R. Iscovici, and J. Sagiv, *Adsorbed Monolayers Versus Langmuir-Blodgett Monolayers Why and How .1. From Monolayer to Multilayer, by Adsorption.* Thin Solid Films, 1983. 99(1-3): p. 235-241.

29. Nuzzo, R.G. and D.L. Allara, *Adsorption of Bifunctional Organic Disulfides on Gold Surfaces.* Journal of the American Chemical Society, 1983. 105(13): p. 4481-4483.

30. Bain, C.D., et al., *Formation of monolayer films by the spontaneous assembly of organic thiols from solution onto gold.* Journal of the American Chemical Society, 1989. 111(1): p. 321-335.

31. Ulman, A., *An introduction to ultrathin organic films: from Langmuir-Blodgett to self-assembly*. 1991: Academic Press.

32. Dubois, L.H. and R.G. Nuzzo, *Synthesis, Structure, and Properties of Model Organic-Surfaces.* Annual Review of Physical Chemistry, 1992. 43: p. 437-463.

33. Nuzzo, R.G., B.R. Zegarski, and L.H. Dubois, *Fundamental-Studies of the Chemisorption of Organosulfur Compounds on Au(111) - Implications for Molecular Self-Assembly on Gold Surfaces.* Journal of the American Chemical Society, 1987. 109(3): p. 733-740.

34. Nuzzo, R.G., F.A. Fusco, and D.L. Allara, *Spontaneously Organized Molecular Assemblies .3. Preparation and Properties of Solution Adsorbed Monolayers of Organic Disulfides on Gold Surfaces.* Journal of the American Chemical Society, 1987. 109(8): p. 2358-2368.

35. Chesters, M.A. and G.A. Somorjai, *Chemisorption of Oxygen, Water and Selected Hydrocarbons on (111) and Stepped Gold Surfaces.* Surface Science, 1975. 52(1): p. 21-28.

36. Fenter, P., A. Eberhardt, and P. Eisenberger, *Self-Assembly of N-Alkyl Thiols as Disulfides on Au(111).* Science, 1994. 266(5188): p. 1216-1218.

37. Dubois, L.H., B.R. Zegarski, and R.G. Nuzzo, *Molecular Ordering of Organosulfur Compounds on Au(111) and Au(100) - Adsorption from Solution and in Ultrahigh-Vacuum.* Journal of Chemical Physics, 1993. 98(1): p. 678-688.

38. Biebuyck, H.A., C.D. Bian, and G.M. Whitesides, *Comparison of Organic Monolayers on Polycrystalline Gold Spontaneously Assembled from Solutions Containing Dialkyl Disulfides or Alkenethiols.* Langmuir, 1994. 10(6): p. 1825-1831.

39. Porter, M.D., et al., *Spontaneously Organized Molecular Assemblies .4. Structural Characterization of Normal-Alkyl Thiol Monolayers on Gold by Optical Ellipsometry, Infrared-Spectroscopy, and Electrochemistry.* Journal of the American Chemical Society, 1987. 109(12): p. 3559-3568.

40. Holmesfarley, S.R., C.D. Bain, and G.M. Whitesides, *Wetting of Functionalized Polyethylene Film Having Ionizable Organic-Acids and Bases at the Polymer Water Interface - Relations between Functional-Group Polarity, Extent of Ionization, and Contact-Angle with Water.* Langmuir, 1988. 4(4): p. 921-937.

41. Bain, C.D., J. Evall, and G.M. Whitesides, *Formation of Monolayers by the Coadsorption of Thiols on Gold - Variation in the Head Group, Tail Group, and Solvent.* Journal of the American Chemical Society, 1989. 111(18): p. 7155-7164.

42. Strong, L. and G.M. Whitesides, *Structures of Self-Assembled Monolayer Films of Organosulfur Compounds Adsorbed on Gold Single-Crystals - Electron-Diffraction Studies.* Langmuir, 1988. 4(3): p. 546-558.

43. Nishida, N., et al., *Thermal desorption spectroscopy of alkanethiol self-assembled monolayer on Au(111).* Japanese Journal of Applied Physics Part 1-Regular Papers Short Notes & Review Papers, 1996. 35(11): p. 5866-5872.

44. Nishida, N., et al., *Dimerization process in alkanethiol self-assembled monolayer on Au(111).* Japanese Journal of Applied Physics Part 2-Letters, 1996. 35(6B): p. L799-L802.

45. Hashimoto, K., K. Ito, and Y. Ishimori, *Novel DNA Sensor for Electrochemical Gene Detection.* Analytica Chimica Acta, 1994. 286(2): p. 219-224.

46. Tang, X.W., et al., *Carbon nanotube DNA sensor and sensing mechanism.* Nano Letters, 2006. 6(8): p. 1632-1636.

47. Vo-Dinh, T., et al., *DNA biochip using a phototransistor integrated circuit.* Analytical Chemistry, 1999. 71(2): p. 358-363.

48. Zheng, L.F., J.P. Brody, and P.J. Burke, *Electronic manipulation of DNA, proteins, and nanoparticles for potential circuit assembly.* Biosensors & Bioelectronics, 2004. 20(3): p. 606-619.

49. Lakin, M.R., et al., *Abstractions for DNA circuit design.* Journal of The Royal Society Interface, 2012. 9(68): p. 470-486.

50. Hyrup, B. and P.E. Nielsen, *Peptide nucleic acids (PNA): synthesis, properties and potential applications.* Bioorg Med Chem, 1996. 4(1): p. 5-23.

51. Dizdaroglu, M., *Chemical determination of free radical-induced damage to DNA.* Free Radical Biology and Medicine, 1991. 10(3–4): p. 225-242.

52. Richter, C., J.W. Park, and B.N. Ames, *Normal oxidative damage to mitochondrial and nuclear DNA is extensive.* Proceedings of the National Academy of Sciences, 1988. 85(17): p. 6465-6467.

53. Nielsen, P., et al., *Sequence-selective recognition of DNA by strand displacement with a thymine-substituted polyamide.* Science, 1991. 254(5037): p. 1497-1500.

54. Larsen, H.J., T. Bentin, and P.E. Nielsen, *Antisense properties of peptide nucleic acid.* Biochimica Et Biophysica Acta-Gene Structure and Expression, 1999. 1489(1): p. 159-166.

55. Braasch, D.A. and D.R. Corey, *Novel antisense and peptide nucleic acid strategies for controlling gene expression.* Biochemistry, 2002. 41(14): p. 4503-4510.

56. Lohse, J., O. Dahl, and P.E. Nielsen, *Double duplex invasion by peptide nucleic acid: A general principle for sequence-specific targeting of double-stranded DNA.* Proceedings of the National Academy of Sciences of the United States of America, 1999. 96(21): p. 11804-11808.

57. Egholm, M., et al., *Pna Hybridizes to Complementary Oligonucleotides Obeying the Watson-Crick Hydrogen-Bonding Rules.* Nature, 1993. 365(6446): p. 566-568.

58. Wittung, P., et al., *DNA-Like Double Helix Formed by Peptide Nucleic-Acid.* Nature, 1994. 368(6471): p. 561-563.

59. Paul, A., et al., *Role of Nucleobase Energetics and Nucleobase Interactions in Single-Stranded Peptide Nucleic Acid Charge Transfer.* Journal of the American Chemical Society, 2009. 131(18): p. 6498-6507.

60. Paul, A., et al., *Charge transfer through single-stranded peptide nucleic acid composed of thymine Nucleotides.* Journal of Physical Chemistry C, 2008. 112(18): p. 7233-7240.

61. Venkatramani, R., et al., *Evidence for a Near-Resonant Charge Transfer Mechanism for Double-Stranded Peptide Nucleic Acid.* Journal of the American Chemical Society, 2011. 133(1): p. 62-72.

62. Geier, G.R., D.M. Haynes, and J.S. Lindsey, *An Efficient One-Flask Synthesis of N-Confused Tetraphenylporphyrin.* Organic Letters, 1999. 1(9): p. 1455-1458.

63. Lucas, R., et al., *A facile and rapid iodine-catalyzed meso-tetraphenylporphyrin synthesis using microwave activation.* Tetrahedron Letters, 2008. 49(38): p. 5537-5539.

64. Gonsalves, A.M.D.A.R. and M.M. Pereira, *A new look into the rothemund meso-tetraalkyl and tetraarylporphyrin synthesis.* Journal of Heterocyclic Chemistry, 1985. 22(3): p. 931-933.

65. Kuster, W., *Information on bilirubine and haemine.* Hoppe-Seylers Zeitschrift Fur Physiologische Chemie, 1912. 82(6): p. 463-483.

66. Fischer, H. and K. Zeile, *Synthesis of the hamatoporphyrine protoporphyrin and hamin.* Justus Liebigs Annalen Der Chemie, 1929. 468: p. 98-116.

67. Yamashita, K., Y. Harima, and T. Matsubayashi, *Conductance Control of Porphyrin Solids by Molecular Design and Doping.* Journal of Physical Chemistry, 1989. 93(13): p. 5311-5315.

68. Smith, K.M.K.R.G.K.M., *Biochemistry and Binding, Activation of Small Molecules*. 2000: Elsevier.

69. Takulapalli, B.R., et al., *Electrical detection of amine ligation to a metalloporphyrin via a hybrid SOI-MOSFET.* Journal of the American Chemical Society, 2008. 130(7): p. 2226-2233.

70. Schmidt-Mende, L., et al., *Zn-porphyrin-sensitized nanocrystalline TiO2 heterojunction photovoltaic cells.* Chemphyschem, 2005. 6(7): p. 1253-1258.

71. Lukasczyk, T., et al., *Interaction of cobalt(II) tetraarylporphyrins with a Ag(111) surface studied with photoelectron spectroscopy.* Journal of Physical Chemistry C, 2007. 111(7): p. 3090-3098.

72. Scudiero, L., et al., *Scanning tunneling microscopy, orbital-mediated tunneling spectroscopy, and ultraviolet photoelectron spectroscopy of metal(II) tetraphenylporphyrins deposited from vapor.* Journal of the American Chemical Society, 2001. 123(17): p. 4073-4080.

73. Buchner, F., et al., *Coordination of iron atoms by tetraphenylporphyrin monolayers and multilayers on Ag(111) and formation of iron-tetraphenylporphyrin.* Journal of Physical Chemistry C, 2008. 112(39): p. 15458-15465.

74. Imahori, H., et al., *Chain length effect on photocurrent from polymethylene-linked porphyrins in self-assembled monolayers.* Langmuir, 1998. 14(19): p. 5335-5338.

75. Akiyama, T., H. Imahori, and Y. Sakata, *Preparation of Molecular Assemblies of Porphyrin-Linked Alkanethiol on Gold Surface and Their Redox Properties.* Chemistry Letters, 1994(8): p. 1447-1450.

76. Shimazu, K., et al., *Formation and characterization of thiol-derivatized zinc(II) porphyrin monolayers on gold.* Thin Solid Films, 1996. 273(1-2): p. 250-253.

77. Akiyama, T., et al., *Synthesis and self-assembly of porphyrin-linked fullerene on gold surface using S-Au linkage.* Chemistry Letters, 1996(10): p. 907-908.

78. Kondo, T., et al., *Photoelectrochemical characteristics of a self-assembled monolayer of porphyrin-mercaptoquinone coupling molecules.* Thin Solid Films, 1996. 284: p. 652-655.

79. Uosaki, K., et al., *Very efficient visible-light-induced uphill electron transfer at a self-assembled monolayer with a porphyrin-ferrocene-thiol linked molecule.* Journal of the American Chemical Society, 1997. 119(35): p. 8367-8368.

80. Boeckl, M.S., et al., *Self-assembly of tetraphenylporphyrin monolayers on gold substrates.* Langmuir, 2000. 16(13): p. 5644-5653.

81. Bramblett, A.L., et al., *Determination of surface coverage for tetraphenylporphyrin monolayers using ultraviolet visible absorption and x-ray photoelectron spectroscopies.* Surface and Interface Analysis, 2002. 33(6): p. 506-515.

82. Hutchison, J.E., T.A. Postlethwaite, and R.W. Murray, *Molecular Films of Thiol-Derivatized Tetraphenylporphyrins on Gold - Film Formation and Electrocatalytic Dioxygen Reduction.* Langmuir, 1993. 9(11): p. 3277-3283.

83. Imahori, H., et al., *Concentration effects of porphyrin monolayers on the structure and photoelectrochemical properties of mixed self-assembled monolayers of porphyrin and alkanethiol on gold electrodes.* Langmuir, 2001. 17(16): p. 4925-4931.

84. Imahori, H., et al., *Chain length effect on the structure and photoelectrochemical properties of self-assembled monolayers of porphyrins on gold electrodes.* Journal of Physical Chemistry B, 2000. 104(6): p. 1253-1260.

85. Rawlett, A.M., et al., *A molecular electronics toolbox.* Nanotechnology, 2003. 14(3): p. 377-384.

86. Roth, K.M., et al., *Comparison of electron-transfer and charge-retention characteristics of porphyrin-containing self-assembled monolayers designed for molecular information storage.* Journal of Physical Chemistry B, 2002. 106(34): p. 8639-8648.

87. Yasseri, A.A., et al., *Characterization of self-assembled monolayers of porphyrins bearing multiple thiol-derivatized rigid-rod tethers.* Journal of the American Chemical Society, 2004. 126(38): p. 11944-11953.

88. Zak, J., et al., *Thiol-Derivatized Metalloporphyrins - Monomolecular Films for the Electrocatalytic Reduction of Dioxygen at Gold Electrodes.* Langmuir, 1993. 9(11): p. 2772-2774.

89. Wang, Z.C., C.J. Medforth, and J.A. Shelnutt, *Porphyrin nanotubes by ionic self-assembly.* Journal of the American Chemical Society, 2004. 126(49): p. 15954-15955.

90. Faul, C.F.J. and M. Antonietti, *Ionic Self-Assembly: Facile Synthesis of Supramolecular Materials.* Advanced Materials, 2003. 15(9): p. 673-683.

91. Tomalia, D.A., et al., *A New Class of Polymers - Starburst-Dendritic Macromolecules.* Polymer Journal, 1985. 17(1): p. 117-132.

92. Newkome, G.R., et al., *Supramolecular chemistry of flexible, dendritic-based structures employing molecular recognition.* Chemical Communications, 1996(24): p. 2737-2738.

93. Deisenhofer, J. and J.R. Norris, *The Photosynthetic reaction center*. 1993: Academic Press.

94. Blankenship, R.E., M.T. Madigan, and C.E. Bauer, *Anoxygenic photosynthetic bacteria*. 1995: Kluwer Academic Publishers.

95. Prathapan, S., T.E. Johnson, and J.S. Lindsey, *Building-Block Synthesis of Porphyrin Light-Harvesting Arrays.* Journal of the American Chemical Society, 1993. 115(16): p. 7519-7520.

96. Li, J.Z., et al., *Template-directed synthesis, excited-state photodynamics, and electronic communication in a hexameric wheel of porphyrins.* Journal of the American Chemical Society, 1999. 121(38): p. 8927-8940.

97. Maruyama, K. and A. Osuka, *A Chemical Approach toward Photosynthetic Reaction Center.* Pure and Applied Chemistry, 1990. 62(8): p. 1511-1520.

98. Aratani, N. and A. Osuka, *A new strategy for construction of covalently linked giant porphyrin arrays with one, two, and three dimensionally arranged architectures.* Bulletin of the Chemical Society of Japan, 2001. 74(8): p. 1361-1379.

99. Choi, M.S., et al., *A large dendritic multiporphyrin array as a mimic of the bacterial light-harvesting antenna complex: Molecular design of an efficient energy funnel for visible photons.* Angewandte Chemie-International Edition, 2001. 40(17): p. 3194-+.

100. Imahori, H., et al., *Photoactive three-dimensional monolayers: Porphyrin-alkanethiolate-stabilized gold clusters.* Journal of the American Chemical Society, 2001. 123(2): p. 335-336.

101. Hahner, G., et al., *Investigation of Intermediate Steps in the Self-Assembly of N-Alkanethiols on Gold Surfaces by Soft-X-Ray Spectroscopy.* Langmuir, 1993. 9(8): p. 1955-1958.

102. Rouhana, L.L., M.D. Moussallem, and J.B. Schlenoff, *Adsorption of Short-Chain Thiols and Disulfides onto Gold under Defined Mass Transport Conditions: Coverage, Kinetics, and Mechanism.* Journal of the American Chemical Society, 2011. 133(40): p. 16080-16091.

103. Cole, R.B., *Electrospray ionization mass spectrometry: fundamentals, instrumentation, and applications*. 1997: Wiley.

104. Cascio, A.J., et al., *Investigation of a Polythiophene Interface Using Photoemission Spectroscopy in Combination with Electrospray Thin Film Deposition.* Applied Physics Letters, 2006. 88: p. Art.No.: 062104.

105. Lagel, B., et al., *Investigation of the poly[2-methoxy-5-(2 '-ethyl-hexyloxy)-1,4-phenylene vinylene]/indium tin oxide interface using photoemission spectroscopy.* Journal of Applied Physics, 2005. 98(2).

106. Lyon, J.E., et al., *Photoemission study of the poly(3-hexylthiophene)/Au interface.* Applied Physics Letters, 2006. 88(22).

107. Magulick, J., et al., *Ionization energy and electronic structure of polycytidine.* Journal of Physical Chemistry B, 2006. 110: p. 2692-2699.

108. Morozov, V.N. and T.Y. Morozova, *Electrospray deposition as a method to fabricate functionally active protein films.* Analytical Chemistry, 1999. 71(7): p. 1415-1420.

109. Tani, Y., S. Kobayashi, and H. Kawazoe, *Characterization of electrospray ion-beam-deposited CdSe/ZnS quantum dot thin films from a colloidal solution.* Journal of Vacuum Science & Technology A, 2008. 26(4): p. 1058-1061.

110. Tani, Y., S. Kobayashi, and H. Kawazoe, *Ion beam deposition of quantum dots from colloidal solution.* Japanese Journal of Applied Physics, 2008. 47(4): p. 2977-2981.

111. Jayasinghe, S.N., *Biojets in regenerative biology & medicine.* Materials Today, 2011. 14(5): p. 202-211.

112. Ertl, G. and J. Küppers, *Low energy electrons and surface chemistry*. 1985: VCH.

113. Taylor, G., *Disintegration of Water Drops in Electric Field.* Proceedings of the Royal Society of London Series a-Mathematical and Physical Sciences, 1964. 280(1380): p. 383-+.

114. Hertz, H., *Ueber einen Einfluss des ultravioletten Lichtes auf die electrische Entladung.* Annalen Der Physik, 1887. 267(8): p. 983-1000.

115. Lenard, P., *The light electrical effect.* Annalen Der Physik, 1902. 8(5): p. 149-198.

116. Thomson, J.J., *On the Masses of the Ions in Gases at Low Pressures.* Philosophical Magazine, 1899. 48(295): p. 547-567.

117. Einstein, A., *Generation and conversion of light with regard to a heuristic point of view.* Annalen Der Physik, 1905. 17(6): p. 132-148.

118. Nordling, C., E. Sokolowski, and K. Siegbahn, *Precision Method for Obtaining Absolute Values of Atomic Binding Energies.* Physical Review, 1957. 105(5): p. 1676-1677.

119. Nordling, C. and K. Siegbahn, *A New Precision Spectroscopy of Atoms and Molecules.* Revue Roumaine De Physique, 1966. 11(9-10): p. 797-&.

120. Siegbahn, K. and C. Nordling, *A New High-Precision Instrument for Electron and Nuclear Spectroscopy.* Arkiv for Fysik, 1962. 22(5): p. 436-436.

121. Fahlman, A., et al., *An Apparatus for Esca Method.* Arkiv for Fysik, 1966. 31(6): p. 479-&.

122. Fahlman, A. and K. Siegbahn, *Esca Method Using Monochromatic X-Rays and a Permanent Magnet Spectrograph.* Arkiv for Fysik, 1966. 32(2-3): p. 111-&.

123. Lüth, H., *Solid Surfaces, Interfaces and Thin Films*. 2010: Springer.

124. Hufner, S., *Photoelectron Spectroscopy: Principles and Applications*. 2003: Springer.

125. Schlaf, R., H. Murata, and Z.H. Kafafi, *Work function measurements on indium tin oxide films.* Journal of Electron Spectroscopy and Related Phenomena, 2001. 120(1-3): p. 149-154.

126. Beerbom, M.M., et al., *Direct comparison of photoemission spectroscopy and in situ Kelvin probe work function measurements on indium tin oxide films.* Journal of Electron Spectroscopy and Related Phenomena, 2006. 152(1-2): p. 12-17.

127. Narioka, S., et al., *The Electronic-Structure and Energy-Level Alignment of Porphyrin/Metal Interfaces Studied by Ultraviolet Photoelectron-Spectroscopy.* Applied Physics Letters, 1995. 67(13): p. 1899-1901.

128. Seki, K., E. Ito, and H. Ishii, *Energy level alignment at organic/metal interfaces studied by UV photoemission.* Synthetic Metals, 1997. 91: p. 137-142.

129. Yoshimura, D., et al., *The electronic structure of porphyrin/metal interfaces studied by ultraviolet photoelectron spectroscopy.* Journal of Electron Spectroscopy and Related Phenomena, 1996. 78: p. 359-362.

130. Seki, K., et al., *Uv Photoemission-Study of Dye/Agbr Interfaces in Relation to Spectral Sensitization.* Physical Review B, 1994. 49(4): p. 2760-2767.

131. Peisert, H., et al., *Fluorination of copper phthalocyanines: Electronic structure and interface properties.* Journal of Applied Physics, 2003. 93(12): p. 9683-9692.

132. Knupfer, M. and G. Paasch, *Origin of the interface dipole at interfaces between undoped organic semiconductors and metals.* Journal of Vacuum Science & Technology A, 2005. 23(4): p. 1072-1077.

133. Crispin, X., et al., *Characterization of the interface dipole at organic/metal interfaces.* Journal of the American Chemical Society, 2002. 124(27): p. 8131-8141.

134. Lindell, L., et al., *Characterization of the interface dipole at the paraphenylenediamine-nickel interface: A joint theoretical and experimental study.* Journal of Chemical Physics, 2005. 122(8).

135. Lang, N.D., *Interaction between Closed-Shell Systems and Metal-Surfaces.* Physical Review Letters, 1981. 46(13): p. 842-845.

136. Alkauskas, A., et al., *Energy level alignment at metal-octaethylporphyrin interfaces.* Journal of Physical Chemistry B, 2005. 109(49): p. 23558-23563.

137. Zangwill, A., *Physics at Surfaces*. 1988: Cambridge University Press.

138. Holloway, S., et al., *Handbook of surface science: Electronic structure*. 2000: Elsevier.

139. Chen, Y.C., J.E. Cunningham, and C.P. Flynn, *Dependence of Rare-Gas-Adsorbate Dipole-Moment on Substrate Work Function.* Physical Review B, 1984. 30(12): p. 7317-7319.

140. Da Silva, J.L.F., C. Stampfl, and M. Scheffler, *Adsorption of Xe atoms on metal surfaces: New insights from first-principles calculations.* Physical Review Letters, 2003. 90(6).

141. Morikawa, Y., H. Ishii, and K. Seki, *Theoretical study of n-alkane adsorption on metal surfaces.* Physical Review B, 2004. 69(4).

142. Hirose, Y., et al., *Chemistry and electronic properties of metal-organic semiconductor interfaces: Al, Ti, In, Sn, Ag, and Au on PTCDA.* Physical Review B, 1996. 54(19): p. 13748-13758.

143. Wolak, M.A., et al., *Electronic Structure of Self-Assembled Peptide Nucleic Acid Thin Films.* Journal of Physical Chemistry C, 2011. 115(34): p. 17123-17135.

144. Kojima, I. and M. Kurahashi, *APPLICATION OF ASYMMETRICAL GAUSSIAN LORENTZIAN MIXED-FUNCTION FOR X-RAY PHOTOELECTRON CURVE SYNTHESIS.* Journal of Electron Spectroscopy and Related Phenomena, 1987. 42(2): p. 177-181.

145. Scofield, J.H., *Hartree-Slater Subshell Photoionization Cross-Sections at 1254 and 1487ev.* Journal of Electron Spectroscopy and Related Phenomena, 1976. 8(2): p. 129-137.

146. Paul, A., et al., *Distance Dependence of the Charge Transfer Rate for Peptide Nucleic Acid Monolayers†.* The Journal of Physical Chemistry B, 2009. 114(45): p. 14140-14148.

147. Beerbom, M.M., R. Gargagliano, and R. Schlaf, *Determination of the electronic structure of self-assembled L-cysteine/Au interfaces using photoemission spectroscopy.* Langmuir, 2005. 21(8): p. 3551-3558.

148. Magulick, J., M.M. Beerbom, and R. Schlaf, *Comparison of ribonucleic acid homopolymer ionization energies and charge injection barriers.* Journal of Physical Chemistry B, 2006. 110: p. 15973-15981.

149. Magulick, J., M.M. Beerbom, and R. Schlaf, *Investigation of Adenine, Uracil, and Ribose Phosphate Thin Films Prepared by Electrospray In-Vacuum Deposition Using Photoemission Spectroscopy.* Thin Solid Films, 2008. 516(9): p. 2396-2400.

150. Stańczyk, K., et al., *Transformation of nitrogen structures in carbonization of model compounds determined by XPS.* Carbon, 1995. 33(10): p. 1383-1392.

151. Pels, J.R., et al., *Evolution of nitrogen functionalities in carbonaceous materials during pyrolysis.* Carbon, 1995. 33(11): p. 1641-1653.

152. Mateo-Marti, E., et al., *A DNA biosensor based on peptide nucleic acids on gold surfaces.* Biosensors & Bioelectronics, 2007. 22(9-10): p. 1926-1932.

153. Malitesta, C., et al., *Applicability of chemical derivatization – X-ray photoelectron spectroscopy (CD–XPS) to the characterization of complex matrices: case of electrosynthesized polypyrroles.* Journal of Electron Spectroscopy and Related Phenomena, 1998. 97(3): p. 199-208.

154. Malitesta, C., et al., *New findings on polypyrrole chemical structure by XPS coupled to chemical derivatization labelling.* Journal of Electron Spectroscopy and Related Phenomena, 1995. 76(0): p. 629-634.

155. Fisher, G.B. and J.L. Gland, *The Interaction of Water with the Pt(111) Surface.* Surface Science, 1980. 94: p. 446-455.

156. Laibinis, P.E., C.D. Bain, and G.M. Whitesides, *ATTENUATION OF PHOTOELECTRONS IN MONOLAYERS OF NORMAL-ALKANETHIOLS ADSORBED ON COPPER, SILVER, AND GOLD.* Journal of Physical Chemistry, 1991. 95(18): p. 7017-7021.

157. Mateo-Marti, E., et al., *Self-Assembled Monolayers of Peptide Nucleic Acids on Gold Surfaces: A Spectroscopic Study.* Langmuir, 2005. 21(21): p. 9510-9517.

158. Chandra, A.K., M.T. Nguyen, and T. Zeegers-Huyskens, *Theoretical Study of the Interaction between Thymine and Water. Protonation and Deprotonation Enthalpies and Comparison with Uracil.* The Journal of Physical Chemistry A, 1998. 102(29): p. 6010-6016.

159. Salomon, A., et al., *Comparison of electronic transport measurements on organic molecules.* Advanced Materials, 2003. 15(22): p. 1881-1890.

160. Conwell, E.M., et al., *Duplex polarons in DNA.* Journal of the American Chemical Society, 2007. 129(29): p. 9175-9181.

161. Conwell, E.M. and S.M. Bloch, *Base sequence effects on transport in DNA.* Journal of Physical Chemistry B, 2006. 110(11): p. 5801-5806.

162. Kurnikov, I.V., et al., *Hole size and energetics in double helical DNA: Competition between quantum delocalization and solvation localization.* Journal of Physical Chemistry B, 2002. 106(1): p. 7-10.

163. Conwell, E.M. and S.V. Rakhmanova, *Polarons in DNA.* Proceedings of the National Academy of Sciences of the United States of America, 2000. 97(9): p. 4556-4560.

164. Magulick, J., M.M. Beerbom, and R. Schlaf, *Polarization Lowering of Charge Injection Barriers at a Ribonucleic Acid/Au Interface.* Journal of Applied Physics, 2008. 104: p. 123701.

165. Amy, F., C. Chan, and A. Kahn, *Polarization at the gold/pentacene interface.* Organic Electronics, 2005. 6(2): p. 85-91.

166. Horn, K., et al., *Observation of Final-State Screening in Inverse Photoemission from Adsorbed Xenon Layers.* Physical Review Letters, 1986. 57(8): p. 1064-1067.

167. Jacobi, K., *Photoemission from Ar, Kr, and Xe on Pb(111).* Physical Review, 1988. B38(9): p. 5869-5877.

168. Schlaf, R., et al., *Absence of final state screening shifts in photoemission spectroscopy frontier orbital alignment measurements at organic semiconductor interfaces.* Surface Science, 1999. 420(1): p. L122-L129.

169. Heimel, G., et al., *The Interface Energetics of Self-Assembled Monolayers on Metals.* Accounts of Chemical Research, 2008. 41(6): p. 721-729.

170. Wierzbinski, E., et al., *Charge Transfer through Modified Peptide Nucleic Acids.* Langmuir, 2012. 28(4): p. 1971-1981.

171. Wierzbinski, E., et al., *Effect of Backbone Flexibility on Charge Transfer Rates in Peptide Nucleic Acid Duplexes.* Journal of the American Chemical Society, 2012.

172. Mossine, A.V., et al., *Ferrocene as a Hydrophobic Templating Agent with Pyrogallol[4]arenes.* Israel Journal of Chemistry, 2011. 51(7): p. 840-842.

173. Guo, L.-H., J.S. Facci, and G. McLendon, *Distance dependence of electron transfer rates in bilayers of a ferrocene Langmuir-Blodgett monolayer and a self-assembled monolayer on gold.* The Journal of Physical Chemistry, 1995. 99(21): p. 8458-8461.

174. Watcharinyanon, S., E. Moons, and L.S.O. Johansson, *Mixed Self-Assembled Monolayers of Ferrocene-Terminated and Unsubstituted Alkanethiols on Gold: Surface Structure and Work Function.* The Journal of Physical Chemistry C, 2009. 113(5): p. 1972-1979.

175. Woodbridge, C.M., et al., *HREELS and XPS studies of ferrocene on Ag(100).* Journal of Physical Chemistry B, 2000. 104(14): p. 3085-3093.

176. Gregory, J.K., et al., *The Water Dipole Moment in Water Clusters.* Science, 1997. 275(5301): p. 814-817.

177. Ritsko, J.J., P. Nielsen, and J.S. Miller, *Photoemission from ferrocene, decamethylferrocene, and decamethylferrocene-bis(7,7,8,8-tetracyano-p-quinodimethane).* The Journal of Chemical Physics, 1977. 67(2): p. 687-690.

178. Dowben, P.A., et al., *The occupied and unoccupied electronic structure of adsorbed ferrocene.* Chemical Physics Letters, 1998. 283(1-2): p. 44-50.

179. Welipitiya, D., et al., *The adsorption and desorption of ferrocene on Ag(100).* Surface Science, 1996. 367(1): p. 20-32.

180. Di Felice, R., A. Selloni, and E. Molinari, *DFT Study of Cysteine Adsorption on Au(111).* The Journal of Physical Chemistry B, 2002. 107(5): p. 1151-1156.

181. Furukawa, M., et al., *Geometrical characterization of pyrimidine base molecules adsorbed on Cu(110) surfaces: XPS and NEXAFS studies.* Surface Science, 2003. 532–535(0): p. 261-266.

182. Piana, S. and A. Bilic, *The nature of the adsorption of nucleobases on the gold [111] surface.* Journal of Physical Chemistry B, 2006. 110(46): p. 23467-23471.

183. de Jong, M.P., et al., *Orbital-specific dynamic charge transfer from Fe(II)-tetraphenylporphyrin molecules to molybdenum disulfide substrates.* Physical Review B, 2005. 72(3).

184. Watcharinyanon, S., et al., *Molecular orientation of thiol-derivatized tetraphenylporphyrin on gold studied by XPS and NEXAFS.* Surface Science, 2009. 603(7): p. 1026-1033.

185. Niwa, Y., Kobayash.H, and T. Tsuchiya, *X-Ray Photoelectron-Spectroscopy of Tetraphenylporphin and Phthalocyanine.* Journal of Chemical Physics, 1974. 60(3): p. 799-807.

186. Karweik, D.H. and N. Winograd, *Nitrogen Charge-Distributions in Free-Base Porphyrins, Metalloporphyrins, and Their Reduced Analogs Observed by X-Ray Photoelectron-Spectroscopy.* Inorganic Chemistry, 1976. 15(10): p. 2336-2342.

187. Gottfried, J.M., et al., *Direct synthesis of a metalloporphyrin complex on a surface.* Journal of the American Chemical Society, 2006. 128(17): p. 5644-5645.

188. Kretschmann, A., et al., *Tetraphenylporphyrin picks up zinc atoms from a silver surface.* Chemical Communications, 2007(6): p. 568-570.

189. Ghosh, A., et al., *Electronic Distinction between Porphyrins and Tetraazaporphyrins - Insights from X-Ray Photoelectron-Spectra of Free-Base Porphyrin, Porphyrazine, and Phthalocyanine Ligands.* Inorganic Chemistry, 1994. 33(26): p. 6057-6060.

190. Zeller, M.V. and R.G. Hayes, *X-Ray Photoelectron Spectroscopic Studies on Electronic-Structures of Porphyrin and Phthalocyanine Compounds.* Journal of the American Chemical Society, 1973. 95(12): p. 3855-3860.

191. Castner, D.G., K. Hinds, and D.W. Grainger, *X-ray photoelectron spectroscopy sulfur 2p study of organic thiol and disulfide binding interactions with gold surfaces.* Langmuir, 1996. 12(21): p. 5083-5086.

192. Bain, C.D., H.A. Biebuyck, and G.M. Whitesides, *Comparison of self-assembled monolayers on gold: coadsorption of thiols and disulfides.* Langmuir, 1989. 5(3): p. 723-727.

193. Weisshaar, D.E., M.M. Walczak, and M.D. Porter, *Electrochemically Induced Transformations of Monolayers Formed by Self-Assembly of Mercaptoethanol at Gold.* Langmuir, 1993. 9(1): p. 323-329.

194. Wei, L.Y., et al., *Adsorption characteristics of tripodal thiol-functionalized porphyrins on gold.* Journal of Physical Chemistry B, 2005. 109(50): p. 23963-23971.

195. Ashkenasy, G., et al., *Functional monolayers with coordinatively embedded metalloporphyrins.* Angewandte Chemie-International Edition, 1999. 38(9): p. 1257-1261.

196. Alexander, A.E., *381. Monolayers of porphyrins and related compounds.* Journal of the Chemical Society (Resumed), 1937: p. 1813-1816.

197. Hunter, C.A. and J.K.M. Sanders, *The nature of .pi.-.pi. interactions.* Journal of the American Chemical Society, 1990. 112(14): p. 5525-5534.

198. Sanders, G.M., et al., *Studies on the conformation of 5,15-diarylporphyrins with (arylsulfonyl)oxy substituents.* The Journal of Organic Chemistry, 1988. 53(22): p. 5272-5281.

199. Bai, Y., et al., *Interfacial coordination interactions studied on cobalt octaethylporphyrin and cobalt tetraphenylporphyrin monolayers on Au(111).* Physical Chemistry Chemical Physics, 2010. 12(17): p. 4336-4344.

200. Yoshimura, D., et al., *The electronic structure of porphyrin/metal interfaces studied by UV photoemission spectroscopy.* Synthetic Metals, 1997. 86(1-3): p. 2399-2400.

201. Ishii, H., et al., *Electronic structures of porphyrins and their interfaces with metals studied by UV photoemission.* Molecular Crystals and Liquid Crystals Science and Technology Section a-Molecular Crystals and Liquid Crystals, 1997. 296: p. 427-444.

202. Witte, G., et al., *Vacuum level alignment at organic/metal junctions: "Cushion" effect and the interface dipole.* Applied Physics Letters, 2005. 87(26).

203. Liao, M.S. and S. Scheiner, *Electronic structure and bonding in metal porphyrins, metal=Fe, Co, Ni, Cu, Zn.* Journal of Chemical Physics, 2002. 117(1): p. 205-219.

204. Rojas, G., et al., *Self-Assembly and Properties of Nonmetalated Tetraphenyl-Porphyrin on Metal Substrates.* Journal of Physical Chemistry C, 2010. 114(20): p. 9408-9415.

205. He, C., et al., *Turn on fluorescence sensing of vapor phase electron donating amines via tetraphenylporphyrin or metallophenylporphrin doped polyfluorene.* Chemical Communications, 2010. 46(40): p. 7536-7538.

206. Schlettwein, D. and N.R. Armstrong, *Correlation of Frontier Orbital Positions and Conduction Type of Molecular Semiconductors as Derived from Ups in Combination with Electrical and Photoelectrochemical Experiments.* Journal of Physical Chemistry, 1994. 98(45): p. 11771-11779.

207. Kaushik, V.K., *XPS core level spectra and Auger parameters for some silver compounds.* Journal of Electron Spectroscopy and Related Phenomena, 1991. 56(3): p. 273-277.

208. Polzonetti, G., P. Alnot, and C.R. Brundle, *The adsorption and reactions of NO2 on the Ag(111) surface: I. XPS/UPS and annealing studies between 90 and 300 K.* Surface Science, 1990. 238(1–3): p. 226-236.

209. Zemlyanov, D.Y., A. Nagy, and R. Schlögl, *The reaction of silver with NO/O2.* Applied Surface Science, 1998. 133(3): p. 171-183.

210. Flechtner, K., et al., *Surface-confined two-step synthesis of the complex (ammine)(meso-tetraphenylporphyrinato)-zinc(II) on Ag(111).* Journal of Physical Chemistry C, 2007. 111(16): p. 5821-5824.

211. Shubina, T.E., et al., *Principle and mechanism of direct porphyrin metalation: Joint experimental and theoretical investigation.* Journal of the American Chemical Society, 2007. 129(30): p. 9476-9483.

212. Duisman, J.A. and S.A. Stern, *Vapor pressure and boiling point of pure nitric acid.* Journal of Chemical & Engineering Data, 1969. 14(4): p. 457-459.

213. Gerenser, L.J., *Photoemission Investigation of Silver Poly(Ethylene-Terephthalate) Interfacial Chemistry - the Effect of Oxygen-Plasma Treatment.* Journal of Vacuum Science & Technology a-Vacuum Surfaces and Films, 1990. 8(5): p. 3682-3691.

214. Wagner, C.D. and G.E. Muilenberg, *Handbook of x-ray photoelectron spectroscopy: a reference book of standard data for use in x-ray photoelectron spectroscopy*. 1979: Perkin-Elmer Corp., Physical Electronics Division.

215. Jablonski, A., B. Lesiak, and G. Gergely, *Derivation of the Electron Inelastic Mean Free-Path from the Elastic Peak Intensity.* Physica Scripta, 1989. 39(3): p. 363-366.

216. Hebenstreit, W., et al., *Bulk Terminated NaCl(111) on Aluminum: A Polar Surface of an Ionic Crystal?* Physical Review Letters, 2000. 85(25): p. 5376-5379.

217. Schnippering, M., et al., *Electronic properties of Ag nanoparticle arrays. A Kelvin probe and high resolution XPS study.* Physical Chemistry Chemical Physics, 2007. 9(6): p. 725-730.

APPENDICES

Appendix A: Copyright Permission to Use Figure 1

Home | Create Account | Help

Title: Self-Assembled Monolayers of Thiolates on Metals as a Form of Nanotechnology
Author: J. Christopher Love et al.
Publication: Chemical Reviews
Publisher: American Chemical Society
Date: Apr 1, 2005

User ID
Password
Enable Auto Login
LOGIN
Forgot Password/User ID?
If you're a copyright.com user, you can login to RightsLink using your copyright.com credentials. Already **a RightsLink user** or want to learn more?

PERMISSION/LICENSE IS GRANTED FOR YOUR ORDER AT NO CHARGE

This type of permission/license, instead of the standard Terms & Conditions, is sent to you because no fee is being charged for your order. Please note the following:

- Permission is granted for your request in both print and electronic formats, and translations.
- If figures and/or tables were requested, they may be adapted or used in part.
- Please print this page for your records and send a copy of it to your publisher/graduate school.
- Appropriate credit for the requested material should be given as follows: "Reprinted (adapted) with permission from (COMPLETE REFERENCE CITATION). Copyright (YEAR) American Chemical Society." Insert appropriate information in place of the capitalized words.
- One-time permission is granted only for the use specified in your request. No additional uses are granted (such as derivative works or other editions). For any other uses, please submit a new request.

BACK | CLOSE WINDOW

Appendix B: Copyright Permission to Use Table 1 and Figures 27 and 28

Home | Create Account | Help

Title: Electronic Structure of Self-Assembled Peptide Nucleic Acid Thin Films
Author: Matthäus A. Wolak et al.
Publication: The Journal of Physical Chemistry C
Publisher: American Chemical Society
Date: Sep 1, 2011

User ID
Password
Enable Auto Login
LOGIN
Forgot Password/User ID?
If you're a copyright.com user, you can login to RightsLink using your copyright.com credentials. Already **a RightsLink user** or want to learn more?

PERMISSION/LICENSE IS GRANTED FOR YOUR ORDER AT NO CHARGE

This type of permission/license, instead of the standard Terms & Conditions, is sent to you because no fee is being charged for your order. Please note the following:

- Permission is granted for your request in both print and electronic formats, and translations.
- If figures and/or tables were requested, they may be adapted or used in part.
- Please print this page for your records and send a copy of it to your publisher/graduate school.
- Appropriate credit for the requested material should be given as follows: "Reprinted (adapted) with permission from (COMPLETE REFERENCE CITATION). Copyright (YEAR) American Chemical Society." Insert appropriate information in place of the capitalized words.
- One-time permission is granted only for the use specified in your request. No additional uses are granted (such as derivative works or other editions). For any other uses, please submit a new request.

BACK | CLOSE WINDOW